MASS TRANSPORT AND WETTING RESISTANCE IN MEMBRANES FOR ADVANCED WATER TREATMENT

by

SANGSUK LEE

B.S., Korea University, 2014

M.E., Korea University, 2016

M.S., Carnegie Mellon University, 2018

A thesis submitted to the

Faculty of the Graduate School of the

University of Colorado in partial fulfillment

of the requirement for the degree of

Doctor of Philosophy

Department of Civil, Environmental, and Architectural Engineering

May 2023

Committee Members:

Dr. Anthony P. Straub, chair

Dr. Julie Korak

Dr. Sheldon Masters

Dr. Yifu Ding

Dr. Michael Shirts

Abstract

Sangsuk Lee (Ph.D., Environmental Engineering)

MASS TRANSPORT AND WETTING RESISTANCE IN MEMBRANES FOR ADVANCED
WATER TREATMENT

Thesis directed by Assistant Professor Anthony P. Straub

1 in 4 people on Earth face a lack of clean and safe water sources for drinking, irrigation, sanitation, and economic development. The urgent need for water motivates the use of unconventional water resources, such as seawater and wastewater. Advanced water treatment technologies that allow us to access these unconventional resources are drawing increasing attention. Membrane processes including reverse osmosis (RO) and nanofiltration (NF) have been rapidly growing as advanced water treatment technologies for desalination and water reuse due to high productivity, cost-effectiveness, and scalability. The objective of this dissertation research is to further understand mass transport of water and solutes across membranes and increase the effectiveness of innovative distillation-based membrane technologies.

Numerous potentially harmful compounds exist in feed streams entering advanced water treatment facilities, and thus, understanding membrane rejection in reverse osmosis and nanofiltration for hundreds of compounds is critical for securing high quality product water. A large rejection dataset was compiled, and machine learning techniques enhanced by molecular fingerprints were used to predict membrane rejection of organic compounds. These techniques allowed us to interpret the relationship between the molecular structure of the solute and its rejection in membrane processes. The machine learning models showed high prediction accuracy

(Spearman and Pearson coefficients of 0.86-0.99) both with training and test sets. Then, the trained models were analyzed using Shapley values to study the effects of sub-structures of organic compounds on membrane rejection.

The second study in this dissertation focused on addressing the low water flux of the osmotic distillation (OD) process. We found that the high membrane thickness (typically 30-100 μm) of current membranes was the main cause of low water fluxes. An optimal membrane thickness of 0.073 μm was derived with element-scale simulations, and it was able to achieve water fluxes exceeding those of current commercial forward osmosis (FO) membranes. In addition, comparison of module-scale performance with OD and FO membranes found that optimized OD membranes can outcompete high-performance FO membranes in maximum achievable water flux (25.3 vs. 18.6 kg m^{-2}h^{-1} for OD and FO membranes, respectively) and water recovery (0.28 vs. 0.18).

The third study in this dissertation focused on the transport of volatile compounds in membrane distillation (MD). Rejection of volatile compounds in MD is highly varied and poorly understood. This study analyzed a variety of volatile and semi-volatile organic compounds to yield a comprehensive understanding of transport in MD. The effects of different molecular properties on transport were studied first, and we found the Henry's constant and diffusion coefficient were important in determining solute flux. Then, the transport resistances across MD membranes were quantified and two distinct transport regimes (membrane resistance regime and boundary layer resistance regime) were defined.

Hydrophobic membranes are susceptible to membrane pore wetting, which results in failure of the system. To overcome this issue in pressure-driven distillation treating low surface tension liquids, the final study in the dissertation focused on fabricating omniphobic, wetting

resistant membranes. Nanoporous membranes were modified with re-entrant structures and low surface energy. The results showed the liquid entry pressure values of the modified membranes were much higher than those of conventional membranes with cylindrical pores, allowing for the desalination at 16 bar with a 15% water-ethanol mixture. This low surface tension feed solution wetted the membrane with cylindrical pores.

Acknowledgements

I am thankful to God and lots of people who have supported me and contributed to my personal growth and professional development throughout my Ph.D. journey. It is overwhelming to consider the support that I have received during my time pursuing Ph.D.

First, I would like to express my deep gratitude to my academic advisor, Prof. Anthony Straub, for his consistent support like a friend and the many opportunities he provided as the leader of our research group. He has made a friendly and supportive environment so that I was able to spend my days at graduate school more enjoyable.

I am also grateful to my committee members, Prof. Julie Korak, Prof. Sheldon Masters, Prof. Yifu Ding, and Prof. Michael Shirts, for their advice and support throughout my Ph.D. research. They were a helpful source of knowledge and inspiration outside of my research group. Especially, Prof. Michael Shirts as a co-author of my journal paper helped me to strengthen the statistical aspect and the simulation details of the paper.

Outside of the CU Boulder community, I want to thank my previous advisors, Prof. Seungkwan Hong and Prof. Kelvin Gregory at Korea University and Carnegie Mellon University, respectively. They were very supportive of me pursuing a doctoral degree and offered helpful discussions when I needed.

I would like to thank my family and friends who made this journey even more rewarding and satisfying. I am especially thankful for the support of my parents, Hongjai Lee and Hyunsook Chae in Seoul, Korea. I am also grateful to my friends in the Straub group and in Boulder for their help and their stimulation in broadening my horizons. Special thanks to Jihyeok Park who has constantly cared for my soul by sending pastors' sermons and Bible verses.

This journey would not have been possible without the grace of God. His presence is the anchor of my soul so that I can be unshaken under any circumstances. He is my light in the darkness that leads me toward the right path.

CONTENTS

LIST OF TABLES

LIST OF FIGURES

CHAPTER 1

Introduction

1.1 Background and research needs

The shortage of clean and safe water has become an urgent global issue because one-third of the world population is affected by water scarcity today.[1] The 2021 Annual Report of the World Economic Forum examined the global water crisis and found causes of water scarcity include an exponential growth in the world population, increased industrial activities, improved living standards, and expanding agricultural irrigation. The United Nations Water Development Report estimated global water consumption will continue increasing at a rate of 1% every year.[2] Although the absolute amount of available water sources is enough to meet the increasing demands, temporal and spatial variations of water supply and demand are large, which leads to severe water scarcity at certain locations during specific times of the year. For example, 400 million people from India and China experience water scarcity at least one month each year according to the Human Development Report.[3] Thus, developing advanced water treatment technology that can expand accessible water supplies from seawater, wastewater, and other non-traditional sources is urgent to address the imbalanced temporal and spatial distribution of water resources.

Membrane processes including reverse osmosis (RO) and nanofiltration (NF) have drawn enormous interest as technologies to address water scarcity, and capital investments on the membrane systems have grown by 15% per year.[4] The key advantages of membrane processes include high energy efficiency, compact and scalable design, ease of operation, and reliable removal of target compounds. As a result, RO and NF technologies are experiencing growth in a

wide range of applications outside of traditional water treatment, such as drug purification, industrial wastewater treatment, protein concentration, and food processing.

Despite the growth in implementation of membrane processes, RO and NF systems are well-known to suffer from poor rejection of certain harmful compounds and a trade-off between water permeability and water-salt selectivity.[5] Moreover, RO and NF membranes demonstrated low rejections of small compounds with neutral charge such as N-nitrosodimethylamine (NDMA), N-methylethanolamine (NMEA), urea, and boron. On top of that, there are numerous emerging organic compounds entering water and wastewater treatment facilities, and many of the compounds' rejections are not identified yet.[6] Lastly, current polymer membranes for RO and NF are inherently constrained due to a permeability-selectivity tradeoff where increasing water permeability unavoidably accompanies unwanted selectivity losses.[7]

Distillation-based membrane processes that use hydrophobic porous membranes have recently gained attention because of their ability to overcome some the key limitations of RO and NF. Distillation processes utilize hydrophobic membranes that trap air within their pores. During operation, water evaporates on the feed side, diffuses through the thin air layer in the gas phase, and condenses on the permeate side due to driving forces induced by temperature, pressure, or concentration differences. Unlike RO and NF, distillation processes ideally offer near-complete rejection for non-volatile compounds, which include small and neutral compounds that are problematic in RO and NF. The phase-change selectivity mechanism potentially allows distillation processes to circumvent the permeability-selectivity tradeoff that constrains conventional dense polymeric membranes. Thus, it is hypothetically viable to accomplish high permeability and complete rejection at the same time.[8] Because of the potential strengths of distillation processes,

they are experiencing growing interest in the treatment of high salinity brines from shale gas and oil operations, food concentration, and industrial wastewater.[9]

Although distillation-based membrane processes offer the potential to overcome major challenges facing conventional membranes, they also suffer from several shortcomings that have drawn research attention, such as low water productivity, poor rejection of volatile compounds, and membrane wetting. Low water productivity is observed in distillation-based membrane processes, meaning that their flux rates can be substantially lower than those of current membrane systems. For example, osmotic distillation (OD) is a process analogous to forward osmosis using concentration difference between the feed and draw sides to induce partial vapor pressure difference. Since OD does not require heat or applied pressure, it has the advantage to separate compounds sensitive to heat and pressure. However, the water flux in OD processes is only 1-2 LMH, which is much lower than in conventional membrane systems.[10,11] Thus, there is a need to investigate optimal membrane design and heat transfer effects for OD membranes to improve water productivity.

Poor rejection of volatile compounds is another key issue facing distillation-based membrane processes. Membrane distillation (MD), which uses a temperature difference to drive water flow, has become an increasingly considered approach treat high salinity water, and there is burgeoning interest in applying the process for a variety of feed streams that have volatile organic compounds (VOCs). However, only few studies have examined the mass transport of VOCs across distillation membranes, and the number of volatile compounds used in the experiments was also limited.[12,13] Thus, there is a need to study more general trends between compound volatility and membrane rejection with a wider set of VOCs.

Distillation-based processes are also limited by membrane pore wetting. Membrane wetting occurs when the air layer in the membrane becomes displaced by liquid water, leading to a loss in selectivity and process failure. There are two principal causes of membrane wetting. First, liquid penetrates membrane pore when external hydraulic pressure exceeds the liquid entry pressure (LEP) of membrane, which can be calculated by the Young-Laplace equation. Second, wetting can be caused by the treatment of low surface tension liquid. When the surface tension of liquid is low enough, the solid-liquid interface becomes more favorable than solid-air interface. The occurrence of this wetting depends on material surface energy, liquid and solute properties, and the structure of pore. Pretreatment getting rid of unwanted wetting agents in prior and coating highly hydrophobic chemicals on membrane have been typical strategies to prevent from wetting. However, these methods can be costly. There is therefore a need for membrane designs that inherently resist wetting.[14,15]

1.2 Scope of the dissertation

The principal scope of this dissertation research is to investigate mass transport and wetting resistance of membranes for advanced water treatment. The work first focuses on understanding the rejection of compounds in RO and NF to improve our capacity to predict the rejection of emerging contaminants. The work then shifts focus to understand and improve emerging distillation-based membranes. This includes addressing low water productivity, poorly understood contaminant rejection, and wetting in distillation-based membrane processes. For each chapter, experimental or theoretical approaches are used to examine critical factors governing the performances of the processes. The results of this dissertation work will expand the application of membrane technologies for sustainable desalination and water reuse.

The following specific objectives are targeted in this dissertation:

i. Analyze the rejection of emerging organic compounds in RO and NF with molecular fingerprints to improve prediction capabilities and molecular-level understanding of rejection mechanisms.

ii. Simulate osmotic distillation with different membrane properties and operating conditions to identify the optimal membrane and system design.

iii. Identify critical properties of volatile organic compounds to understand volatile solute transport across hydrophobic membranes used in membrane distillation.

iv. Develop wetting-resistant omniphobic membranes with re-entrant pore structures for treating low surface tension liquids in pressure-driven distillation.

1.3 Key contributions

This dissertation research advances the use of data and data-driven models to understand and improve membrane processes. Computational approaches that have experienced growth in other scientific areas, such as the use of molecular fingerprints, are applied to membrane science. Furthermore, innovations in materials science and the design of nanomaterials are leveraged to improve the robustness of emerging membrane processes. The major contributions of this work include the following:

> **Chapter 2 demonstrated the use of machine learning and molecular fingerprints for predicting and understanding contaminant rejection in RO and NF membranes at the molecular level.** The novel data structure of molecular fingerprints was introduced to build membrane rejection prediction models with a machine learning algorithm. The study showed the validity of models trained with molecular fingerprints instead of typical molecular properties such as molecular weight, octanol-water partition coefficient, and dipole moment. Subsequently, different molecular fingerprints including path-based, circular, and structural-key fingerprints were compared to explain how their prediction performances, calculation efficiency, and interpretability vary. The results displayed that

the simple and straightforward structural-key fingerprint may be the best choice in this scenario. Lastly, rejection mechanisms were explained using fingerprints to connect rejections to molecular structures.

Chapter 3 identified the potential membrane design for osmotic distillation to outperform forward osmosis in desalination. Element- and module-scale computational modeling were used to examine OD membrane properties and to improve water productivity. Membrane thickness was the most crucial factor in enabling high performance, and a thickness of 0.073 μm is needed to achieve water fluxes exceeding those of current commercial FO membranes. Module-scale comparison of OD with FO showed that optimized OD membranes can outcompete high-performance FO membranes in maximum achievable water flux (25.3 vs. 18.6 kg m^{-2}h^{-1} for OD and FO membranes, respectively) and water recovery (0.28 vs. 0.18).

Chapter 4 demonstrated crucial compound properties to understand volatile solute transport in membrane distillation. The transport of a wide range of semi-volatile and volatile compounds in membrane distillation (55 compounds total) was examined, which allows us to gain broad insights into the compound properties, system designs, and operating conditions that impact transport rates in MD. The study showed that the Henry's constant and diffusion coefficient are the most important molecular properties in determining solute flux. Distinct transport regimes were also found: the membrane resistance regime is dominated by resistances associated with diffusion through the membrane, and the boundary layer resistance regime is dominated by resistance to transport through boundary layers on either side of the membrane. Lastly. simulations of

large-scale MD modules revealed the impact of membrane area, operating temperature, and crossflow velocity on the removal of contaminants.

Chapter 5 developed a novel omniphobic membrane with re-entrant structures, which can be used for treating low surface tension liquids in pressure-driven distillation. Membranes with nano-sized pores were modified with nanoparticles to build re-entrant structures and hydrophobic modification was performed. Improved wetting resistance of the modified membrane was confirmed as comparing to the control membranes without nanoparticles. The control membrane was immediately wicked with a 40% ethanol and water mixture, whereas the modified membrane showed the liquid entry pressure of 5 bar for the same mixture. During flux and rejection tests, the modified membrane was operated under 100 psi for 24 and 48 hours, and the membranes were not compromised with high NaCl rejection of 97%.

1.4 Dissertation overview

Table 1.1 Dissertation overview with hypotheses

Topic	Chapter	Approaches	Specific objectives
Prediction model trained upon molecular fingerprints of emerging organic compounds	2	Data analysis	1. Confirm model validation trained upon fingerprints 2. Compare the effects of different fingerprint algorithms 3. Build relationship between membrane rejection and molecule structure
Optimized membrane design for improved water productivity in osmotic distillation	3	Numerical analysis	1. Decide critical membrane properties to increase flux 2. Optimize OD membrane design to outperform conventional membranes in water productivity

Investigation of volatile compound properties to understand their transport in membrane distillation	4	Numerical analysis	1. Investigate a transport of a wide range of volatile compounds in membrane distillation 2. Examine the influence of different molecular properties on transport 3. Study the transport resistances across hydrophobic membranes
Improved wetting resistance induced by re-entrant structures for treating low surface tension liquids in pressure-driven distillation	5	Bench-scale experiments	1. Develop an omniphobic membrane with re-entrant structures 2. Confirm improved liquid entry pressure and stability in flux and rejection tests

CHAPTER 2

Predicting organic solute rejection in reverse osmosis and nanofiltration with machine learning and molecular fingerprints

2.1 Introduction

3.6 billion people experience water scarcity at least one month per year, and water shortages are become more severe because of climate change and increasing water demands.[16] Processes that utilize unconventional water resources such as desalination, brine treatment, and water reuse have the potential to sustainably alleviate water stress by augmenting clean water supplies beyond those available from existing water resources. Reverse osmosis (RO) and nanofiltration (NF) are widely considered in advanced water treatment trains because of their ability to remove a broad spectrum of compounds, including salts and harmful organic contaminants, more reliably than other processes.[17] In addition to water treatment, RO and NF are increasingly considered in a broad suite of separations applications including drug purification, protein concentration, and food processing.[18–21]

Emerging water treatment applications, such as municipal and industrial wastewater reuse, include myriad organic compounds in the feed streams. Some of these compounds, such as 1,4-dioxane and N-nitrosodimethylamine (NDMA), are of particular concern because they are known to be harmful to human health and are well-documented as being poorly removed by membrane processes.[22] However, many other potentially harmful compounds exist in feedwaters with poorly understood rejection in NF and RO.[23] It is thus of critical importance to develop an ability to determine the removal of a broad range of compounds in membrane systems. To date, much of our understanding of membrane rejection has relied on experimental measurements of rejection

for individual compounds in studies that generally examined between 5 and 30 compounds.[24] These individual experimental measurements provide valuable insights, but alternative methods are necessary to approximate rejection of the multitude of compounds in feedwaters and develop a greater understanding of rejection mechanisms.[25,26]

Machine Learning (ML) models are powerful tools to address complex real-world problems in many science and engineering fields such as material development, chemical processing, biomedical study, and environmental science.[27] ML models are constructed from data, enabling complicated non-linear relationships to be captured by such predictive algorithms. In the field of membrane separations, ML models have been used to predict rejection of emerging compounds based on collected rejection data.[27–33] These ML methods have been valuable for the selection of a suitable membrane for a given application and used in the design of membrane processes.[34,35] Moreover, the ML models have been tools to predict rejection using membrane and compound properties.[36–40]

In studying membrane rejection, a major downside of ML algorithms is the challenge of gaining a mechanistic understanding of the mechanisms by which compound and membrane properties influence rejection. Previous ML models used to predict rejection of different compounds in membrane processes have used input parameters based on compound descriptions such as molecular weight, dipole moment, and octanol-water partition coefficient.[27,32,41] While these descriptors can effectively quantify the physicochemical properties of a compound, they lack the ability to intuitively express structural information and atom connectivity.[28,42] Recent rejection studies indicated that the interactions between functional groups and aromatic rings on compounds and polyamide membranes are strongly related to rejection,[43–45] and considering the molecular structure is therefore critical to understand how functional groups and their positions

10

within the molecule influence membrane rejection. Moreover, phenomena such as proton dissociation, which enhances rejection through strong electrostatic repulsion, are closely related to molecular structures.[46,47] To gain molecular-level mechanistic insights into membrane rejection, models that include details on molecular structure are therefore needed.[27,48] Furthermore, some molecular descriptors such as acid dissociation constants are not readily available for certain compounds, precluding the analysis of a broad range of contaminants.

Molecular fingerprints (MFs) are a promising method to encode organic compound structures. MFs transform chemical structural features into binary vectors (0's and 1's) and the binary vectors account for the absence or presence of molecular sub-structures.[49,50] Recently, multiple studies successfully built data-driven models using MFs as input data to predict molecular properties including the refractive index, viscosity, acid dissociation constant, and reaction rate of the organic compounds with hydroxyl radical.[50–53] In addition, Shapley Additive Explanations (SHAP) have been used as an evaluation tool to explain the relationships between input and output data for ML models.[54] Typically, ML models do not provide clear relations between input and output, and thus, explainable machine learning techniques such as SHAP can help to unveil the decision-making process of ML models. In studying RO and NF membrane rejection, the combination of MF data and SHAP has potential to elucidate the interplay of different molecular fragments and membranes to reveal complex RO/NF membrane rejection mechanisms.[36–40] However, no studies to date have used the MFs of organic solutes to predict rejection in RO and NF water treatment processes.

In this study, we develop ML models trained upon MFs to predict contaminant rejection and examine the potential of MFs and ML techniques to discover underlying rejection mechanisms. The models are trained with three different fingerprint categories (path-based, circular, and

structural-key) and 1906 rejection samples (228 unique organic compounds). We first compile input datasets including membrane properties, operating conditions, and the different MFs of a compound. The prediction performances of the trained models are quantified through evaluation metrics such as Pearson and Spearman coefficients. We change the parameters for fingerprints (e.g. maximum path length, maximum radius, structural-key number) to estimate optimal fingerprints in terms of prediction power, calculation expense, and interpretability. Molecular fragments created by each fingerprint, SHAP value, and unsupervised clustering analysis are used to gain an understanding of molecular-scale compound-membrane interactions. Our analysis provides a valuable tool for rejection prediction and important insights into future improvements of RO and NF rejections for emerging organic contaminants.

2.2 Methods

2.2.1 Overview of dataset and data processing

Membrane properties, corresponding compound SMILES, and rejection values were obtained from the previous literature.[27,31] The dataset included 1906 data points, 228 organic compounds, and 39 types of RO and NF membranes. The retrieved SMILES for the organic compounds were converted into three classes of MFs, path-based, circular, and structural-key. RDKit and Morgan fingerprints were chosen as the path-based and circular fingerprints, respectively. MACCS and PubChem fingerprints were chosen as structural key fingerprint. Insufficient data were available for membrane surface charge in the original dataset, so solution pH was used as an indirect feature of membrane surface charge because solution pH governs the extent of protonation on the membrane surface.[55]

Table 2.1 summarizes the information available in the input datasets excluding the MFs. The datasets used for model training contained three membrane properties (membrane weight cut-off,

membrane contact angle, and solution pH), three operating conditions (pressure, measurement time, and initial concentration), and MFs that represent the molecular properties. The distribution of output (rejection, R) demonstrated a severely left-skewed shape indicating that the data was imbalanced since rejection values tended to be high, with most rejection values greater than 90%. In this study, the original distribution, -log(1-R) transformation, and -sqrt(1-R) transformation were examined and the -sqrt(1-R) transformation was finally applied on the output because the sqrt(1-R) transformation shifted the left-skewed distribution closer to normal distribution. All input and output values were scaled from 0 to 1 to render the range of values equal for training, and then the outputs were transformed back to the original scale when evaluating model performance. The entire dataset is available in the Supporting Information, and the detailed descriptions about MFs can be found in the next section.

Table 2.1 Overall distribution of the input data

	pH	MB MWCO (Da)	MB contact angle	Pressure (kPa)	Measurement time (min)	Initial concentration of compound (mg/L)	Rejection (%)
25th Percentile	7.0	100	41.4	500	10	0.053	72.06
50th Percentile	7.0	152	53.8	690	10	0.5	90.82
75th Percentile	7.0	300	63.2	1000	300	10.0	96.90
Min value	2.2	65	14.4	240	10	0.00072	0
Max value	11	460	79.4	3500	5760	2000	100

2.2.2 Molecular fingerprints generation

Molecular fingerprints (MFs) encode the structural information of chemical compounds into binary vectors. Each binary value (0 or 1) indicates whether a certain molecular fragment exists in a compound and the position of the binary vector displays which molecular fragment it is. This molecular representation enables the computationally efficient management and comparison of

13

chemical structures (e.g. Tanimoto and Dice similarity coefficients).[56] Fingerprinting has played a key role in virtual screening, QSAR/QSPR analysis, similarity-based compound search, target molecule ranking, and other chemical compounds discovery processes.[57] Moreover, previous studies proved that fingerprinting is useful for ML models to predict variables depending highly on molecular structures.[58–62]

There are five main categories of 2D fingerprints, namely substructure key-based fingerprints, topological or path-based fingerprints, circular fingerprints, pharmacophore, and neural fingerprints. Three categories of fingerprints were applied in this study to convert SMILES into binary vectors: path-based (RDKit), circular (Morgan), and structural-key (PubChem and Molecular Access System (MACCS)). RDKit fingerprint is a path-based fingerprint and maximum path lengths of 1 and 3 and bit lengths of 1024 and 32768 were chosen. Path-based fingerprints encode all possible connectivity for the fragments of a compound following a linear path along the molecular graph from a central atom up to a given maximum length. Under a path-based approach, any compound can produce a meaningful fingerprint; however, bit collision can be an issue because a bit can be set by multiple different fragments.[63] Although it increases computational complexity, the expanded bit lengths of 32768 were used for the maximum path length of 3 to avoid bit collision; a detailed explanation of bit collision counts can be found in the Supporting Information. The circular Morgan fingerprint had a maximum radius of 1 and 3 and bit lengths of 4096 and 16384 were chosen. The radius does not have units and depends on the radial distance from a center-atom. The circular fingerprint utilizes a similar approach to the path-based fingerprint but constructs fragments within a radius of the starting atom instead of linear paths. PubChem and MACCS were used as structural key fingerprints. PubChem fingerprints are based on 881 structural keys defined by PubChem database system. MACCS uses 166 keys developed

by the Molecular Design Limited (MDL) Information Systems, and during data generation, one dummy bit was padded to the head of the MACCS keys, which resulted in 167 keys in total. Structural keys-based fingerprints define the bits depending on the presence and absence in the compound of certain fragments from a given list of structural keys. Therefore, these fingerprints are meaningful when with molecules' fragments mostly covered by the pre-defined keys.[63]

2.2.3 Model development

XGBoost (Extreme Gradient Boosting) algorithm was used to build models for predicting contaminant rejection with multiple fingerprint datasets (Figure 2.1). XGBoost falls under the category of ensemble methods. The algorithm creates a set of additive estimators, wherein the next estimator is fit to the residual errors of the previous estimator, and its training is fast and capable of handling overfitting due to improved regularization.[64] Although the algorithm has very low probability to predict a value outside of the given output range (rejection 0–100%), we defined boundary conditions to ensure predicted values always fall in the range of 0–100%. Incremental learning was used to deal with the 70 samples having the same output value (100% rejection) with different inputs. In each cycle, 50% of training set was randomly selected to train a model and positive normally distributed random noises (1% mean and 0.5% standard deviation of the 100% rejection) were deducted from the 100% rejection values to jitter the points. This process was repeated over 100 cycles and the coefficients of a model were incrementally updated at each cycle. The test set that was not seen during the training was used for evaluation. To verify the models' validity and robustness, datasets were randomly split into a training set and a test set with a ratio of 4 to 1. The datasets were significantly imbalanced with few of points in the low rejection range, so a stratified split was applied with 5 bins to preserve the percentage of samples for each bin in the training and test sets. For estimating the model performance, the mean square error (MSE),

Spearman, and Pearson coefficients were calculated with each training and test set, respectively. Pearson coefficients are commonly used to evaluate prediction models, so scores can be compared to previous studies.[27,65] Spearman coefficients were also used to assess monotonic and non-linear relationship in rejections. Membrane rejection is the outcome of the complex interaction between membrane properties, operating conditions, and compounds, so that Spearman coefficient is useful to catch non-linear trends. All the implementations of the procedures above were executed with the XGBoost and scikit-learn libraries in Python. The datasets and codes used to generate the results were deposited in a GitHub repository (see Supplementary Information).
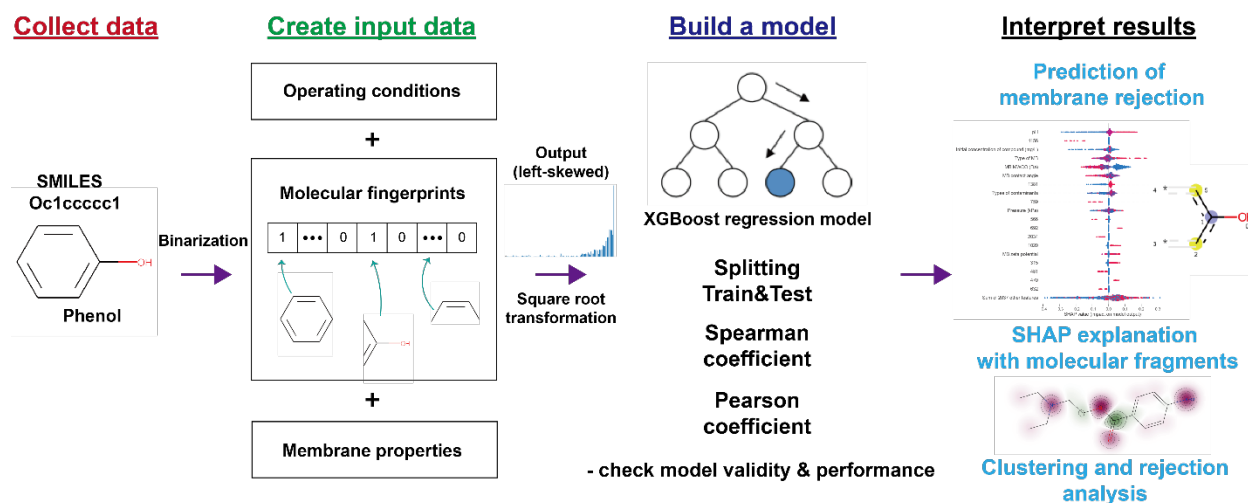
Figure 2.1 Overall workflow of this study demonstrating the input data shapes, model development procedures, and approaches for model interpretation.

2.2.4 Shapley values and clustering analysis for explainable machine learning models

Shapley additive explanations (SHAP) are used for evaluating the influence of each single input feature on rejection. The process is based on the cooperative game theory that analyzes the contribution of each input variable to the outcome by measuring the significance of every single variable.[66] SHAP has the models be trained with all possible combinations of the input variables, and the differences of the predicted outcome including and excluding an input variable of interest

are computed. The SHAP results can clarify which compound fragments (input) most affect rejection (output) and thus help explain the rejection mechanisms. Molecular fragments of compounds are drawn using RDKit library to further investigate the interactions between membrane and compound. The importance score of a feature is obtained by averaging absolute SHAP values of each data point for the feature.

Clustering is a powerful unsupervised machine learning technique that can help to group similar data points. Clustering can help to identify patterns and relationships between different groups of data points. By examining the characteristics of each cluster, we can understand what makes them similar or different. T-distributed Stochastic Neighborhood Embedding (t-SNE) was used as a clustering algorithm. The Scikit Learn library in Python was used to implement t-SNE. The number of clusters was fixed at 4, so four different clusters were defined. The MACCS fingerprint was used to implement the clustering of the 228 organic compounds. Sub-dataset was generated with conditions of MWCO < 225 Da and pH = 7 to eliminate the effects of MWCO and pH, and focus on the effect of the molecular structures. A point on the plot represents an organic compound, and the values of the x and y axes are equivalent to the reduction of 167 structural keys of MACCS. The averaged rejections of the compounds were displayed with colors.

2.3 Results and Discussion

2.3.1 Validation of learning process and prediction performance

The learning processes and prediction performances of the three fingerprint-based models (path-based, circular, and structural key) were evaluated with data divided into train and test sets with stratified split, and the results indicated that models were well-trained. The datasets included the same input features and rejections except for fingerprints. Figure 2.2A–C shows the learning curves with different fingerprints where the maximum path length for the path-based fingerprint

was 3, the maximum radius for the circular fingerprint was 3, and the bit length of the PubChem fingerprint was 881. The default maximum path length and radius are 7 in RDKit, and here we chose 3 because organic compounds in the data are relatively small compared to proteins and macromolecules. The learning curves are broadly used to see how models learn and minimize errors over time. The results demonstrated that error decreased with an increasing number of iterations, eventually reaching a lower limit of error at a high number of iterations. For the circular and PubChem cases, the test errors did not start increasing after hitting the plateau; this indicates the models were not overfitted, which would be shown by test error increasing while training error decreases. For example, the testing error during the learning process with the circular fingerprint was about 0.0013, and the training error was 23% lower at around 0.0010. On the other hand, the test set error of the path-based model increased by 16% from the 90th iteration to the end of 100th iteration, which indicates that the model may start being overfitted at the 90th iteration and should be stopped prior to this cycle.

After training procedures, measured rejections and predicted rejections were compared (Figure 2.2D–F), and MSE, Spearman, and Pearson coefficients of the three models were calculated (Table 2.2). MSE values in the learning curves were obtained using scaled rejections, and the MSE values in Table 2.2 are reported with rejections in the original scale (0-100%). The results showed that all three fingerprint models (path-based, circular, and PubChem) had high Spearman coefficients (greater than 0.98) with the training sets. For the test sets, the performances of the path-based, circular, and PubChem models decreased to 0.91, 0.93, and 0.92, respectively. The Pearson coefficient results were similar to the Spearman results. The Pearson coefficients with the training sets were high (0.96-0.99), and the coefficients with the test sets fell in the range of 0.84-0.88, with the path-based model showing the lowest coefficient.

18

Table 2.3 summarizes results from 11 previous studies using ML to evaluate membrane rejection. Their datasets included information on molecular properties, membrane properties, operating conditions, and RO and NF membrane rejections.[28,30–33,41,67–71] Although the most common ML algorithm for these studies has been neural networks, gradient boosting has recently become popular. The size of the dataset is critical to build a robust ML model, and the ranges of the data size varied widely from 19 to 38430 rejection points. Although some studies did not report performances that can be compared directly to those in this work, the Pearson coefficients with test sets fell in the range between 0.84 and 0.99. The dataset size of our study is 1906, which is equivalent to the largest datasets used to study solute rejection in RO and NF using aqueous feed streams. We used unique input features, molecular fingerprints, to investigate the effects of molecular structures and functional groups on membrane rejection. Our model results indicate the fingerprint-based models have comparable predictive performances to previous work based on molecular descriptors.
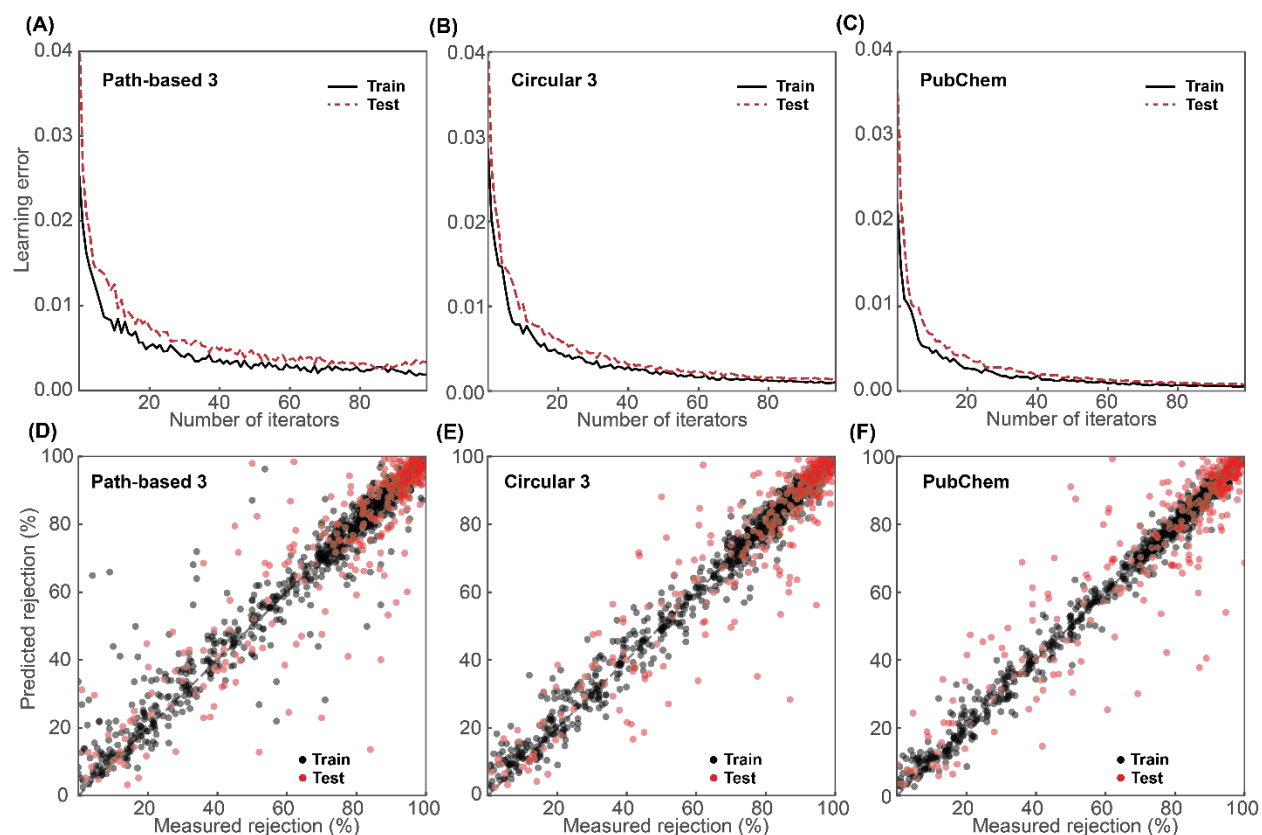
Figure 2.2 Learning curves and Q-Q plots of models trained with different molecular fingerprints. The maximum path length and bit length for the path-based fingerprint were 3 and 32768, respectively. The maximum radius and bit length for the circular fingerprint were 3 and 16384, respectively. The bit length of the PubChem fingerprint was 881.

Table 2.2 Training and test performances of the models with different fingerprint algorithms.

Name	Fingerprint parameter	Bit length	Train MSE	Test MSE	Train Spearman	Test Spearman	Train Pearson	Test Pearson
Path-based 3	Maximum path length 3	32768	2.60	6.03	0.98	0.91	0.96	0.84
Circular 3	Maximum radius 3	16384	1.92	5.25	0.99	0.93	0.99	0.88
PubChem	-	881	1.37	5.61	0.99	0.92	0.99	0.86

Table 2.3 Summary of previous studies using machine learning to predict contaminant rejection.

Year	Algorithm	Process	Data size	Input feature	Output feature	RMSE train	RMSE test	MAE train	MAE test	R^2 train	R^2 test	RMSE CV	R^2 CV
2000	Neural Net	NF	342	operating conditions, salt type, membrane type	solute rejection								
2008	Neural Net	RO	50	solute properties	passage/sorbed/rejected fractions								
2009	Neural Net	RO/NF	124	solute properties	solute rejection			6.113	4.56	0.91	0.97		
2015	Neural Net	RO/NF	965	solute properties, membrane properties, operating conditions	solute rejection	10.78	11.53			0.921	0.904		
2017	Neural Net	RO/NF	436	-	solute rejection								
2020	Random Forest	RO/NF	701	solute properties, membrane properties, operating conditions	solute rejection	0.025	0.092			0.947	0.907		
2020	Genetic Algorithm	NF	19	solute properties	solute rejection								
2021	Neural Net, Support Vector Machine, Random Forest	NF	38430	solute properties, membrane properties, operating conditions	solvent permeance, solute rejection	4.42	12.14			0.989	0.914		
2021	Extreme Gradient Boosting, Categorical Gradient Boosting	NF	1524	monomer, fabrication conditions, operating conditions	water permeability, solute rejection	4.17	11.74			0.980	0.840		
2022	Partial Least Square, Convolutional Neural Net	NF	38430	solute properties, membrane properties, operating conditions	solute rejection							7.95	0.89
2022	Gradient Boosting, Kernel Ridge	PV	681	molecular fragments, membrane properties, operating conditions	solvent flux, separation factor			0.077	0.126	0.995	0.987		

| This study | Extreme Gradient Boosting | RO/NF | 1906 | molecular fingerprints, membrane properties, operating conditions | solute rejection | 1.92 | 5.25 | | 0.99 | 0.88 |

2.3.2 Effect of varying fingerprint hyperparameters on model performance and bit collision

In the previous section, all three fingerprint types (path-based, circular, and structural-key) were able to produce comparable predictive performances when applied to the rejection dataset. We also found that the path-based model became susceptible to overfitting. Herein, we vary the hyperparameters of MFs (maximum path length for the path-based fingerprint, maximum radius for the circular fingerprint, and length of the pre-defined structural-keys for the PubChem fingerprint) to further investigate how the simulation conditions affect the performance and interpretability of the models. The hyperparameters control the maximum boundary of fragmentation, and hence, the molecular fragments of a compound can change based on the hyperparameter size. The default hyperparameters used in the previous section were 3 for the maximum path length in the path-based fingerprint, 3 for the maximum radius in the circular fingerprint, and 881 pre-defined structural-keys for the PubChem fingerprint, respectively. The maximum path length of 1, maximum radius of 1, and the MACCS fingerprint as a shorter structural-key fingerprint (167 keys) were additionally used to compare the performances and the changes of calculation time.

The predictive performances with different hyperparameters showed that the test Pearson coefficient of the path-based model noticeably dropped when the path length was changed from 3 to 1, with values of 0.84 and 0.78, respectively. The Pearson coefficients of the circular and PubChem models did not considerably change when lower hyperparameters were used (the coefficient varied by 0.01). In the case of the circular fingerprints, this indicates that the organic compounds in the data are not large and the circular radius of 1 was enough to represent the compounds. The Spearman coefficients, which are good at estimating monotonic association

between two variables, were similar (0.90-0.93) for different fingerprints and hyperparameters because non-linearity of Spearman makes its evaluation less restrictive than Pearson.

Table 2.4 Comparison of performance change and molecular fragments with varying hyperparameters

Fingerprint	Hyperparameter	Train Spearman	Test Spearman	Train Pearson	Test Pearson	Calculation time (s)
Path-based	3 (max. path length)	0.98	0.91	0.96	0.84	2154
	1 (max. path length)	0.96	0.90	0.93	0.78	82
Circular	3 (max. radius)	0.99	0.93	0.99	0.88	1011
	1 (max. radius)	0.99	0.92	0.99	0.89	266
Structural key	881 PubChem keys	0.99	0.92	0.99	0.86	78
	167 MACCS keys	0.99	0.92	0.98	0.87	33

Calculation time of the different fingerprints and hyperparameters was also evaluated (Table 2.4). For a given fingerprint and hyperparameter, calculating times were estimated using the shortest fingerprint bit length that avoided bit collision, which occurs when different sub-structures are stored in the same bit. Bit collision typically only happens in the hashed style fingerprints (in this study, the path-based and circular MFs) as a result of short bit lengths, and can lead to inaccurate interpretation of rejection behavior. Calculation time increases at higher bit lengths. We chose to avoid bit collision in this study since sub-structures were used for rejection analysis. The results demonstrate that the path-based fingerprint with the maximum path length of 3 with the bit length of 32768 had the longest calculation time of any of the algorithms (2154

24

seconds). The long calculation time indicates that the path-based fingerprint with the maximum length of 3 holds the highest number of combinations of sub-structures than other fingerprint cases, and it is probably the reason of overfitting in Figure 2.2A. The circular fingerprint with the maximum radius of 3 required 16384 bits for no bit collision, and its calculation time dropped to 1011 seconds compared 2154 seconds of the path-based fingerprint with the path length of 3. Structural-key fingerprints including PubChem and MACCS were light compared to other fingerprints in terms of bit length and calculation time. Their lengths were below 1000 bits, and the calculation times were only 78 and 33 seconds for PubChem and MACSS, respectively.

Overall, the analysis of various MF types and hyperparameters showed the Pearson and Spearman coefficients of PubChem, MACCS, and circular fingerprint models were all similarly high. However, path-based fingerprints gave somewhat lower prediction performance. We hypothesize that this is because the path-based fingerprint case with a high maximum path length suffered from overfitting, even with the training algorithm minimizing overfitting, due to abundant sub-structure information, and the path-based fingerprint case with a low maximum path length was struggling with brining meaningful sub-structures to predict rejection. Circular and structural key fingerprinting were able to produce higher prediction performances than the path-based fingerprint cases. Structural key fingerprints had the lowest calculation times, as the shorter structural keys of MACCS were fast to compute and convenient to use because of the pre-defined keys. MACCS may therefore be preferred over other fingerprints such as PubChem, circular, and path-based fingerprints to analyze membrane rejection of organic compounds because of the combination of performance and speed.

2.3.3 Model interpretation with SHAP and clustering analyses

In this subsection, the interpretability of each algorithm is investigated by evaluating the importance of molecular fragments and input features using SHAP analysis. In addition, we demonstrate how the relation between molecular fragments and rejection mechanisms can be derived using a clustering technique with the MACCS fingerprint to examine the rejection behavior of each cluster and understand what molecular fragments make them similar or different.

SHAP importance scores were compared for the three MF algorithms (path-based, circular, and structural key) with different hyperparameters (Figure 2.3). All cases show very clear trends correlating rejection with membrane molecular weight cut-off (MWCO) and pH with importance scores of 0.49 and 0.16, respectively. High MWCO increased steric rejection of compounds. High pH increased rejection since a high pH shifts membranes and some compounds toward negative charge. Thus, the higher pH enhances electric repulsion between membranes and the compounds.[72] Other membrane properties and operating conditions including contact angle, operating pressure, type of membrane, and measurement time did not show consistent trends with all algorithms.
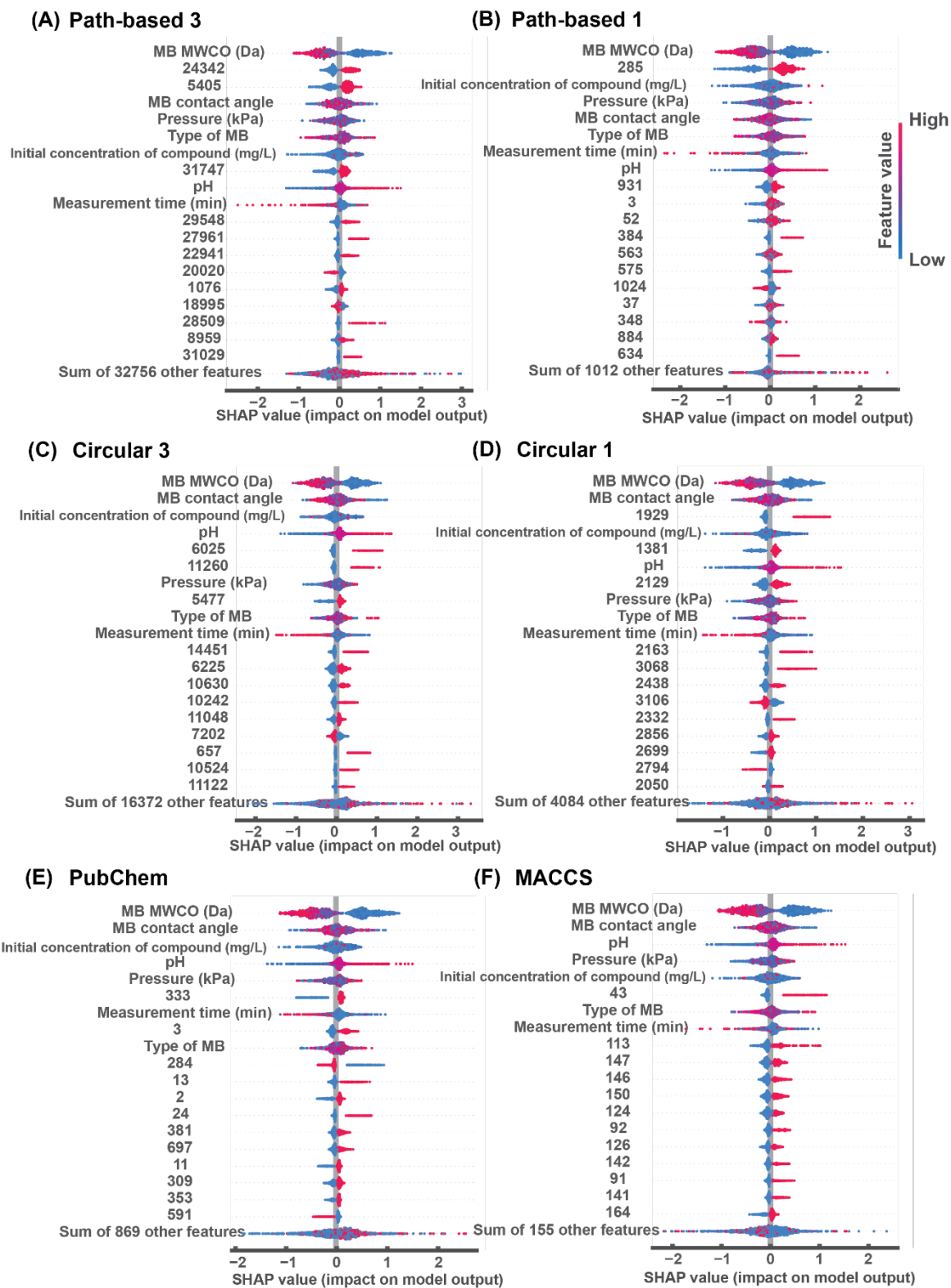
Figure 2.3 Comparing the SHAP importance scores of input features on membrane rejection over different fingerprints and parameters.

The use of molecular fingerprints and SHAP enables to show the physical implications of molecular sub-structures on membrane rejection. Figure 2.3 lists the feature codes for MFs that showed high importance scores. Some of the sub-structures with high impacts on membrane rejection were associated with molecular size or charge (structure schematics are shown in the Supporting Information). The presence of tetrahedral groups of 4 bonds from a central atom, indicating branching molecules or methyl group (285 Path-based 1, 24343 Path-based 3, 5405 Path-based 3, 113 MACCS, 2163 Circular 1, and 14451 Circular 3) led to high rejections, presumably because these characteristics increase molecular size.[73] There were functional groups frequently appearing over different fingerprints, such as carboxyl (-COOH), hydroxyl (-OH), and carbonyl (C=O) groups, that are related to electric charge and polarity. For example, organic acids (e.g. salicylic acid, clofibric acid, and benzoic acid) in the dataset contain the -COOH sub-structure. The hydrogen in -COOH can be easily deprotonated and bring a negative formal charge at neutral pH, which increased rejection due to strong electrostatic repulsion.[74] It is noteworthy that the presence of fluorine was found to be of high importance in the SHAP results (384 Path-based 1, 27961 Path 3, 24 PubChem, and 43 MACCS). However, this is likely linked to carbon chain length and size effects correlated with fluorination, rather than the effect of the fluorine itself. The dataset has 9 PFAS (perfluoroalkyl substances) compounds, and all the compounds have long carbon chains with at least 7 fluorine groups and up to 19 fluorine groups. The PFAS compounds showed high rejections of 86–98% due to their long chains (average molecular weight of PFAS compounds is 67% higher than average molecular weight of the entire data), and fluorine indirectly represented the lengths of the carbon chains.

To further investigate the association between fingerprint sub-structures and rejection, we analyzed the molecular fragments of MACCS structural key fingerprints since MACCS

28

fingerprints are possibly the most efficient candidate for studying membrane rejection based on fast computation time and accuracy. The top-ranked fragments can explain the interactions between compounds and membranes in a straightforward manner. In Figure 2.4A, the 12 most important sub-structures of MACCS and their importance scores are displayed. The importance score was obtained by averaging absolute SHAP values in Figure 2.3. MACCS features such as 113, 126, 146, and 164 were largely related to molecular volumes because the presences of tetrahedrons and rings can increase their size (e.g. the average McGowan molecular volume of compounds having tetrahedrons is 32% higher than the average McGown molecular volume of the entire data). Feature 124 represented carboxylic groups, and features 141 and 147 represented the counts of oxygen in compounds. Larger amounts of oxygen are possibly linked to negative surface charge due to oxygenated groups often having high electronegativity. Features of 91, 92, 142, and 150 were associated with alkyl chain including methyl group, which can affect size and polarity.

Clustering analysis was further used to group compounds based on their MACCS fingerprints and compare rejection behavior between clusters. Before implementing clustering, the data was divided depending on membrane weight cut-off and pH, which are two significant predictors with high importance scores, to eliminate their influences while analyzing the effect of molecular structures. A sub-dataset with MWCO less than 225 Da and pH 7 was generated, and the sub-dataset contained 176 unique compounds. Their MACCS fingerprints (167 bits) were reduced to 2 arbitrary bits by dimension reduction for visualization. Data points were labeled with 4 clusters based on t-SNE clustering algorithm to group similar compounds in Figure 2.4B. Cluster 1 had the highest average rejection (86%) in Table 2.5. The results of fingerprint feature appearance frequency (see Figure 2.4C) show that Cluster 2 is the most homogenous cluster. This is described in the standard deviation of rejection in Table 2.5. The cluster had the lowest standard

deviations for rejection and molecular weight among the four clusters. This may indicate the highest average rejection of the cluster is derived from their large sizes without high variances in their molecular structures. A few compounds in the cluster are presented in Figure S1 as examples, and they share rings and branches that can possibly expand their volumes. On the other hand, the compounds in Cluster 3 had very few rings, and their structures were mostly long chained with multiple oxygens attached. The average rejection of Cluster 3 was in between that of Clusters 2 and 4. Interestingly, the average molecular weight of Cluster 3 was lower than that of Cluster 4, but the average rejection of Cluster 3 was higher than that of Cluster 4. This is probably related to the long-chain shapes in Cluster 3 (see Figure S1), which induce a larger dimension (e.g. increasing van der Waals radius), and thus make it difficult for a compound to pass through the pore.[75] Cluster 4 was the least homogenous cluster in Figure 2.4C. It showed the lowest average rejection (61%) as well as the highest standard deviation for the rejection. The cluster included small aldehydes and alcohols as well as compounds with multiple rings that brought high rejections.[76]
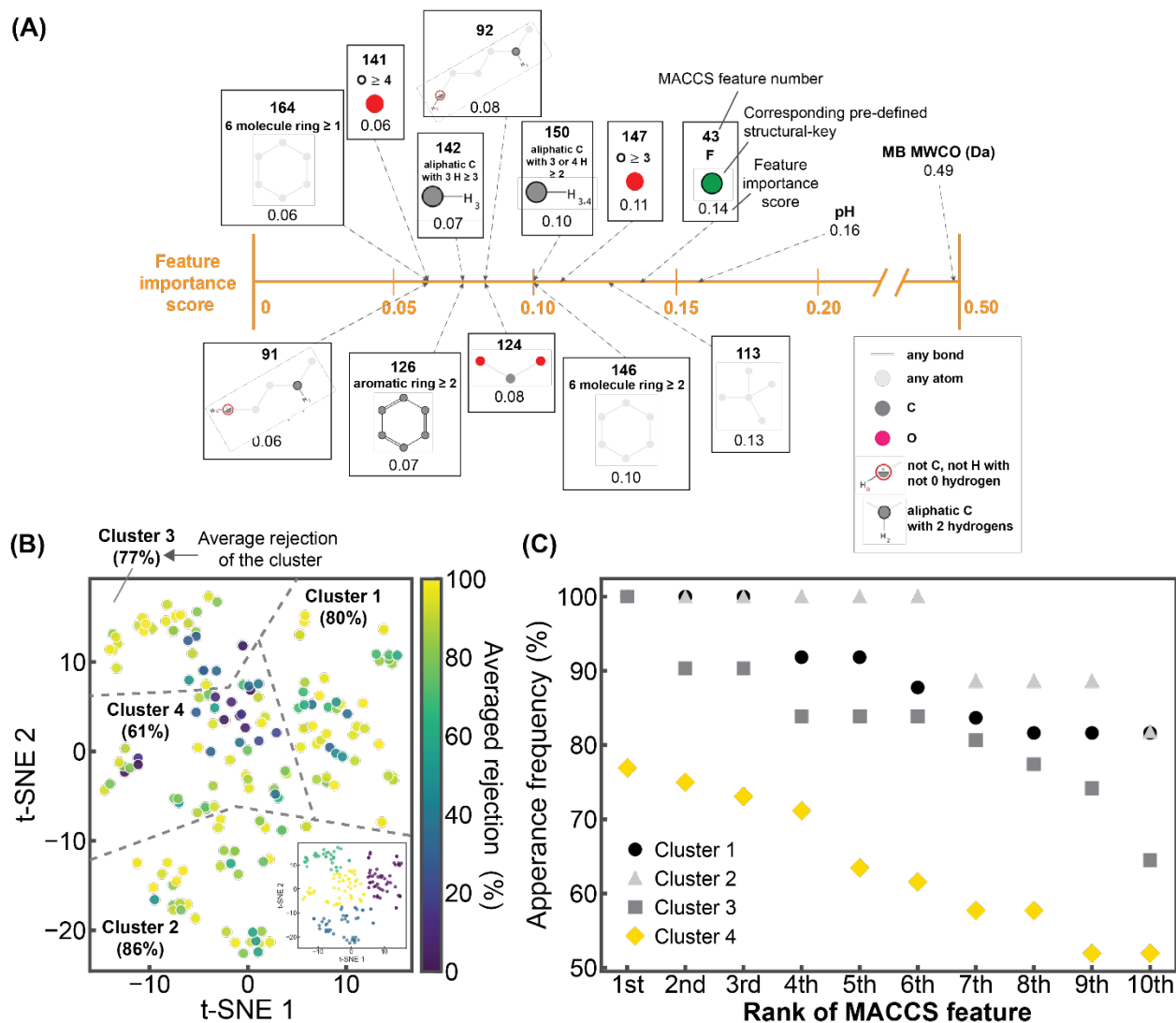
Figure 2.4 (A) Feature importance scores of the top-ranked (importance score > 0.05) MACCS molecular sub-structures obtained from the SHAP results. MWCO and pH had the first and second highest scores, so their importance scores were presented on the graph for comparison. (B) Clustering results based on MACCS fingerprint with four clusters and the MWCO < 225 Da & pH = 7 sub-dataset. (C) The appearance of all the MACCS features in each cluster was counted and converted to a percentage by dividing the count by the number of compounds in the cluster. Only top-10 frequent features were shown, and the list of the features can be found in Table S6.

31

Table 2.5 Comparing cluster characteristics with a sub-dataset (MWCO < 225 Da & pH = 7).

Name	Molecular weight (g/mol)	Compound charge	Dipole moment (debye)	log P	Avg. rejection (%)
Mean					
Cluster 1	271.91	-0.24	3.51	2.92	80
Cluster 2	274.08	-0.03	3.32	1.31	86
Cluster 3	147.86	-0.07	2.1	-1.09	77
Cluster 4	179.73	-0.15	2.96	1.79	61
Standard deviation					
Cluster 1	160.81	0.69	2.04	1.37	22.84
Cluster 2	64.73	0.68	1.75	1.68	13.72
Cluster 3	99.96	0.25	1.33	1.94	27.02
Cluster 4	94.79	0.35	1.87	1.52	33.90

2.4 Conclusions

In this work, membrane rejection was analyzed using machine learning and molecular fingerprints. We found that representing solutes with molecular fingerprints, rather than using molecular properties (e.g., dipole moment, molecular volume), resulted in high prediction accuracies. A molecular fingerprint-based approach allows for the rejection of any molecule to be determined directly without requiring the time-consuming and expensive determination of molecular properties via experiments or computation. In our analysis, the performances of three different fingerprint generation algorithms (path-based, circular, and structural key) were compared with varying hyperparameters. We found that, of these fingerprint algorithms, the MACCS structural key fingerprint offered the best combination of predictive power, calculation efficiency, and interpretability.

Our work highlights that the use of molecular fingerprints can improve our ability to understand and visualize the interactions between membranes and solutes. The importance of all the fingerprint features for determining rejection was quantified using SHAP analysis. This

analysis highlights certain molecular structures (e.g., tetrahedrons, ring structures, functional groups) that are associated with high membrane rejection. We also used clustering analysis with the MACCS fingerprint to group compounds based on their structures, and to compare rejection behavior for each cluster. The results identified common or unique sub-structures in each cluster that were related to membrane rejection. Further work may be able to further elucidate specific molecular structures that are strongly linked to solute-membrane interaction that impact membrane rejection. Eventually, the molecular-level insights into the rejection behavior can allow for the development of membranes that have tailored rejection of target compounds.

CHAPTER 3

Opportunities for high productivity and selectivity desalination via osmotic distillation with improved membrane design

3.1 Introduction

Worldwide, 3.6 billion people are living in areas that experience water scarcity at least one month per year, and this figure is expected to increase to as much as 5.7 billion people in 2050. The only available methods to provide water beyond what is available from the natural hydrological cycle are desalination and wastewater reuse.[77] Water treatment processes utilizing osmotic membranes play a key role in advanced water treatment because of their high energy efficiency and product water quality. Compared to conventional thermal desalination processes, membrane systems consume nearly two orders of magnitude less energy in seawater desalination.[78] As a result, membrane systems have seen growing implementation, with capital investments in reverse osmosis growing by 15% per year.[79] Furthermore, osmotic membrane systems will likely experience growth in emerging applications such as drug purification, protein concentration, and food processing.[80–83]

Despite the growing use of membrane-based water treatment systems, inadequate selectivity of membrane materials often hinders their effectiveness. Current osmotic membranes utilize thin polymer films as selective layers, and these films are inherently constrained by a permeability-selectivity trade-off where improvements in membrane permeability are unavoidably met with detrimental losses in selectivity.[84] This phenomenon is inevitable in dense polymers since a high permeability is usually accomplished by increasing the diffusion coefficient for water which

also leads to concurrent increases in the permeability of other dissolved compounds.[85] In addition to suffering from permeability-selectivity constraints, state-of-the-art polyamide membranes poorly reject low molecular weight solutes with neutral charge. This presents issues in seawater desalination and wastewater reuse, where achieving adequate removal of boron, chloride, and micropollutants requires costly secondary treatment steps.[86,87] Low rejection of urea (less than 60%) also prevents the use of reverse osmosis in urine concentration and key separations in the food and medical industries.[88]

The need for improvements in the selectivity of osmotic membranes has motivated the exploration of numerous new membrane materials, but most of these efforts have yet to produce membranes that can outcompete conventional polyamide. One type of membrane that has demonstrated success is the hydrophobic porous membrane, which is utilized in osmotic distillation (OD) systems. When immersed in water, the hydrophobic membrane traps air within its pores, forming a microscopic air layer between the feed and permeate streams. Transport across this air layer can only occur in the gas phase, meaning that the membrane offers complete rejection of all non-volatile species.[89,90] The phase-change process liberates OD from the permeability-selectivity trade-off. Therefore, unlike existing processes using dense polymer membranes, it is theoretically possible to achieve high permeability and near-perfect rejection simultaneously.[91]

Osmotic distillation membranes are implemented in a process analogous to forward osmosis (FO), where the membrane is placed between a low salinity feed stream and a high salinity draw stream. The difference in chemical potential, manifested in a partial vapor pressure difference, drives water molecules from the feed to the draw solution. The lack of an applied hydraulic pressure or heating in OD means it is considered an amenable process to separate compounds sensitive to pressure and heat such as foods and juices.[92–94] Osmotic distillation also shares many

of the advantages of FO, such as an ability to treat high salinity waters and feed water with high fouling potential.[95] Unlike FO, OD does not suffer from high reverse solute leakage, obviating the need for extra process steps for draw solution recovery or replenishment.

Although there is significant potential for OD, previous work on the process has observed low fluxes and poor efficiencies.[96–98] The meager performance is predominantly due to the use of membranes that are not optimized for the process. Most membranes tested have been developed for air filtration or thermal distillation and do not have suitable properties for OD. The large thickness (greater than 30 μm) of current membranes creates a long diffusion path for vapor molecules, resulting in water permeability coefficients 2–4 orders of magnitude lower than conventional polyamide membranes used in FO. For example, OD studies using hydrophobic membranes with thicknesses of 30–100 μm observed water permeabilities equivalent to between 4×10^{-4} and 8×10^{-4} kg m^{-2}h^{-1}bar^{-1}, whereas typical polyamide FO membrane permeabilities are 1–4 kg m^{-2}h^{-1}bar^{-1}.[98–101] Furthermore, thick membranes are thermally insulating, promoting undesirable temperature accumulation on either side of the membrane as heat is transferred in the enthalpy of vaporization. Thinner membranes are known to improve OD performance by decreasing the vapor transport path and increasing the thermal conductivity, but the optimal membrane properties (e.g., thickness, porosity, and pore radius) have not been systematically studied and compared to conventional desalination membranes.

In addition to the need to understand optimal membrane properties, the impact of heat accumulation on OD system performance is poorly understood. Although OD is regarded as an isothermal process, evaporation and condensation of water vapor cause temperature polarization, which lowers the partial vapor pressure difference driving water permeation.[102] In large-scale systems, heat accumulation occurs as the bulk feed temperature decreases and the draw

36

temperature increases, eventually reducing water flow in the system. Such heat accumulation effects have been shown to decrease the water flux of membrane modules by more than 30%.[103] Thus, any efficient OD system must be designed with knowledge of appropriate thermal management criteria to prevent temperature polarization and accumulation.

In this work, we examine optimal membrane properties and heat transfer effects in OD via element- and module-scale computations. First, we investigate the achievable water flux of OD membranes, focusing on the impact of membrane thickness, heat transfer properties, and polarization effects. We then develop a module-scale OD model to simulate mass and heat transfer in realistic systems. This model is used to probe the impact of heat and salt accumulation in the membrane module. We also consider the impacts of membrane properties including thickness, porosity, thermal conductivity, and pore radius on the desalination performance of OD systems. Finally, the performance of optimized OD membranes is compared to that of conventional thin-film composite membranes used in FO. Our analysis provides critical insights into design principles for future OD systems that can potentially outcompete conventional membrane processes.

3.2 Mass and heat transport model for osmotic distillation systems

3.2.1 Water and heat transfer across hydrophobic membranes

The overall water and heat transport across the hydrophobic vapor-gap membrane is shown in Figure 1. The membrane has pores filled with air and water vapor that become pathways for water vapor flow through the membrane, J_w, which is driven by a difference in the partial vapor pressure of water, P_v, that depends primarily on the salt concentrations at the feed and draw membrane interfaces ($C_{f,m}$ and $C_{d,m}$, respectively). The concentration difference across the membrane leads to

a net flux of water from the feed to the draw reservoir, and the associated evaporation and condensation of water molecules induces convective and conductive heat transport. Convective heat transport occurs when the water molecules carry the latent heat of vaporization, H_{vap}, through the membrane to cool the feed stream and heat the draw stream. The formation of a thermal gradient across the membrane then induces conductive heat transfer as heat is transported back toward the feed, the rate of which depends on the thermal conductivity of the membrane, K_m, the membrane thickness, d, the temperature at the feed membrane interface, $T_{f,m}$, and the temperature at the draw membrane interface, $T_{d,m}$. The sum of convective and conductive heat is the net heat flux, q. The transport of water and heat is expressed as:[104]

$$J_w = B[P_v(T_{f,m}, C_{f,m}) - P_v(T_{d,m}, C_{d,m})] \tag{1}$$

$$q = J_w H_{vap} + \frac{K_m}{d}(T_{f,m} - T_{d,m}) \tag{2}$$
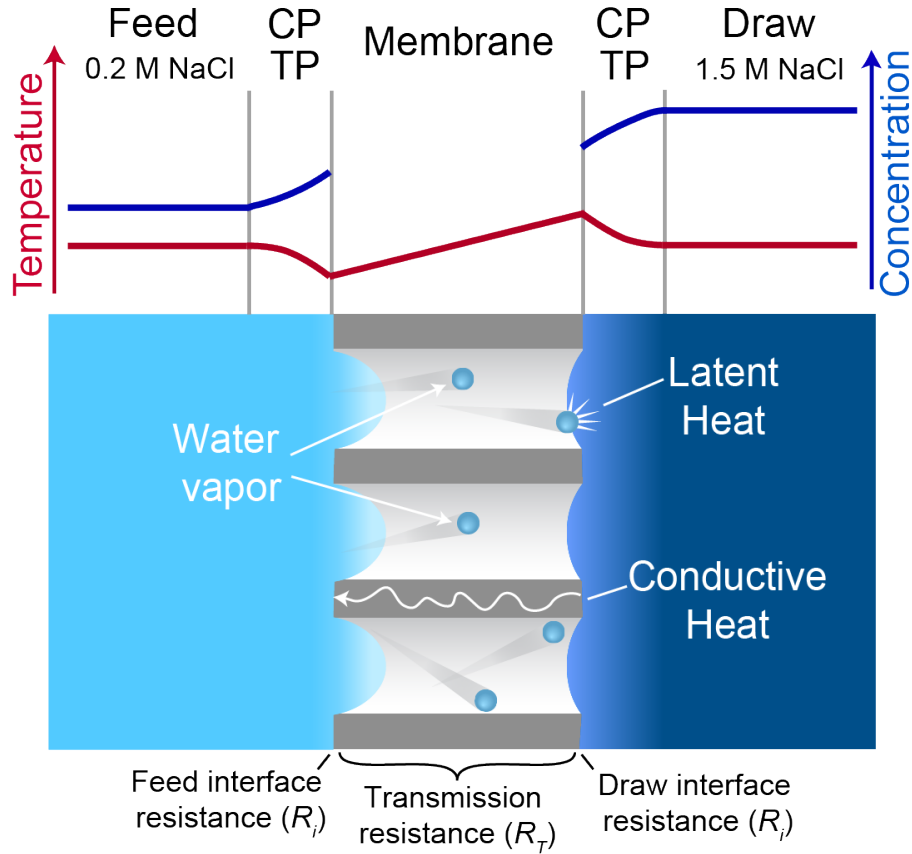
Figure 3.1 Conceptual diagram of mass and heat transfer in osmotic distillation. Water vapor evaporates on the feed air-liquid interface, diffuses through the air gap in the membrane, and condenses on the draw side. Water molecules carry the latent heat of vaporization across the membrane, and the transmembrane temperature difference results in conductive heat transfer from the draw to the feed. Temperature and concentration profiles are shown (red and blue lines, respectively). Concentration polarization (CP) and temperature polarization (TP) occur in boundary layers on both sides of the membrane.

The vapor permeability, B, is determined by incorporating Hertz hypothesis and total transport resistance:[105,106]

$$B = \varepsilon \sqrt{\frac{M_w}{2\pi R_g \bar{\bar{T}}}} \left[R_t + R_{i,f} + R_{i,d}\right]^{-1} \tag{3}$$

where the total resistance is determined by the transmission resistance, R_t, the interface resistance on the feed side, $R_{i,f}$, the interface resistance on the draw side, $R_{i,d}$, the membrane

porosity, ε, the ideal gas constant, R_g, the molecular weight of water, M_w, and the average temperature of both membrane surfaces, $\bar{T}$.

Transmission resistance, R_t, arises from collisions that occur as water molecules pass through the membrane pores. Transmission resistance is the inverse of effective transmission probability, η_{eff}, and can also be expressed using the effective diffusion coefficient, D_{eff}, and the mean speed of water vapor, $\bar{v}_w$.[106]

$$R_t = \frac{1}{\eta_{eff}} = \frac{\bar{v}_w d}{4 D_{eff}} \tag{4}$$

The collisions that cause transmission resistances can be described using two diffusion regimes.[107,108] In molecular diffusion, transport resistances are dominated by collisions between water and air molecules, whereas Knudsen diffusion involves interactions between water molecules and pore walls. The transition between the two regimes is defined by the membrane pore size and mean free path of water vapor. When the size of the pore is larger than the mean free path of the vapor (60-100 nm at atmospheric pressure),[109] the system is in the molecular diffusion regime. In contrast, if the membrane has smaller pores than the mean free path, the system is in the Knudsen regime. Thus, the equation for the effective diffusion coefficient, D_{eff}, contains terms for molecular diffusion and Knudsen diffusion. D_{eff} can be approximated by:

$$D_{eff} \approx \left[\frac{1 - \frac{p_0(\bar{T})}{p_t}}{D_{wa}} + \frac{1}{D_{wM}} \right]^{-1} \tag{5}$$

where $\frac{p_0(\bar{T})}{p_t}$ is the mole fraction of water vapor assumed by comparing the pure water vapor pressure and the total pressure of water and air in the pores, $\bar{T}$ is the mean temperature of the feed

and draw sides, p_t is the total pressure inside the pores, and $p_0(\bar{T})$ is the equilibrium water vapor pressure at a given temperature. This approximation is valid when the operating temperature range falls between 20 and 80 °C.[106] D_{wa} represents the binary (water-air) diffusion coefficient of water vapor, which reflects the molecular diffusion contribution to resistance, and D_{wM} represents the Knudsen diffusion coefficient of water vapor across the membrane.

$$D_{wa} = \frac{cT^{\frac{3}{2}}}{(p_t l_{wa}^2 \Omega_D)}\left[\frac{1}{M_w} + \frac{1}{M_a}\right]^{\frac{1}{2}} \tag{6}$$

$$D_{wM}\frac{\Delta C}{d} = \frac{\eta \bar{v}_w \Delta C}{4} \tag{7}$$

$$D_{wM} = \frac{\eta \bar{v}_w d}{4} \tag{8}$$

$$\eta = 1 + \left(\frac{L^2}{4}\right) - \left(\frac{L}{4}\right)(L^2 + 4)^{\frac{1}{2}} \tag{9}$$

$$- \frac{\left[(8 - L^2)(L^2 + 4)^{\frac{1}{2}} + L^3 - 16\right]^2}{72L(L^2 + 4)^{1/2} - 288\ln[L + (L^2 + 4)^{1/2}] + 288\ln 2}$$

D_{wa} is expressed based on previous studies,[106] where a characteristic length, l_{wa}, is obtained by the Lennard-Jones 12-6 potential. The constant, c, is an empirical constant, and the collision integral, Ω_D, is for mass diffusion. Both D_{wM} and D_{wa} depend on temperature, and thus,

transmission resistance and vapor permeability are also temperature-dependent. Knudsen diffusion coefficient, D_{wM}, in Equation 8 is determined by equating the mole flux calculated from the transmission probability, η, (the right-hand side of Equation 7) with the flux calculated from the diffusion equation (the left-hand side of Equation 7).[110] The transmission probability, η, in a cylindrical tube was determined using the aspect ratio, L, which is defined as the pore length divided by the pore radius.[106] Substituting Equation 6 into Equation 5 defines transmission resistance, R_t, as following:

$$R_t = \frac{(1 - \frac{p_0(\bar{T})}{p_t})\bar{v}_w d}{4D_{wa}} + \frac{1}{\eta} \tag{10}$$

Interface resistance, R_i, occurs because vapor molecules can be reflected at the gas-liquid interface and is expressed using the condensation coefficient, σ, which is the probability of water vapor condensation into bulk liquid at the gas-liquid interface.[111]

$$R_i = \frac{1 - \sigma(T)}{\sigma(T)} \tag{11}$$

For thick membranes, transmission resistances greatly outweigh resistances at the interfaces. However, it has been shown interface resistances are a critical consideration for thin and highly permeable membranes with low transmission resistances.[106] Interface resistance is a function of temperature because higher temperatures result in increased energy levels of water vapor that lead to a higher probability of reflection at the gas-liquid interface.[112] Since the feed and draw side surface temperatures change during the evaporation and condensation of water molecules, the feed interface and draw interface resistances are calculated separately.

3.2.2 Concentration and temperature polarization

The temperature and salt concentration at the membrane surface differs from the bulk solution due to polarization effects, which ultimately decrease the partial vapor pressure difference between the feed and draw solutions. Temperature gradients induced by convective heat transfer are termed temperature polarization (TP). In the OD process, TP reduces the temperature of the membrane surface on the feed side and increases the temperature of the membrane surface on the draw side. As a result, the vapor pressure gap between the feed and draw declines. The membrane surface temperatures for the feed and draw are expressed as:

$$T_{f,m} = T_{f,b} - \frac{q}{h_f} \tag{12}$$

$$T_{d,m} = T_{d,b} + \frac{q}{h_d} \tag{13}$$

where $T_{f,b}$ and $T_{d,b}$ denote the bulk temperature of the feed and draw, respectively, and $T_{f,m}$ and $T_{d,m}$ are the membrane surface temperature of the feed and draw. The extent of TP is related to the feed and draw heat transfer coefficients, h_f and h_d, and the net heat flux, q. High heat transfer coefficients mitigate the development of TP and high membrane thermal conductivity relieves TP by lowering the net heat flux (Equation 2). The heat transfer coefficient is determined by the hydrodynamic conditions of the system. In our work, a heat transfer coefficient, h, of 1000 W m^{-2}K^{-1} for feed and draw was assumed because it is a representative value for laminar flow derived from experiments in the literature.[113]

Concentration polarization occurs when the concentration at the membrane surface is different from the concentration of the bulk solution. On the feed side of the membrane, rejected solutes build up at the air-water interface, leading to a higher concentration at the interface than in the bulk solution.[114] On the draw side of the membrane, water molecules that condense at the air-

water interface dilute the concentration compared to the bulk. CP decreases the concentration difference between the two membrane interfaces, lowering the partial vapor pressure difference driving water transport. The concentrations at the membrane surfaces are given by:

$$C_{f,m} = C_{f,b} \exp\left(\frac{J_w}{k}\right) \tag{14}$$

$$C_{d,m} = C_{d,b} \exp\left(\frac{J_w}{k}\right) \tag{15}$$

where $C_{f,b}$ and $C_{d,b}$ denote the bulk concentrations of the feed and draw, respectively, and $C_{f,m}$ and $C_{d,m}$ represent the surface concentrations. The mass transfer coefficient, k, which quantifies hydrodynamic mixing along the membrane surface, and the water flux, J_w, are factors affecting the extent of CP. In our work, k is fixed at 0.0278 kg m^{-2}s^{-1} based on values obtained from the literature.[115]

We note that this analysis used fixed mass and heat transfer coefficients as a simplifying assumption for the modeling (1000 W m^{-2}K^{-1} and 0.0278 kg m^{-2}s^{-1} for the heat and mass transfer coefficient, respectively). Such an assumption of constant heat and mass transfer coefficients is commonly used in studies on membrane-based systems.[106,116–119] A sensitivity analysis showed that variation of the heat transfer coefficient from 500-22000 W m^{-2}K^{-1} and the mass transfer coefficient from 0.020-0.042 kg m^{-2}s^{-1} had less than a 5% impact on the water flux.

Percentage contributions of TP and CP to flux reduction were obtained to quantify their impacts on performance using the following equations:[120]

$$TP = \frac{\Delta P_{v,b} - \Delta P_{v,m,T}}{\Delta P_{v,b}} \times 100 \tag{16}$$

$$CP = \frac{\Delta P_{v,b} - \Delta P_{v,m,C}}{\Delta P_{v,b}} \times 100 \qquad (17)$$

$$PE = TP + CP \qquad (18)$$

where $\Delta P_{v,b}$ is the vapor pressure difference between the feed bulk and draw bulk solutions, $\Delta P_{v,m,T}$ is the vapor pressure difference between the feed membrane surface and draw membrane surface considering only temperature polarization effects, and $\Delta P_{v,m,C}$ is the vapor pressure difference between the feed membrane surface and draw membrane surface considering only concentration polarization effects. PE is the total polarization effect summing TP and CP.

3.2.3 Numerical simulation of module-scale performance

Analysis of large-scale membrane modules allows us to gain insights into the achievable water recovery and the bulk temperature or concentration changes, all of which cannot be determined solely using element-scale analysis. In this study, we model a counter-current flow membrane module, which has been shown to be the most efficient configuration in previous studies of similar processes and reduces the detrimental impacts of concentration and temperature accumulation.[121,122]

The differential equations representing mass and heat transfer in the system were discretized using a finite difference method. Three differential equations were used to determine the heat flux, flow rates, and concentrations along the membrane module:

$$\frac{dQ_f(A)}{dA} = \frac{dQ_d(A)}{dA} = J_w(T_{f_m}(A), T_{d_m}(A), C_{f_m}(A), C_{d_m}(A)) \qquad (19)$$

$$\frac{d[Q_f(A)h_L(T_f(A))]}{dA} = \frac{d[Q_d(A)h_L(T_d(A))]}{dA} \qquad (20)$$

$$= q(T_{f_m}(A), T_{d_m}(A), C_{f_m}(A), C_{d_m}(A))$$

$$\frac{d[Q_f(A)C_f(A)]}{dA} = \frac{d[Q_d(A)C_d(A)]}{dA} = 0 \qquad\qquad (21)$$

where Equation 19 expresses the volumetric balance of water, Equation 20 represents the heat balance of convective and conductive fluxes, and Equation 21 accounts for mass balance of salt. The balanced equations were solved using the modified Powell method in conjunction with the element-scale analysis. The boundary conditions for numerical solutions were $Q_f(0) = Q_{f,0}$, $Q_d(N) = Q_{d,0}$, $T_f(0) = T_{f,0}$, $T_d(N) = T_{d,0}$, $C_f(0) = C_{f,0}$, and $C_d(N) = C_{d,0}$. The calculated water and heat fluxes over the entire module were used to obtain water recovery, bulk concentrations, and bulk temperatures with varying operation conditions and membrane properties. The computational approach for element- and module-scale modeling is a well-established method in the literature and has been used to simulating different membrane processes including MD and FO.[115,117,123–126]

Unless otherwise noted, the feed solution in all simulations is modeled as having the osmotic pressure and diffusive properties of a 0.2 M NaCl solution and the draw solution is 1.5 M NaCl. Although operating with sodium chloride on both sides of the membrane is impractical, the salinity of this solution pairing serves as a representative model of brackish water desalination or food concentration.[93,127]

3.2.4 Pore wetting criteria

Wetting of membrane pores is a critical consideration because it compromises the selectivity and water flux of the membrane. Liquid penetration into the vapor-gap pores is determined by the pore radius, membrane thickness, surface hydrophobicity, and external applied pressure. In order to prevent wetting and maintain the air gap, the pore size must be sufficiently narrow and the external

pressure must be smaller than the liquid entry pressure, which is calculated by the Young-Laplace equation (Equation 23).[128,129] The pore must also be sufficiently long to prevent wetting of the membrane because there is risk that the meniscus on the feed side and the meniscus on the permeate side of the membrane will come in contact at low thicknesses. This type of wetting is dependent on the aspect ratio of the pore (i.e., membrane thickness, d, divided by pore radius, a), and pore wetting becomes thermodynamically favorable below the critical aspect ratio. In our analysis, we assume the pore length equals the hydrophobic layer thickness (i.e., the membrane has cylindrical pores with a tortuosity of 1). For the membrane to operate without wetting, a minimum aspect ratio must be met:[106]

$$\left(\frac{d}{a}\right)_{min} > \frac{2}{3(cos\theta - cos\theta_{eq})}\left(\frac{1}{1+sin\theta} + sin\theta\right) \tag{22}$$

$$cos\theta = \frac{-a\Delta P}{2\gamma_{LV}} \tag{23}$$

where θ_{eq} is an equilibrium water contact angle considering a partially wetted and cylindrical hydrophobic pore. We assume θ_{eq} as 110° in the calculation. θ is the angle between a tangential line to the gas-liquid interface and the pore axis in force equilibrium between surface tension and external hydraulic pressure drop across a membrane. θ was obtained in Equation 23, where ΔP is the hydraulic pressure difference across the vapor-liquid interface, which becomes the liquid entry pressure when the pores are wetted, and γ_{LV} is the surface interaction energy between the vapor and liquid phases. In our analysis, ΔP and γ_{LV} are fixed at zero and 71.99×10^{-3} N m^{-1}, respectively.[130]

3.3 Results and Discussion

3.3.1 Element-scale analysis of water flux and polarization effects

Analysis of the osmotic distillation (OD) system first focused on understanding performance at the scale of an individual element within a membrane module using models that fully describe heat and mass transfer (Equation 1 and 2). A key parameter for optimization in OD membranes is the thickness, which affects both the water permeability and thermal conductivity of the membrane. The impact of membrane thickness on the water flux is shown in Figure 3.2A. Typical hydrophobic membranes used for osmotic and membrane distillation have thicknesses between 50 and 100 µm, which offer relatively low fluxes (0.05-0.24 kg m^{-2}h^{-1}). Decreasing the thickness of the membrane led to an increase in the water flux by up to three orders of magnitude, with a maximum water flux of 92 kg m^{-2}h^{-1} for an impossibly low thickness of 0.001 µm. However, improvements in water flux were limited after the membrane thickness decreased below 0.1 µm.
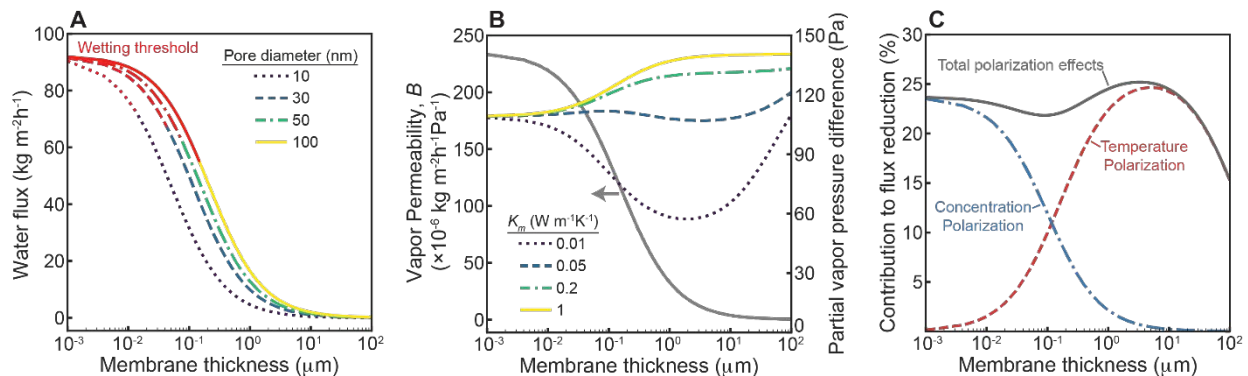
Figure 3.2 (A) Element-scale osmotic distillation water flux as a function of the hydrophobic layer thickness for membranes with different pore sizes. Red color indicates thicknesses low enough to result in membrane wetting for a given pore size. (B) Influence of hydrophobic layer thickness on the vapor permeability coefficient, *B*, and the partial vapor pressure difference across the membrane. Results are shown for membranes with different thermal conductivities. (C) Contribution of temperature and concentration polarization to the water flux reduction with different hydrophobic layer thicknesses. Feed and draw solutions were modeled as 0.2 M and 1.5 M NaCl, respectively. The bulk temperatures of the feed and draw were 298 K. Membranes were modeled with a porosity of 0.8, pore diameter of 50 nm, and tortuosity of 1. For (A) and (B), the thermal conductivity was fixed at 0.05 W m^{-1}K^{-1}.

Although very low thicknesses lead to higher achievable water fluxes, they also increase the vulnerability of the membrane to wetting. The minimum thickness possible in a membrane before wetting becomes thermodynamically favorable is dependent on both the membrane pore size and hydrophobicity (Equation 22). For hydrophobic membranes with a pore diameter of 100 nm, the minimum thickness to prevent wetting is 0.15 μm, whereas membranes with a 10 nm pore diameter can operate with a minimum thickness of 0.015 μm (indicated by red color in Figure 3.2A). The desire to decrease the pore size to achieve thinner membranes must be balanced with the increased vapor transport resistances caused by more frequent collisions with the pore walls, an effect which is manifested in the lower water fluxes of small pore size membranes. Furthermore, fabrication of a very small pore size membrane is difficult, and commercial membrane pores are typically limited to around a 30 nm pore diameter. Thus, we identify membranes with a 50 nm pore diameter and a 0.1 μm thickness as a practically feasible high-performance membrane design that can reach water fluxes of 56.5 kg m^{-2}h^{-1}. Such a membrane has a thickness that exceeds the minimum wetting thickness for a 50 nm pore size of 0.073 μm. Unless otherwise noted, our subsequent analysis utilizes membranes with this pore size and thickness.

Factors that contribute to the water flux are further described in Figure 3.2B. The water flux across the membrane is the product of the vapor permeability coefficient, B, and the partial vapor pressure difference across the membrane (Equation 1). The vapor permeability coefficient increases as the membrane thickness decreases. For a membrane thickness of 100 μm, which is in the range of current commercial hydrophobic membranes used in OD, the permeability was 3.9 × 10^{-7} kg m^{-2}h^{-1}Pa^{-1}. Decreasing the thickness to 1 μm and 0.1 μm increased the vapor permeability coefficient to 3.3 × 10^{-5} and 14 × 10^{-5} kg m^{-2}h^{-1}Pa^{-1}, respectively. Further decreasing the membrane thickness to a value of 0.001 μm, which is only possible in theory because it is below the minimum

49

wetting thickness, resulted in a water permeability of 23×10^{-5} kg m^{-2}h^{-1}Pa^{-1}, a relatively minor increase from a 0.1 μm thickness due to the increasing contribution of interface resistances at low thicknesses (Equation 11).

The dependence of the partial vapor pressure on thickness is more complicated than permeability and heavily influenced by the thermal conductivity of the membrane. Four thermal conductivity values were investigated. A thermal conductivity of 0.05 W m^{-1}K^{-1} corresponds to a high porosity polymeric material typically used in OD (e.g., expanded polytetrafluoroethylene or polypropylene), whereas a thermal conductivity of 0.2 W m^{-1}K^{-1} corresponds to a dense polymer material. Thermal conductivities of 0.01 and 1 W m^{-1}K^{-1} were selected as extreme values corresponding to insulators and highly conductive materials, respectively. Membranes with a high thermal conductivity (0.2 W m^{-1}K^{-1} or greater) only show a decrease in the partial vapor pressure difference as the membrane approaches thicknesses below 1 μm. These low thicknesses result in higher water fluxes and enhance the detrimental impact of concentration polarization (CP), which occurs as pure water transferred across the membrane dilutes the draw solution and concentrates the feed solution, decreasing the partial vapor pressure difference across the membrane. For membranes with low thermal conductivity, the partial vapor pressure difference is reduced even at higher thicknesses (~10 μm) due to enhanced temperature polarization (TP). TP is caused by the enthalpy of vaporization carried across the membrane by the water vapor flux, which heats the permeate side of the membrane and cools the feed side, resulting in a lower partial vapor pressure difference across the air gap. Increasing the thermal conductivity aids in counteracting some of the effects of TP by transferring heat back to the feed side of the membrane through thermal conduction.

To better elucidate the contribution of polarization effects on membrane performance, the relative impacts of temperature and concentration polarization were plotted in Figure 3.2C for a membrane with a thermal conductivity of 0.05 W m^{-1}K^{-1}, which is representative of a typical porous polymeric membrane. Simulations found that TP dominated the flux reduction for thicknesses in the range of current commercial hydrophobic membranes (50–100 μm), with less than 1% contribution from CP to flux reduction. Thick membranes have low conductive heat flux that exaggerates the impact of TP. The low water flux in thick membranes also results in near-negligible CP. As the membrane thickness decreases, there is more conductive heat transferred through the membrane which substantially reduces the impact of TP. However, the high water flux across a thin membrane significantly dilutes the surface concentration of the draw side, which aggravates CP.

Overall, element-scale analysis shows that very thin membranes can facilitate water fluxes that exceed 50 kg m^{-2}h^{-1}, but membranes thinner than 0.1 μm may be impractical due to increased risk of membrane pore wetting. Reducing the thickness from that of normal commercial membranes (50 μm) to 0.1 μm will result in at least two orders of magnitude increase in the flux achievable. For thicker membranes (1–100 μm), high thermal conductivities are desirable to reduce the detrimental impact of TP. However, the effect of thermal conductivity on water flux in thinner membranes is minor. Instead, the main performance limiting effect in thin OD membranes is concentration polarization, which is an unavoidable phenomenon that also hinders the performance of conventional forward osmosis processes.

3.3.2 Module-scale analysis simulating concentration and temperature accumulation

Performance of large-scale OD modules differs from that of small-scale membrane elements because the concentration and temperature vary along the length of a module as mass and heat are transferred through the membrane (Figure 3.3A). To simulate the performance of large-scale modules, element-scale transport models used in the previous section were incorporated into module simulations based on heat and mass balance (Equations 19–21). Such module-scale simulation allows for the determination of bulk concentration, temperature, and flow rate at any given point along the length of a module with finite membrane area. This analysis enables us to probe the impact of heat accumulation and bulk concentration changes with different operation parameters, membrane properties, and module areas.
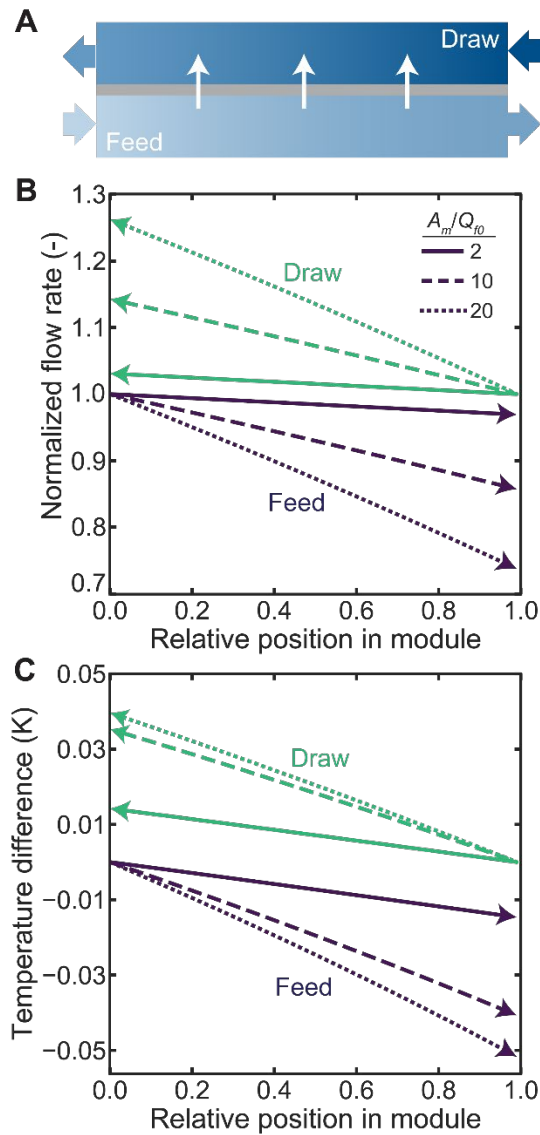
Figure 3.3 (A) Schematic of a countercurrent flow osmotic distillation module. Darker shading indicates higher salinity. (B) Normalized flow rate of the feed and draw along the length of a membrane module. Flows in the feed (teal lines) and draw (purple lines) are shown for membrane modules with different areas. (C) Feed and draw bulk temperature profile along the module length. The y-axis shows the deviation of the bulk temperature from the initial value of 298 K. Membrane thickness, porosity, pore diameter, and thermal conductivity were fixed at 0.1 μm, 0.8, 50 nm, and 0.05 W m^{-1}K^{-1}, respectively. The feed and draw solutions were 0.2 M and 1.5 M NaCl, respectively.

Flow rate and temperature along the length of a membrane module are shown in Figure 3.3B and C. Feed flow rate declined and draw flow rate increased along the length of the module due to water permeation. Larger membrane areas resulted in more permeation and greater changes

in the flow rates. Bulk temperature accumulation in OD systems is also a key consideration since each molecule of permeating water vapor carries across the heat of vaporization. Temperature on the feed side decreased along the module length due to the vaporization of water whereas the draw side temperature increased due to the release of heat during condensation. The largest temperature gap between the feed and draw was about 0.1 K, which corresponds to a reduction in the partial vapor pressure driving force of 13%. These results show that both concentration and temperature accumulation occur on either side of the membrane module resulting in reductions in the available partial vapor pressure difference that drives water flow.

For module scale systems, water recovery is a crucial performance metric that describes the fraction of the initial feed flow rate that has permeated through the membrane. Figure 3.4A shows the water recovery possible in modules with varying membrane area and draw concentrations. For a given draw concentration, increasing the membrane area resulted in higher achievable recoveries since more water is transferred across larger membrane areas. For example, while a normalized area $(\frac{A_m}{Q_{fo}})$ of 10 m^2h L^{-1} yielded recoveries in the range of 0.08 to 0.22, a normalized area of 20 m^2h L^{-1} yielded recoveries in the range of 0.15 to 0.4. Higher draw concentrations increased the driving force for permeation across the membrane, which resulted in higher water recoveries. In general, the recoveries possible in the OD system were consistent with those of previous studies on FO.[131,132]
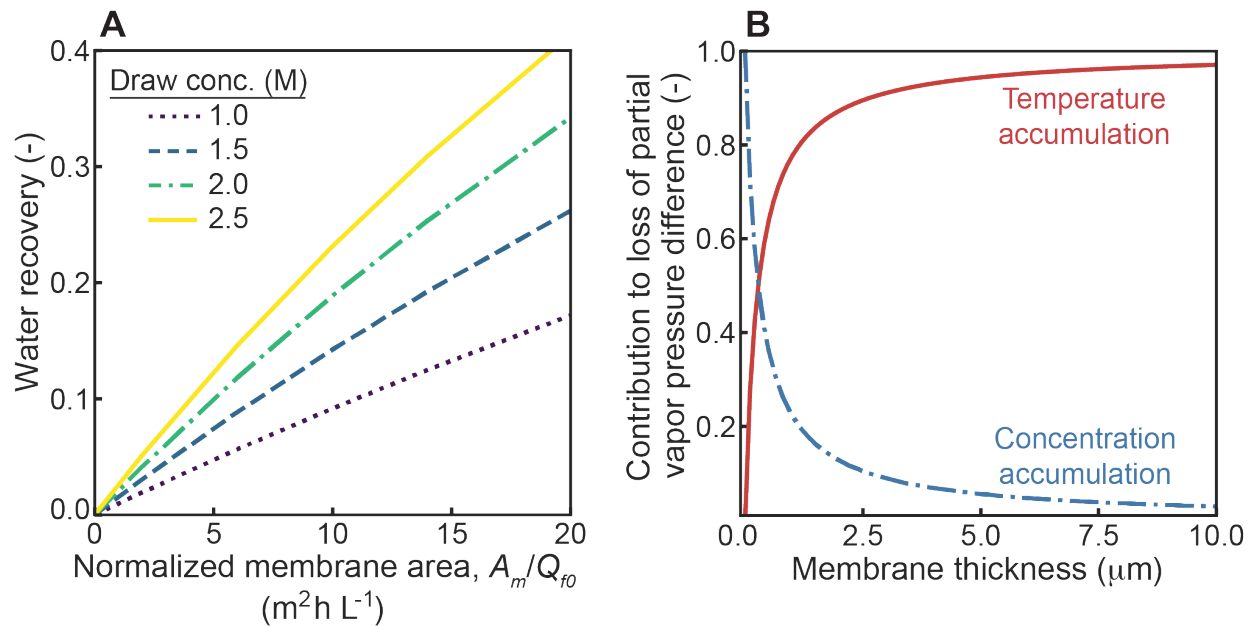
Figure 3.4 (A) Achievable water recovery with varying draw concentration and normalized membrane area, $\frac{A_m}{Q_{f0}}$, in the module. (B) Contribution of bulk changes in temperature and concentration to losses in the partial vapor pressure difference across the membrane. Accumulation effects are shown as a function of the membrane thickness. The initial temperatures of the feed and draw solutions were 298 K. Membrane thickness, porosity, pore diameter, and thermal conductivity were fixed at 0.1 μm, 0.8, 50 nm, and 0.05 W m^{-1}K^{-1}, respectively. Unless otherwise indicated, the feed solution was 0.2 M NaCl and the draw solution was 1.5 M NaCl.

Operation of module-scale OD will result in concentration and temperature accumulation effects that are not seen in element-scale systems. As was shown in Figure 3.3B, water permeation through the membrane results in changes in flow rate in the feed and draw channels, which ultimately result in concentration changes: the feed increases in concentration as it moves along the length of the membrane module and the draw is diluted. Similarly, temperature accumulation effects occur as heat is transferred across the membrane in the enthalpy of vaporization, as was shown in Figure 3.3C. The ultimate result of both temperature and concentration accumulation is a reduction in the partial vapor pressure difference across the membrane. Figure 3.4B shows the relative contribution of temperature and concentration accumulation to the partial vapor pressure loss. Thicker membranes (greater than 1 μm) are thermally insulating, and temperature

accumulation dominates the partial vapor pressure loss. As membrane thickness decreases, temperature accumulation impacts become less substantial and concentration accumulation effects dominate the partial vapor pressure loss. It should be noted that concentration accumulation effects are unavoidable in module-scale systems—they must occur to reach high recoveries—while temperature accumulation is a detrimental phenomenon that is not essential to transport. Thus, the results of our analysis show that the unnecessary harmful impact of temperature accumulation, which is unique to OD systems, can be eliminated if the membrane thickness falls below a certain threshold. In our simulation scenario, this threshold thickness is around 1 μm.

3.3.3 Impact of membrane properties on module-scale performance

In the previous sections, we identified that membrane thickness is a critical parameter that impacts both element- and module-scale performance. However, membrane design for OD systems must optimize a range of available parameters beyond just thickness. The relative impact of various membrane properties on module-scale performance is shown in Figure 3.5. Four membrane properties are examined: hydrophobic layer thickness, porosity, pore radius, and thermal conductivity. Results are shown for membrane modules with varying membrane areas to encompass a wide range of scenarios.

The impact of varying the hydrophobic layer thickness alone is shown in Figure 3.5A. The thickness of 0.1 μm, which is nearly as thin as a 50 nm pore diameter membrane can be made before risking wetting, produced the highest water recovery of 0.26 with a membrane area of 20 m^2h L^{-1}. Increasing the thickness to 1 μm resulted in a decrease in the water recovery to 0.07. Further increases to 10 μm, which is in the range of current commercial hydrophobic membranes (typically 50-100 μm) yielded a low water recovery of around 0.01. Thus, low membrane

thicknesses approaching 0.1 µm are critical to improving the OD water recovery by increasing the water permeability and decreasing temperature accumulation. For membranes with a 1 µm thickness rather than 0.1 µm, more than double the membrane area will be required to reach the same recovery.
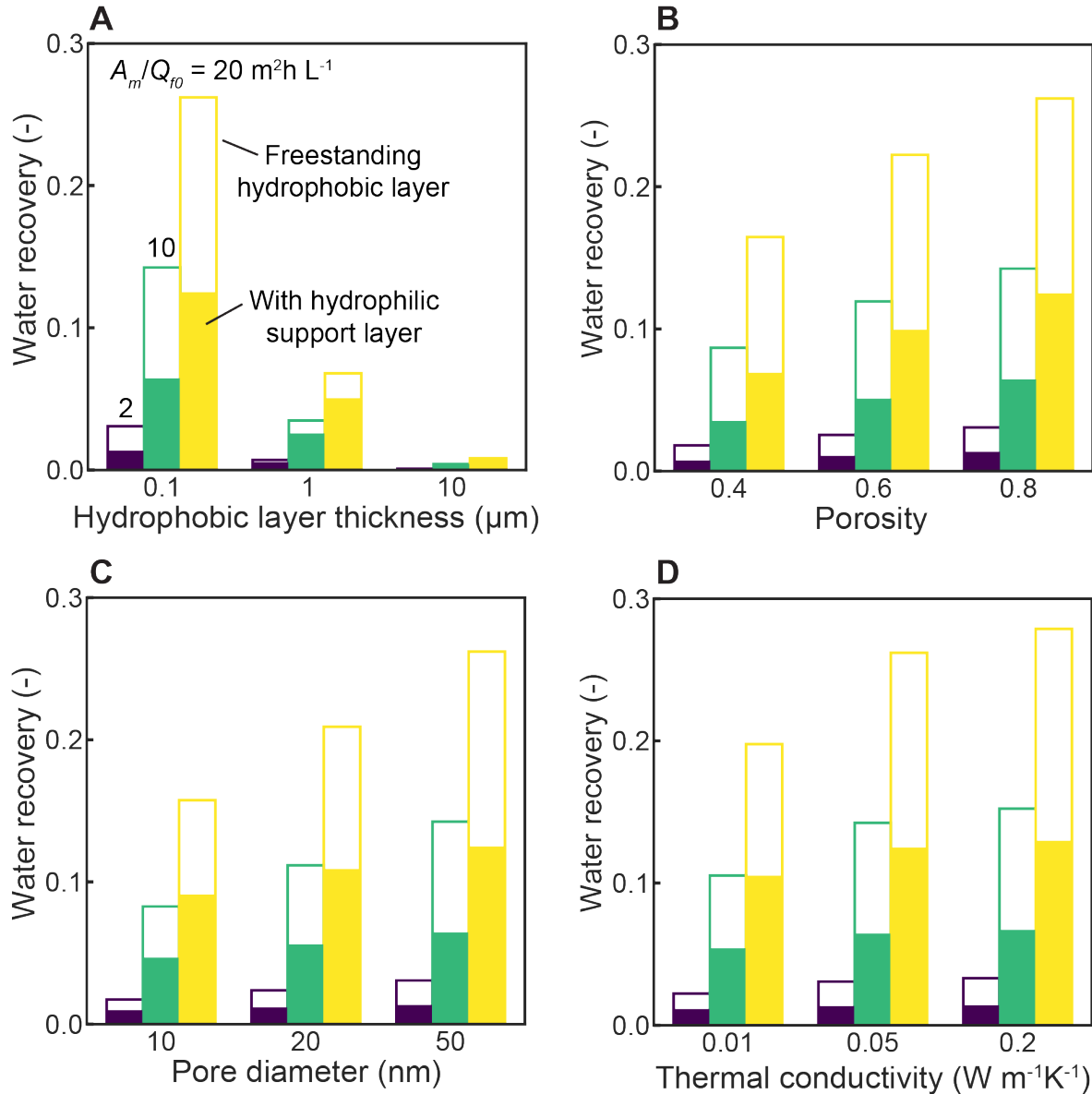
Figure 3.5 Achievable module-scale water recovery with different membrane properties: (A) hydrophobic layer thickness, (B) porosity, (C) pore radius, and (D) thermal conductivity. Each condition is shown with different normalized membrane area, $\frac{A_m}{Q_{fo}}$. Empty bars represent the performance of freestanding hydrophobic membranes whereas filled bars represent the

performance of membranes with a 150 μm thick hydrophilic support layer. Feed and draw solutions were 0.2 M and 1.5 M NaCl. Initial temperatures on both sides of the membrane module were 298 K. The default values for membrane properties were a hydrophobic layer thickness of 0.1 μm, porosity of 0.8, thermal conductivity of 0.05 W $m^{-1}K^{-1}$, and pore diameter of 50 nm.

While very low thicknesses are favorable to obtain high recoveries, membranes less than 1 μm thick are likely fragile and susceptible to rupture during practical operation. Thus, membranes were also modeled with a hydrophilic support layer on the draw side of the membrane (Figure B-S1 and Supplementary Note). This support layer does not affect the thickness of the hydrophobic layer, but does provide extra mechanical stability to the membrane. This structure of a composite membrane with a hydrophilic support layer on the draw side mimics the structure of conventional FO membranes and has already been fabricated and utilized in previous work on OD.[91,133,134] Membranes modeled with a 150 μm thick support layer are shown in Figure 3.5 (solid bars). The 150 μm thickness was chosen since it falls in the range of thicknesses of many commercial membranes.[135–137] For a 0.1 μm thick membrane, the addition of the membrane support layer reduced the achievable recovery by 52%. The support layer exaggerates CP on the draw side of the membrane by restricting hydrodynamic mixing near the hydrophobic membrane surface, leading to severe dilution of the membrane surface concentration on the draw side and a reduced partial vapor pressure difference. For the membranes with a thicker hydrophobic layer (1 μm and 10 μm), the addition of the support layer led to a less than 30% reduction in the overall recovery.

Membrane porosity is another key parameter that can impact OD performance. In Figure 3.5B, the water recoveries with three different porosities are described. Porosities of 0.4, 0.6, and 0.8 represent the typical range for polypropylene (PP), polytetrafluoroethylene (PTFE), and polyvinylidene fluoride (PVDF) hydrophobic membranes.[99,100] As shown in Equation 3,

membrane permeability increases monotonically with porosity, leading to increased recoveries. Higher porosities also result in decreased thermal conductivity due to a higher fraction of air in the pore, which would lead to increased temperature polarization.[91] In our analysis, the TP effect was overshadowed by the improved permeability with higher porosity, which resulted in a clear increase in the recovery as the porosity increased. A doubling of the porosity from 0.4 to 0.8 resulted in a 60% increase in the water recovery.

Optimization of pore diameter is needed to ensure suitable water permeability and wetting resistance of the membrane. Smaller pore sizes allow for thinner membrane hydrophobic layers, since the thermodynamic wetting criteria are dependent on the aspect ratio of the membrane pores (Equation 22). For example, a membrane with a 50 nm pore diameter can reach a minimum thickness of 0.073 μm without wetting whereas a membrane with a 10 nm pore diameter will be able to have a thickness down to 0.015 μm. While thinner membranes can be more robust, decreasing pore diameter also increases the transmission resistances of the membrane, reducing the water vapor permeability. Changing the pore diameter from 50 nm to 10 nm led to a 40% decrease in the water recovery in Figure 3.5C. Thus, the desire to create more thin and robust hydrophobic layers by using a small pore size must also account for decreases in the vapor permeability of the membrane.

Thermal conductivity is an important membrane material property dictating heat flux and accumulation in OD. Thermal conductivities of 0.01, 0.05, and 0.2 W m^{-1}K^{-1} were used for the simulations which correspond to a highly insulating material, a porous polymer material, and a dense polymer material. For the membrane simulated in Figure 3.5D, which had a relatively low thickness of 0.1 μm, the thermal conductivity only had a substantial impact at very low values (0.01 W m^{-1}K^{-1}). The thermal conductivity of 0.01 W m^{-1}K^{-1} resulted in a 25% decrease in the

water recovery compared to a thermal conductivity value of 0.05 W m^{-1}K^{-1}. Low thermal conductivity reduces the conductive heat transfer from the draw to the feed, aggravating the impact of TP and heat accumulation to decrease the partial vapor pressure difference across the membrane. We note that thicker membranes will show a more exaggerated impact of the thermal conductivity since such membranes are more insulating.

3.3.4 Comparison of desalination performance for OD and FO membranes

Osmotic distillation and forward osmosis are similar processes in that both utilize a concentration gradient across a membrane to drive flow. However, OD relies on vapor transport across a hydrophobic porous membrane whereas FO relies on sorption and diffusion of water through a dense polymer film. Compared to FO, OD offers the potential advantage of improved selectivity since vapor transport allows for distillation-quality product water. However, experimental OD systems in the literature have rarely obtained fluxes that can compete with those of conventional FO membranes since most OD membranes in the literature are not optimized to improve performance.[137,138] The subsequent analysis focuses on comprehensively comparing the desalination performance of an optimized OD membranes and high-performance commercial FO membranes.

The obtainable element-scale water fluxes in tailored OD and FO membranes with varying water permeability coefficients are shown in Figure 6A. The feed and draw solutions were 0.2 M and 1.5 M NaCl, and the initial temperatures of both sides were 298 K. The default OD membrane properties were a hydrophobic layer thickness of 0.1 μm, porosity of 0.8, thermal conductivity of 0.05 W m^{-1}K^{-1}, and pore diameter of 50 nm. The same support layer thickness was assumed for both FO and OD to ensure a reasonable comparison. The unit of OD water permeability was

converted to the same unit as the FO water permeability (x-axis) in order to compare the two processes on an identical scale. FO membrane support layer properties corresponded to those of a commercial thin-film composite membrane (S = 453 µm).[139] The FO water permeability coefficient, A, was varied over a wide range of values. The salt permeability coefficient depended on the water pemeability and was determined using the permeability-selectivity trade-off for polyamide membranes established in the literature, $B = \gamma A^3$ (Supplementary Note). The OD permeability was varied by changing the thickness of the membrane hydrophobic layer, with the maximum OD flux (25.3 kg m^{-2}h^{-1}) occurring when the membrane reached the minimum possible thickness defined by the wetting criteria (Equation 22). Polyamide thin-film composite FO membranes were simulated so the water permeability and salt permeability were linked using an established trade-off in the literature. Thus, the maximum water flux for FO membranes (18.6 kg m^{-2}h^{-1}) is reached when the salt flux across the membrane is high enough that further increases will negatively impact the water flux. This limitation occurs at a water permeability coefficient of 6.5 kg m^{-2}h^{-1}bar^{-1}. At all permeability values, OD membranes offered the advantage of improved salt rejection. This was especially true at higher water permeabilities where the FO salt rejection rapidly deteriorated. When the FO membranes reached their maximum flux, the salt rejection was 80%, far lower than typical values for membranes in seawater desalination, which usually exceed 99% rejection.[140] The high salt rejection in OD also explains the higher water flux achievable with OD membranes as compared to FO membranes—OD experiences less reverse salt flux and concentration polarization than FO and thus has a higher available concentration difference to drive permeation.
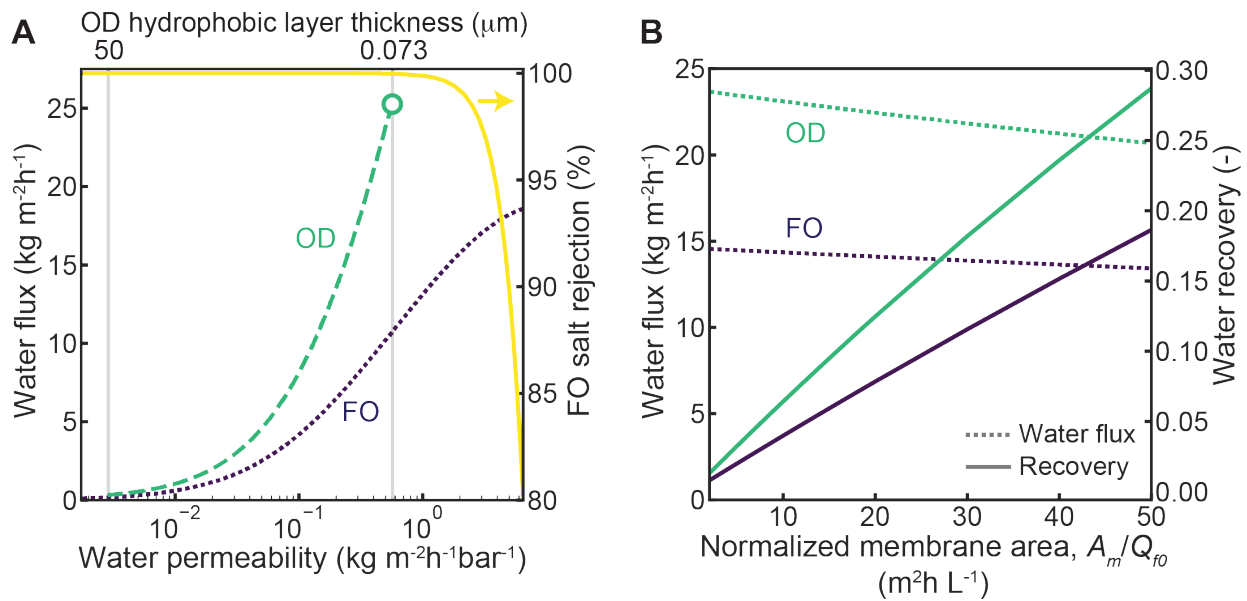
Figure 3.6 (A) Water flux that can be achieved using hydrophobic osmotic distillation (OD) membranes and polyamide thin-film composite forward osmosis (FO) membranes with a given water permeability coefficient. The OD hydrophobic layer thickness that corresponds to a given water permeability coefficient is indicated. FO membranes are simulated with selectivity following the permeability-selectivity trade-off for polyamide membranes, and the corresponding salt rejection is shown. (B) Achievable water flux and recovery in OD and FO modules as a function of normalized membrane area.

Module-scale analysis was used to further compare OD and FO performances in Figure 3.6B. For this analysis, the FO membrane had the simulated properties of a commercial thin-film composite membrane previously studied in the literature ($A = 1.48$ kg m^{-2}h^{-1}bar^{-1}, $B = 0.043$ kg m^{-2}h^{-1}, $S = 453$ μm).[139] The OD membrane was modeled with identical support layer properties as the FO membrane, but the OD permeability was set using a 0.1 μm thick hydrophobic layer. Results from the module-scale analysis indicated that OD membranes always demonstrated both higher average water flux and water recovery. For a normalized membrane area of 50 m^{2}h L^{-1}, the OD water recovery was 56% higher than FO. For the entire range of membrane areas investigated, the average water flux across the OD module was around 8.5 kg m^{-2}h^{-1} (59%) higher than that of FO.

3.4 Conclusions

In this study, we investigated the optimal membrane properties and the impact of heat transfer on the osmotic distillation (OD) process through element-scale and module-scale simulations. A principal conclusion of the analyses at both scales is that decreasing the thickness of the hydrophobic layer is critical for high performance in OD since it both increases the membrane permeability and reduces detrimental heat transfer effects. While there is a limit to how thin membranes can be designed based on thermodynamic wetting criteria, membranes with pore sizes consistent with current commercial membranes can reach desirable thicknesses ($\sim$ 0.1 µm) without risking wetting. At such low thicknesses, the negative impact of temperature polarization on membrane water flux is minimal. Module-scale analysis showed that detrimental heat accumulation in the feed and draw channels can also be minimized at membrane thicknesses lower than 1 µm. Investigations into the impact of membrane pore size, porosity, and thermal conductivity on performance indicated that these parameters have a smaller impact than thickness when varied within a realistic range. Therefore, factors such as pore size should be modified as needed to fabricate membranes with smaller thicknesses.

Our results suggest that optimized OD membranes offer a highly selective alternative to conventional dense polymeric forward osmosis (FO) membranes. OD membranes with optimized properties can offer water fluxes 36% higher than those of optimized polyamide FO membranes. Furthermore, in large-scale systems, the water recovery of practically feasible OD membranes is 56% higher than current FO membranes. Unlike dense polymeric FO membranes, OD membranes offer complete rejection of all non-volatile solutes. Thus, the utilization of OD can eliminate challenges associated with reverse salt leakage in FO processes that add the requirement of

complicated draw solute recovery systems. OD can be especially advantageous for applications requiring high removal of small neutral molecules, such as N-nitrosodimethylamine (NDMA), boron, and urea, that easily pass through polyamide FO membranes.

To realize the advantages of OD systems, further studies must push forward the development of thin and robust hydrophobic membranes. As membrane hydrophobic layers approach very low thicknesses, they will require porous hydrophilic support layers to provide mechanical strength and to prevent breakage. Similar to FO, these support layers must be tailored to reduce concentration polarization effects. Finally, the successful implementation of OD will require further investigation into draw solutions with low volatility that can take advantage of the selective characteristics of the OD membranes, and studies must be undertaken to better understand practical fouling and wetting behavior. Combined developments in OD membrane fabrication and process design will enable desalination with both high productivity and selectivity to be realized.

CHAPTER 4

Analysis of volatile and semi-volatile organic compound transport in membrane distillation modules

4.1 Introduction

Membrane distillation (MD) is a thermally driven separation process experiencing growing interest, especially in treatment of high salinity brines from oil and gas operations, industrial wastewater, and food concentrate.[9] Since MD can be operated with relatively low temperatures (30–80 ℃) compared to conventional thermal distillation,[141] it can potentially utilize low-grade heat to decrease energy costs. Furthermore, compared to membrane-based reverse osmosis (RO) desalination processes, MD does not require high operating pressures and can treat higher salinity brines.[142] These strengths may allow MD to treat certain waters at lower cost than conventional technologies.

A widely acknowledged benefit of MD is that it ideally offers complete rejection of macro-molecules, colloids, ions, and other non-volatile constituents.[142] The high rejection in MD is an inherent characteristic of the process since it only allows for gas-phase transport of constituents across a hydrophobic membrane from the feed side to the permeate side.[143] The vapor pressure difference between the feed and permeate sides drives water vapor to move across the membrane while non-volatile compounds remain on the feed side. The ability to remove all non-volatile solutes gives MD a distinct advantage over RO which poorly rejects non-polar and low molecular weight (MW) compounds.[144,145]

Although MD can highly reject non-volatile constituents, the process has shown poor rejection of semi-volatile and volatile compounds. Specifically, the process has shown less than 80% rejection of semi-volatile compounds (Henry's constant between 10^{-4} and 3×10^3 Pa·L mol^{-1}) and the rejection of volatile compounds (Henry's constant greater than 3×10^3 Pa·L mol^{-1}) falls between negative values and 54%.[146] The rejection of volatile compounds in MD is strongly dictated by the Henry's constant,[146,147] and hence, volatile organic compounds (VOCs) can be problematic in MD water treatment systems since they have high Henry's constants, are commonly encountered in feed waters, and can cause negative environmental impacts and human health issues.[148] Poor rejection of VOCs in MD makes it difficult to meet treatment requirements and limits the application of MD for water treatment.

Despite growing interest in utilizing MD for a wide range of feed streams that contain volatile compounds, few studies have focused on the transport of VOCs. Those studies that have been conducted experimentally investigated the separation of volatile contaminants found in wastewaters and validated theoretical models for predicting the concentrations of volatile contaminants accumulated in the permeate streams.[146,147,149] Recent works have emphasized the importance of the Henry's constant in determining MD selectivity.[146,150] However, prior studies have examined a limited range of compound volatilities and a small set of volatile contaminants (less than 16 compounds).[146,149] There is a need to expand this work to encompass a wider set of contaminants and better correlate molecular properties to MD selectivity. Furthermore, the impacts of operating conditions, such as temperature and crossflow velocity, in large-scale membrane modules have not been investigated despite evidence that these conditions may impact contaminant transport.[151] Thus, to understand realistic removal rates of volatile components, there

is an urgent need to study a wider range of compounds, understand the impact of compound properties on rejection rates, and conduct studies relevant to large-scale membrane modules.

In this work, we investigate the removal of a range of semi-volatile and volatile compounds in direct contact membrane distillation (DCMD) with 55 compounds total enabling a comprehensive understanding of the compound properties, system designs, and operating conditions that impact mass transport in DCMD. First, we examine the influence of molecular properties including the diffusion coefficient and Henry's constant on solute transport. We then study the transport resistances across MD membranes, identifying distinct transport regimes dominated by resistances in the membrane or external boundary layers. Large-scale DCMD modules are simulated to determine the realistic contaminant removal in DCMD systems by varying conditions including operating temperatures and crossflow velocity. Module-scale simulations give the first insights into key operating conditions that will impact contaminant removal. Finally, we provide guidelines for the mass transport of volatile compounds in MD systems and compare MD transport to conventional RO systems.

4.2 Theoretical framework for volatile compound transport

4.2.1 Overview of the dataset used in modeling

This study collected semi-volatile and volatile compounds from multiple sources.[146,147,149] The dataset included 55 compounds and 12 features for each compound including the name, activity coefficient, three Antoine constants, two diffusion coefficient constants, molar volume, octanol-water partitioning coefficient, dipole moment, and organic compound class. The full compound list with properties is presented in Table 1 and additional properties are tabulated in the Supporting Information. The activity coefficient was used for obtaining the Henry's constant as described in

the Yaws Handbook of Properties for Aqueous Systems.[152] Antoine constants (A, B, and C) needed

to simulate the vapor pressure of a pure component as a function of temperature were retrieved

from the Yaws Handbook of Vapor Pressure.[153] The two diffusion coefficient constants were

retrieved from the Yaws Handbook of Diffusion Coefficients at Infinite Dilution in Water,[154] and

they were used to obtain the diffusion coefficient of each volatile compound as a function of

temperature. The molar volume, octanol-water partitioning coefficient, and dipole moment of each

compound were acquired using ChemSpider. The molecular properties were used to calculate the

Henry's constant and mass transfer coefficient at the interface with different temperatures.

Table 4.1 List of organic compounds investigated in this work with their key molecular properties ordered by Henry's constant. The entire list of chemicals and properties can be found in the Supporting Information.

Name	Class	Henry's constant at 25°C (Pa·L mol^{-1})	Molecular weight (g mol^{-1})	Log octanol-water partitioning coefficient	Dipole moment (debye)
bisphenol A	phenols	9.28×10^{-4}	228.29	3.64	1.695
phenylmethanol (benzyl alcohol)	alcohols	1.87×10^{1}	108.14	1.08	1.442
phenol	phenols	5.68×10^{1}	94.11	1.51	2.087
2-methylphenol (o-cresol)	phenols	6.27×10^{1}	108.14	1.94	2.069
3-methylphenol (m-cresol)	phenols	6.27×10^{1}	108.14	1.94	2.212
4-methylphenol (p-cresol)	phenols	6.27×10^{1}	108.14	1.94	2.385
aniline	amines	1.93×10^{2}	93.13	1.08	0.626
4-tert-butylphenol	phenols	2.09×10^{2}	150.22	3.42	2.431
benzophenone	ketones	2.13×10^{2}	182.22	3.15	2.381
ethanol	alcohols	5.75×10^{2}	46.07	-0.14	1.545
propanol	alcohols	7.62×10^{2}	60.10	0.35	1.557
butanol	alcohols	8.93×10^{2}	74.12	0.84	1.550
cyclohexanone	ketones	9.12×10^{2}	98.15	1.13	2.605
pyridine	amines	1.11×10^{3}	79.10	0.8	1.353
pentanol	alcohols	1.35×10^{3}	88.15	1.33	1.557
1-hexanol	alcohols	1.97×10^{3}	102.18	1.82	1.550
benzal dehyde	aldehydes	2.85×10^{3}	106.12	1.71	2.402
4-tert-octylphenol (p-tert-octylphenol)	phenols	2.96×10^{3}	206.33	5.28	1.811
acetonitrile	nitrile	3.10×10^{3}	41.053	-0.15	2.187
α-epichlorohydrin	ethers	4.36×10^{3}	92.53	0.63	2.273
acetone	ketones	5.03×10^{3}	58.08	-0.24	2.571

methyl ethyl ketone	ketones	6.67×10^3	72.11	0.26	2.567
methyl propyl ketone	ketones	8.02×10^3	86.13	0.75	2.543
diethyl ketone	ketones	8.85×10^3	86.13	0.75	2.565
methyl butyl ketone (2-hexanone)	ketones	9.44×10^3	100.16	1.24	2.547
acrylonitrile	nitrile	1.40×10^4	53.064	0.21	2.049
ethyl acetate	esters	1.60×10^4	88.11	0.86	1.880
3-methylbutanal	aldehydes	1.61×10^4	86.13	1.23	2.485
ethyl butyrate (ethyl butanoate)	esters	4.15×10^4	116.16	1.85	1.760
hexyl acetate	esters	5.37×10^4	144.21	2.83	1.860
methyl tert-butyl ether	ethers	5.95×10^4	88.15	1.43	1.676
ethyl hexanoate (ethyl caproate)	esters	6.37×10^4	144.21	2.83	0.385
dibromomethane	alkyl halides	9.91×10^4	173.84	1.52	1.153
vinyl acetate	esters	1.19×10^5	86.09	0.73	1.610
1,2-dichloroethane	alkyl halides	1.20×10^5	98.96	1.83	1.800
styrene	arenes	2.85×10^5	104.15	2.89	0.031
bromochloromethane	alkyl halides	3.03×10^5	129.38	1.43	1.300
dichloromethane	alkyl halides	3.29×10^5	84.93	1.34	1.400
chlorobenzene	arenes	4.04×10^5	112.56	2.64	1.170
chloroform	alkyl halides	4.11×10^5	119.37	1.97	1.122
cis-1,2-Dichloroethylene	alkenes	4.13×10^5	96.94	1.98	1.878
trans-1,2-Dichloroethylene	alkenes	4.13×10^5	96.94	1.98	0
xylenes (total)	arenes	5.26×10^5	106.17	3.09	0.159
benzene	arenes	5.42×10^5	78.11	1.99	0
toluene	arenes	6.73×10^5	92.14	2.54	0.113
1,4 xylene (p-xylene)	arenes	6.99×10^5	106.17	3.09	0.008
bromomethane (methyl bromide)	alkyl halides	8.60×10^5	50.50	1.18	1.065
ethylbenzene	arenes	9.00×10^5	106.17	3.03	0.120
trichloroethylene	alkenes	9.98×10^5	131.38	2.47	0.651
chloroethane (ethyl chloride)	alkyl halides	1.10×10^6	64.51	1.58	1.310
tetrachloroethylene	alkenes	1.79×10^6	165.82	2.97	0
trans-1,3-dichloropropene	alkenes	2.48×10^6	110.97	2.29	1.406
1,1-dichloroethylene	alkenes	3.23×10^6	96.94	2.12	0.705
limonene	arenes	5.75×10^6	136.24	4.83	0.163
butane	alkanes	9.82×10^7	58.12	2.31	0

4.2.2 Determination of the Henry's law constant

The Henry's law constant (air-water partitioning coefficient) is an important parameter to predict the volatility of a chemical compound and its rejection in MD.[155] Previous studies have reported a close relation between the Henry's constant and rejection for volatile and semi-volatile compounds.[146,149,156,157] The Henry's constant is calculated by using the following equation:

$$H_s = \gamma_s P_{v,s}^* \bar{V}_w \qquad (24)$$

where γ_s is the activity coefficient, $P_{v,s}^*$ is the pure component vapor pressure, and $\bar{V}_w$ is the molar volume of water. This work simulated low concentrations (less than 1 mM) of volatile compounds so the effect of solute concentration on the activity coefficient was assumed to be negligible unless otherwise noted. The pure component vapor pressure of each compound was obtained using the Antoine equation:

$$P_{v,s}^* = 10^{A - \frac{B}{C+T}} \qquad (25)$$

where A, B, and C are Antoine constants that are specific to each compound, and T is temperature. With the equations above, the Henry's constant of each compound was obtained at different temperatures, and it was applied to gain the corresponding partial vapor pressure, feed concentration, or permeate concentration assuming compound concentrations at the air-liquid interfaces were at equilibrium.

4.2.3 Mass transfer of volatile compounds

Transport of semi-volatile and volatile compounds is driven by partial pressure differences affected by the compound concentrations and temperatures at the interfaces of the membrane. The solute flux, J_s, of semi-volatile and volatile compounds across membranes is described by the following equations representing the three stages of transport: transport from the feed bulk solution

70

to the feed-membrane interface (eq 26), transport of vapor through the membrane (eq 27), and transport from the permeate-membrane interface to the permeate bulk solution (eq 28).

$$J_s = k_{l,s,f}\left(C_{s,f} - C_{s,f,m}\right) \tag{26}$$

$$J_s = \frac{k_{s,m}}{RT_m}\left(P_{v,s,f,m} - P_{v,s,p,m}\right) \tag{27}$$

$$J_s = k_{l,s,p}\left(C_{s,p,m} - C_{s,p}\right) \tag{28}$$

In the above equations, $k_{l,s,f}$ and $k_{l,s,p}$ are the liquid mass transfer coefficients of a solute in the feed and permeate, respectively; $C_{s,f}$ and $C_{s,p}$ are the feed and permeate bulk concentrations of a compound, respectively; $C_{s,f,m}$ and $C_{s,p,m}$ are the compound concentrations of the feed and permeate air-liquid interfaces at the membrane surface; $P_{v,s,f,m}$ and $P_{v,s,p,m}$ are the partial vapor pressures of a compound at the feed and permeate interfaces, respectively; R is the ideal gas constant; T_m is the average of the temperatures at the feed and permeate interfaces; and $k_{s,m}$ is the mass transport coefficient across a membrane that can be calculated using the equations below.

$$k_{s,m} = \frac{\varepsilon}{\tau d}\left(\frac{1}{D_{s,a}} + \frac{1}{D_{s,m}}\right)^{-1} \tag{29}$$

$$D_{s,a} = \frac{0.00143 T_m^{1.75}}{p_t(\bar{V}_s^{\frac{1}{3}} + \bar{V}_a^{\frac{1}{3}})^2 \left(2\left(\frac{1}{M_s} + \frac{1}{M_a}\right)^{-1}\right)^{\frac{1}{2}}} \tag{30}$$

$$D_{s,m} = \frac{d_p}{3}\sqrt{\frac{8RT_m}{\pi M_s}} \tag{31}$$

The membrane mass transfer coefficient, $k_{s,m}$, is obtained using the molecular diffusion coefficient, $D_{s,a}$, and the Knudsen diffusion coefficient, $D_{s,m}$. The parameter ε is the porosity of

the membrane, τ is the tortuosity of the membrane, and d is the membrane thickness. The molecular diffusion coefficient of a compound through the air in the membrane pore, $D_{s,a}$, is estimated by the empirical correlation as shown in Equation 30,[8] where M_s and M_a are the molecular weights of the solute and air, respectively; $\overline{V_s}$ and $\overline{V_a}$ are the molar volume of the solute and air, respectively; and P_T is the total pressure in a pore. The Knudsen diffusion coefficient, $D_{s,m}$, is calculated using Equation 31, where d_p is the average pore diameter.

The liquid mass transfer coefficient, $k_{l,s}$, indicates the transport resistance of the boundary layers on the feed and permeate-membrane interfaces. Empirical equations were used for calculating Sherwood number of the laminar and turbulent flow channels in a membrane module.[158,159] The expressions for the mass transfer coefficient and Sherwood numbers are shown below:

$$k_{l,s} = Sh \frac{D_{s,w}^l}{d_h} \tag{32}$$

$$Sh = 1.85 \left(Re \frac{d_h}{l_s} Sc\right)^{0.33} \text{ (Re < 2300, laminar flow)} \tag{33}$$

$$Sh = 0.04 Re^{0.75} Sc^{0.33} \text{ (4000 < Re, turbulent flow)} \tag{34}$$

where $D_{s,w}^l$ is the liquid diffusion coefficient of a compound in water, d_h is the hydraulic diameter of the channel, Sh is the Sherwood number, Re is the Reynolds number, Sc is the Schmidt number, and l_s is the length of the channel. This study uses the module channel dimension of 5 cm × 5 cm × 0.2 cm for element-scale analysis, which is a typical lab-scale module channel. For module-scale analysis, a spacer-filled plate membrane module (100 cm × 100 cm × 0.4 cm)

is used and the Sherwood number for the spacer-filled channel in laminar flow is obtained as shown below:

$$Sh = 0.664 Re^{0.5} Sc^{0.33} \left(\frac{d_h}{l_s}\right)^{0.5} \tag{35}$$

(Re < 2300, laminar flow in spacer-filled channel)

Henry's constants obtained at the feed- and permeate-membrane interfaces, $H_{s,f}$ and $H_{s,p}$, and the mass transfer coefficients were used to calculate the overall mass transfer coefficient of a volatile compound, $k_{s,tot}$. Then, the overall mass transfer coefficient, Henry's constant, and bulk compound concentrations were used to describe the flux of the volatile compound, J_s.

$$k_{s,tot} = \left(\frac{H_{s,f}}{k_{l,s,f}} + \frac{RT_m}{k_{s,m}} + \frac{H_{s,p}}{k_{l,s,p}}\right)^{-1} \tag{36}$$

$$J_s = k_{s,tot}\left(C_{s,f}H_{s,f} - C_{s,p}H_{s,p}\right) \tag{37}$$

The heat of transport by the volatile compound flux was neglected because the volatile compound concentration was small compared to the amount of water in the feed and permeate streams (i.e., the molar percentage of solute to water was less than 1%). We also assumed there is no leakage of volatile compounds from system due to their high volatility and no hydrophobic interaction between volatile compounds and membrane materials or tubing, as has been assumed in prior work.[160–162]

4.2.4 Numerical analysis of DCMD membrane module

Large-scale membrane module analysis was used to understand effects related to temperature or concentration changes along the feed and permeate streams that cannot be evaluated using

element-scale analysis. Simulations were conducted in a counter-current membrane module based on previous work showing that this is the most efficient configuration.[121,122]

The differential equations were used to describe mass and heat transfer in the system and were discretized using the finite difference method. Three differential equations were used to determine the flow rates, temperature, and volatile compound concentrations along the module:

$$\frac{dQ_f(x)}{dA} = \frac{dQ_p(x)}{dA} = J_w(T_{f_m}(x), T_{p_m}(x), C_{f_m}(x), C_{p_m}(x)) \tag{38}$$

$$\frac{d[Q_f(x)h_L(T_f(x))]}{dA} = \frac{d[Q_p(x)h_L(T_p(x))]}{dA} \tag{39}$$

$$= q(T_{f_m}(x), T_{p_m}(x), C_{f_m}(x), C_{p_m}(x))$$

$$\frac{d[Q_f(x)C_f(x)]}{dA} = \frac{d[Q_p(x)C_p(x)]}{dA} = J_s(T_{f_m}(x), T_{p_m}(x), C_{f_m}(x), C_{p_m}(x)) \tag{40}$$

where Equation 38 presents the volumetric balance of water, Equation 39 expresses the heat balance of convective and conductive fluxes, and Equation 40 accounts for the mass balance of the solute. x represents an axial position along the membrane module; dA is equal to the total membrane area, A_m, divided by the number of the elements used in numerical analysis; J_w is the water flux; Q_f and Q_p are feed and permeate flow rates in membrane module; T_f and T_p are feed and permeate solution temperatures; h_L is heat transfer coefficient of liquid; C_f and C_p are feed and permeate concentrations of a volatile compound; and T_{f_m}, T_{p_m}, C_{f_m}, and C_{p_m} express temperatures and concentrations at membrane surface. The modified Powell method was used to solve the equations in conjunction with the element-scale analysis. The boundary conditions were $Q_f(0) = Q_{f,0}$, $Q_p(N) = Q_{p,0}$, $T_f(0) = T_{f,0}$, $T_p(N) = T_{p,0}$, $C_f(0) = C_{f,0}$, and $C_p(N) = C_{p,0}$, where 0 and N stand for the position of the inlet and outlet, respectively. The calculated water and

heat fluxes over the entire module were used to obtain bulk temperatures and concentrations with varying volatile compounds and operation conditions.

4.2.5 Equilibrium ratio across the MD membrane

The removal of solutes in module-scale analysis was assessed using the equilibrium ratio, a parameter that describes the ratio of the permeate concentration to the feed concentration at pseudo steady state. The equilibrium ratio is expressed below:

$$Eq = \frac{C_{s,p}}{C_{s,f}} \tag{41}$$

where Eq is equilibrium ratio of a solute, $C_{s,p}$ is the solute concentration in the permeate side, and $C_{s,f}$ is the solute concentration in the feed side. An equilibrium ratio less than 1 indicates that the compound is rejected. An equilibrium ratio greater than 1 indicates that the higher amount of a volatile compound exists in the permeate stream at equilibrium.

4.3 Results and Discussion

4.3.1 Molecular properties for predicting volatile and semi-volatile compound transport

The transport of volatile compounds from the bulk feed solution to the bulk permeate solution requires compounds to diffuse through the stagnant film layer on the feed side of the membrane, evaporate at the gas-liquid interface, diffuse through the membrane in the gas phase, condense on the permeate gas-liquid interface, and diffuse through the stagnant film layer on the feed side of the membrane (Figure 4.1). The resistances associated with transport across the membrane are described in Equations 29–36. These equations relay the complex dependence of solute transport on the properties of the compound and membrane system.
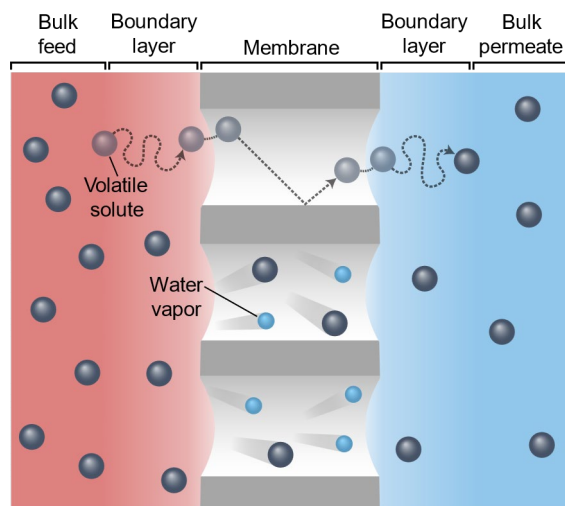
Figure 4.1 Conceptual diagram of water and volatile solute transport in membrane distillation. Transport of a volatile solute from the bulk feed solution to the bulk permeate solution requires diffusion through the boundary layer on the feed side of the membrane, evaporation, vapor-phase diffusion through the membrane pore, condensation, and diffusion through the boundary layer on the permeate side of the membrane.

Relating the molecular properties of volatile and semi-volatile compounds to transport properties is key to gaining generalizable insights on volatile mass transport in MD. Prior studies have shown that size, hydrophobicity, polarity, and volatility of a compound play important roles in explaining rejection. In this work, all 55 compounds in the dataset were grouped into different organic compound classes (12 total) and ordered according to the average Henry's constant of the compounds in each class (Figure 4.2A, Table 4.1). Alkanes, arenes, alkenes, alkyl halides, ethers, and esters are relatively volatile and thus have higher Henry's constants compared to the other compounds studied. Amines, alcohols, aldehydes, ketones, nitriles, and phenols are less volatile.

The compounds in the dataset spanned a wide range of molecular properties. Figure 4.2B shows the dipole moment and log of the octanol-water partitioning coefficient (log P) of each compound. The compound classes with higher Henry's constants (alkanes, arenes, alkenes, alkyl halides, ethers, and esters) had relatively low dipole moments values compared to the less volatile

compound classes (amines, alcohols, aldehydes, ketones, nitriles, and phenols). More hydrophobic compounds (i.e., those with a high octanol-water partitioning coefficient) tended to have a lower dipole moment and higher Henry's constant. As was expected, compounds that have a low dipole moment and high octanol-water partitioning coefficient tend to be highly volatile since they have weaker interactions with liquid water. Although nonpolar compounds can develop induced dipole forces due to water molecules (making nonpolar compounds temporarily polar), the forces are weaker than the dipole forces of polar compounds. Thus, they tend to have higher Henry's constants.

Specific compound classes have distinct characteristics that impact their volatility. Since alkanes, arenes, and alkenes have a very low dipole moment due to their symmetrical structures, they are nonpolar, have a low affinity for water molecules, and easily volatilize.[163] For instance, butane is the compound in the alkane class with the highest Henry's constant in the dataset because its symmetric structure makes it nonpolar, and it has a shorter chain length than similar compounds in its class. Alkyl halides, ethers, and esters have slightly higher dipole moments than the alkanes, arenes, and alkenes. Carbon and halogen in alkyl halides contribute to an electronegativity difference in molecules that increases the dipole moment. The carbon-oxygen bond in ethers and esters also has an electronegativity difference that makes molecules polar. Nitriles, ketones, and aldehydes have high dipole moments due to their double and triple bonds. Amines can form hydrogen bonds with themselves or water[164] so that their increasing MW and chain length decrease volatility because more hydrogen bonds are formed. Hydroxyl groups in phenols and alcohols make the classes polar and less volatile. Bisphenol A has the lowest Henry's constant in the dataset due to its two hydroxyl groups and high MW.
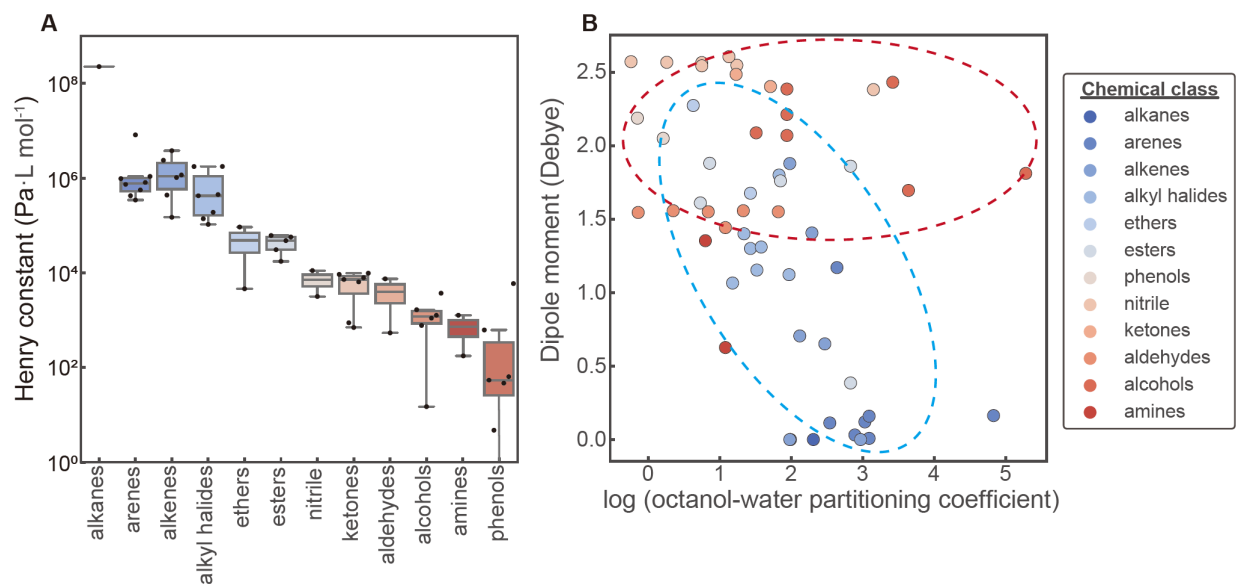
Figure 4.2 (A) Distribution of Henry's constants for each organic compound class studied in this work where compounds colored blue are more volatile and compounds colored red are less volatile. (B) Log octanol-water partitioning coefficient (log P) and dipole moment for each compound. The colors correspond the classes of the compounds.

The solute flux of compounds in DCMD was simulated using a previously established modeling framework (eq 37). The accuracy of the framework was verified by comparing simulated rejection values to those available from prior work in the literature[147]. Overall, it was found that simulated rejection values were within 12% of measured values for the four compounds examined: 4-tert-octylphenol, 4-tert-butylphenol, and bisphenol A (Figure C-S2).

The influence of compound properties on solute flux was investigated using all 55 compounds in the dataset. The solute flux equation (eq 37) indicates that flux is determined by the overall mass transfer coefficient and the partial vapor pressure difference between the feed and permeate sides. The overall mass transfer coefficient is a function of the Henry's constant, liquid mass transfer coefficient, and membrane properties (eq 36). The partial vapor pressure difference is influenced by the Henry's constant and concentration. The solute flux equation and prior work

reveal the strong influence of the Henry's constant on solute transport;[146,147] this influence is also apparent in our simulations (Figure 4.3A), where compounds with a higher Henry's constant showed increased solute flux. Importantly, only compounds with a Henry's constant below 10000 Pa·L mol^{-1} (red group) showed solute fluxes that strongly correlated with the Henry's constant (determination coefficient of 0.87, gray solid line). As the Henry's constant increased beyond 10000 Pa·L mol^{-1} (blue group), the solute flux as a function of Henry's constant asymptotically approached an upper limit rather than continuing to increase as the Henry's constant increased. The observation that highly volatile compounds did not show a strong correlation between solute flux and the Henry's constant indicates other factors likely influence solute transport.

After examining multiple properties that can be correlated to solute flux for compounds with a Henry's constant above 10000 Pa·L mol^{-1}, the diffusion coefficient was found to be the property that most substantially correlated with the solute flux (Figure 4.3B). Since compounds with very high Henry's constants can quickly transport through the membrane, their mass transport rates are dependent on the rate at which contaminants diffuse through boundary layers on either side of the membrane. The diffusion coefficient of the solute is the primary compound property that influences transport rates through such boundary layers, and a strong correlation was observed between solute flux and the diffusion coefficient for high volatility compounds (determination coefficient of 0.74, gray solid line). Since the diffusion coefficient is primarily related to the size of a molecule, it is apparent that highly volatile bulky compounds will transport in MD more slowly than smaller volatile molecules.
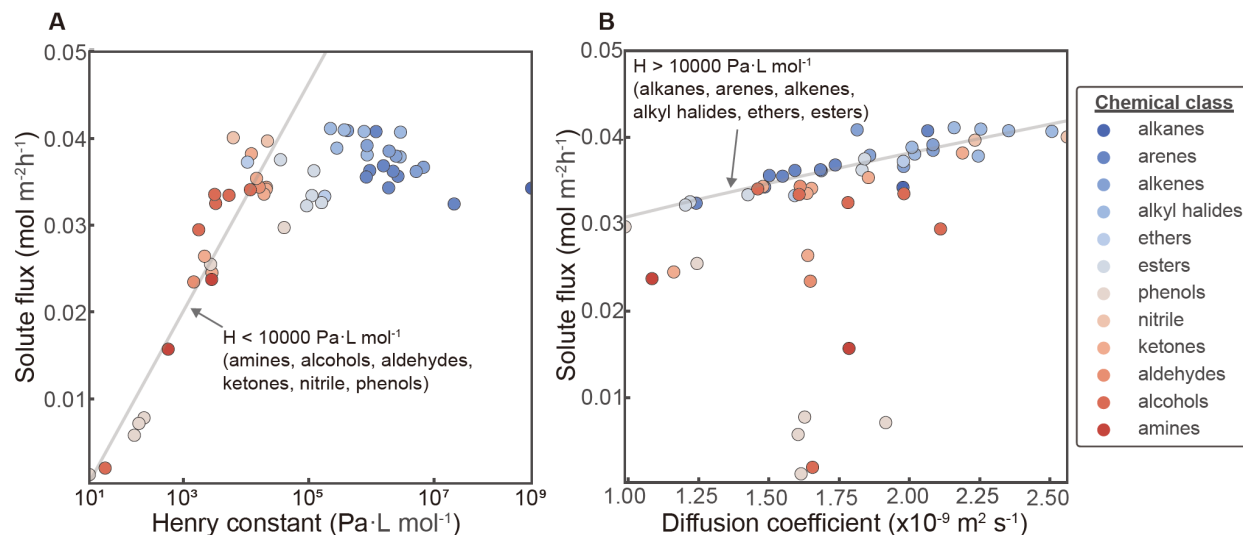
Figure 4.3 (A) Solute flux as a function of the Henry's constants. Gray line indicates a linear fit (R^2 = 0.87) to the data for low Henry's constant (less than 10000 Pa·L mol^{-1}) compounds. (B) Solute flux as a function of the diffusion coefficients. Gray line indicates a power function (R^2 = 0.74) for high Henry's constant (greater than 10000 Pa·L mol^{-1}) compounds. The MD membrane properties used in solute flux calculations were a thickness of 125 μm, porosity of 0.75, thermal conductivity of 0.06 W m^{-1}K^{-1}, and pore diameter of 220 nm. The feed concentration was 1 mM and the permeate side was DI water. The feed and permeate temperatures were 50 and 20 °C, respectively. The crossflow velocity was 0.31 m/s.

4.3.2 Transport resistance regimes of semi-volatile and volatile compounds

The results of the prior section indicate that, for semi-volatile and volatile compounds, there are distinct transport regimes in MD dictated by the dominant resistances to solute transport. Transport resistances can be broken down into two components: (1) the membrane resistance and (2) boundary layer resistances on the feed and permeate sides of the membrane (Figure 4.3A). Membrane resistances occur as solute molecules travel through the membrane pores via molecular diffusion and Knudsen diffusion; the membrane resistance is primarily affected by membrane properties and the physical size (molecular weight and volume) of a compound.[165] When the Henry's constant of a solute is low, membrane resistances dominate over other resistances and the system is in the membrane resistance regime. Boundary layer resistances occur due to hindered

solute transport from the feed and permeate bulk solutions to the air-liquid interfaces of the membrane; the boundary layer resistances are defined by film theory and primarily dictated by the diffusion coefficient of a solute and hydraulic conditions that affect the mass transfer coefficient (e.g. crossflow velocity and channel dimensions).[157] When the Henry's constant of a compound is high, the boundary layer resistances dominate. Thus, high volatility compounds operate in the boundary layer resistance regime.

In Figure 4.4B, the relative transport resistance associated with the membrane and boundary layers is shown for four compounds, which were chosen as representative compounds due to their varied Henry's constant values and other properties. The Henry's constant at 25 °C increased in order of phenol (39.9 Pa·L mol^{-1}), ethanol (638.4 Pa·L mol^{-1}), chloroform (3.87×10^5 Pa·L mol^{-1}), and butane (2.03×10^8 Pa·L mol^{-1}). The ratio of membrane resistance compared to total resistance rapidly dropped with increasing Henry's constant. Phenol's membrane resistance ratio was 96% and the ratio for butane plummeted to 4×10^{-6}%. For all compounds, the changes of the membrane resistances with increasing Henry's constant were insignificant compared to the changes of the boundary layer resistances. The membrane resistances for the four compounds fell in the range of $7.57\times10^4 - 9.77\times10^4$ J·s mol^{-1}m^{-1} with variations attributable to different molecular sizes of the compounds. In contrast, the feed boundary layer resistances increased substantially from 2.34×10^3 J·s mol^{-1}m^{-1} for phenol to 9.71×10^9 J·s mol^{-1}m^{-1} for butane because of the large difference in Henry's constants. High Henry's constants led to high boundary layer resistances because of the higher concentration polarization at the liquid-gas interface.[166]

This analysis indicates that the transport of the compounds with high Henry's constants will be dominated by the feed and permeate boundary resistances, whereas the transports of

compounds with low Henry's constants are limited by membrane resistances. In this work, we define the membrane resistance regime as the scenario where membrane resistance are at least a factor of ten higher than boundary layer resistances; compounds with Henry's constants less than $100 \, Pa \cdot L \, mol^{-1}$ can be considered in the membrane resistance regime for most realistic conditions. In contrast, the boundary layer resistance regime is defined such that boundary layer resistances are at least a factor of ten higher than membrane resistances; compounds with Henry's constants greater than $10000 \, Pa \cdot L \, mol^{-1}$ generally fall into this regime. Detailed explanation for determining each regime can be found in Supporting Information.
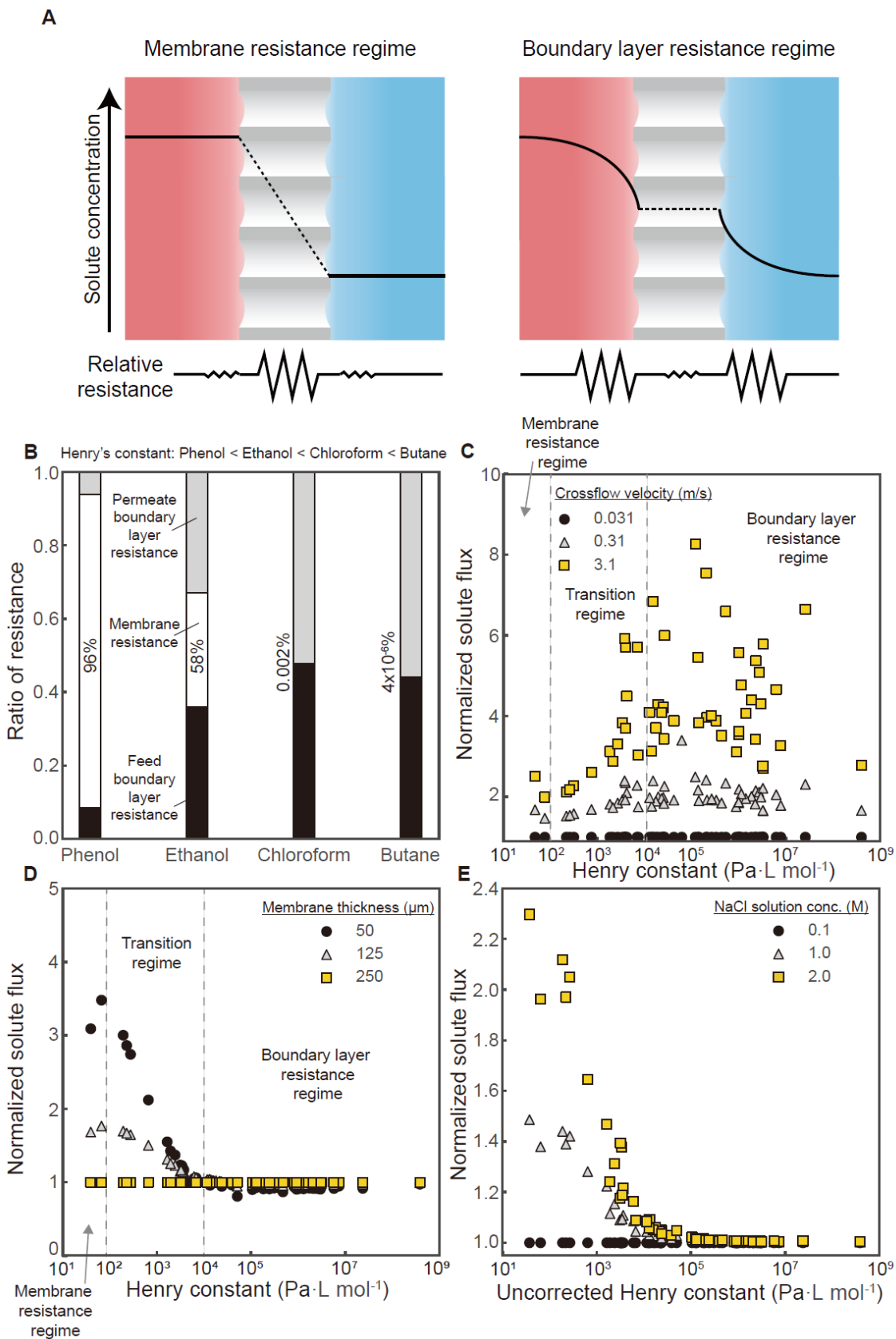
Figure 4.4 (A) Schematic diagram of the two resistance regimes (membrane resistance regime and boundary layer resistance regime). Concentration profiles for each regime are shown. (B) Transport resistances associated with boundary layers and the membrane with compounds having varied Henry's constants (Phenol: 39.9 Pa·L mol^{-1}, Ethanol: 638.4 Pa·L mol^{-1}, Chloroform: $3.87{\times}10^5$ Pa·L mol^{-1}, Butane: $2.03{\times}10^8$ Pa·L mol^{-1}). (C) Effect of the crossflow velocity on solute flux for compounds with different Henry's constants. (D) Effect of the membrane thickness on solute flux for compounds with different Henry's constants. (E) Effect of the NaCl solution concentration on solute flux for compounds with different Henry's constant. Note that the uncorrected Henry's constant means that the fixed Henry's constants were used for only for plotting. During the calculations, Henry's constants varied depending on concentration. The MD membrane properties were a thickness of 125 µm (unless otherwise indicated), porosity of 0.75, thermal conductivity of 0.06 W m^{-1}K^{-1}, and pore diameter of 220 nm. The feed concentration was 1 mM and the permeate side was DI water. The feed and permeate temperatures were 50 and 20 °C, respectively.

The distinct solute transport regimes in MD become apparent when varying conditions such as the crossflow velocity. Figure 4.4C shows the normalized solute flux of compounds with different Henry's constants in systems with different crossflow velocities. Increasing the crossflow velocity increases mass transfer in the boundary layers on either side of the membrane. For compounds in the boundary layer resistance regime (compounds with a Henry's constant greater than 10000 Pa·L mol^{-1}), the solute flux with the crossflow velocity of 3.1 m s^{-1} was about 4–8 times higher than that of the crossflow velocity of 0.031 m s^{-1}. Compounds with lower Henry's constants, which would be considered in the transition regime or membrane resistance regime, showed less of a change when the crossflow velocity decreased. We note the compounds in the membrane resistance regime (those with a Henry's constant below 100 Pa·L mol^{-1}) still show an increase in solute flux when the crossflow velocity increased. However, this change was triggered by increases in the heat transfer coefficient caused by the increased crossflow velocity rather than changes in mass transport resistance. Such changes in the heat transfer coefficient result in a higher temperature difference and thus greater solute flux.

Differences in behavior in the transport regimes are also evident when membrane properties are altered. Figure 4.4D shows the solute flux in membranes with different thicknesses. In the membrane resistance regime for low Henry's constant compounds, membranes with a thickness of 50 μm (low membrane resistance) showed 3-times higher normalized solute flux than membranes with a thickness of 250 μm (high membrane resistance). In the boundary layer resistance regime for high Henry's constant compounds, the thickness change did not result in substantial solute flux variations. It is noteworthy that the solute flux with a thin membrane slightly decreased in the boundary layer resistance regime; this was because the water flux increased and the temperature difference between the feed and permeate decreased. Therefore, there was less partial vapor pressure difference with a thin membrane that resulted in a lower solute flux.

The importance of different transport regimes is also evident when examining salting-out phenomena, where volatile solute transport increases when the salinity of a feed solution increases. This salting-out effect occurs because salinity increases the activity coefficient and resulting Henry's constant of a compound as described by the Setschenow equation (Supporting Information). The solute flux for all compounds with feed salinities of 0.1, 1, and 2 M NaCl is shown in Figure 4.4E where the x-axis shows the Henry's constant of compound that is not modified for salinity. In the membrane resistance regime and transition regime, increases in salt concentration increase the volatility of a compound, resulting in solute fluxes up to a factor of two higher than in pure species. For more volatile compounds in the boundary layer resistances regime, increases in volatility due to salinity increases have a negligible effect on the solute flux.

4.3.3 Large-scale analysis of volatile compound transport in DCMD system

An underexplored consideration for volatile compound selectivity in MD is the effect of large module-scale systems on the mass transport of a compound. To probe these effects, large-scale DCMD modules were simulated using the finite element method with the heat and mass transfer differential equations (eq 38–40). The system was designed to obtain the steady-state concentration of a volatile compound in the permeate stream while the permeate stream was recycled to provide cooling (Figure 4.5A). Treated water was constantly withdrawn from the permeate stream to maintain the same volume of circulating water. The feed stream was in a once-through configuration and the initial feed temperature and solute concentration were set at 50 °C and 1 mM, respectively. The steady-state concentration in the permeate stream was used to obtain the equilibrium ratio of a compound under the operating conditions. The equilibrium ratio describes the ratio of the permeate concentration to the feed concentration at steady state, which is an indicator of the solute removal in large-scale DCMD systems. An equilibrium ratio less than one indicates a solute is rejected whereas an equilibrium ratio greater than one indicates the solute is concentrated in the permeate stream.
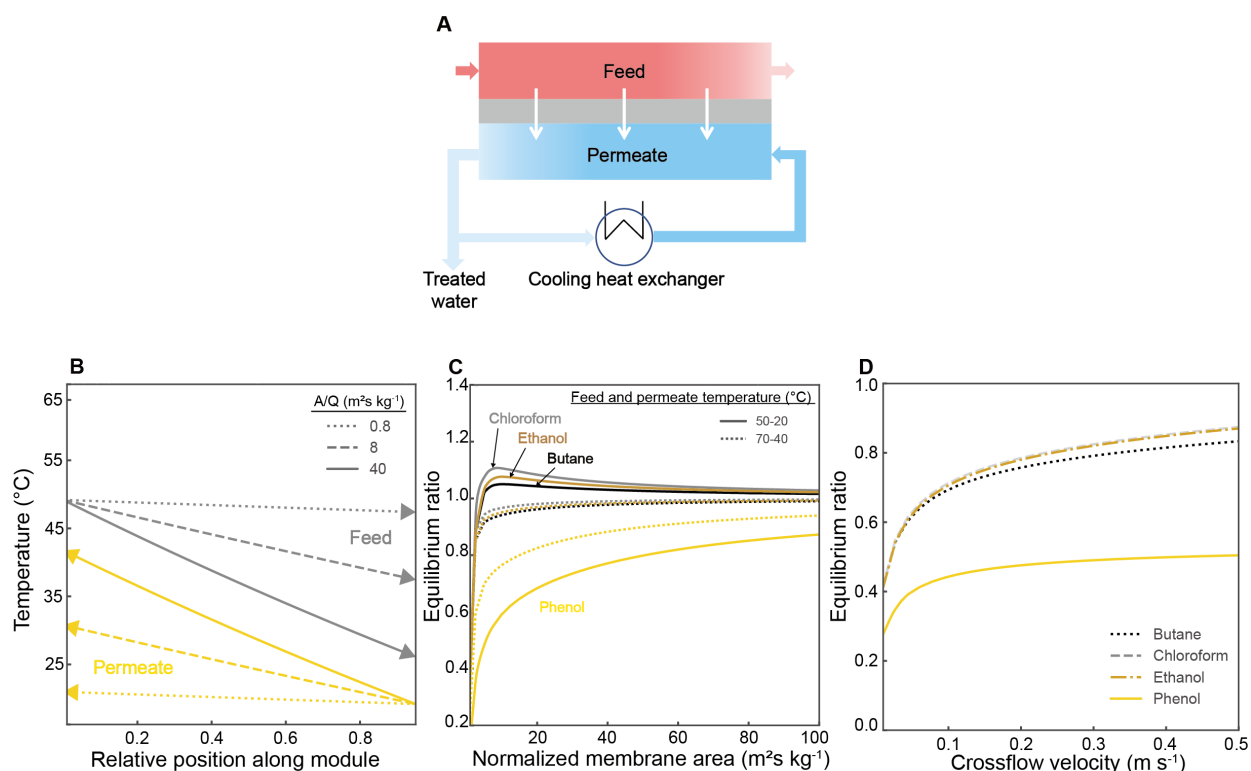
Figure 4.5 (A) Schematic diagram of a large-scale MD system with permeate recycling. The feed and permeate flow rates were 1.25 kg s^{-1}. The feed and permeate temperatures were 50 and 20 °C. The feed concentration at the inlet was 1 mM. The initial permeate concentration was zero, and the concentration accumulated as cycles continued. (B) Feed and permeate temperatures as a function of position in the membrane module for different normalized membrane areas (membrane area, A, divided by flow rate, Q). (C) The equilibrium ratio (i.e., ratio of the concentration in the permeate to the feed concentration) as a function of membrane area with different initial feed and permeate temperatures (50 and 20 °C, and 70 and 40 °C) for 1 mM feed solutions of butane, chloroform, ethanol, and phenol. (D) Effect of crossflow velocity on mass transport of compounds across an MD module with a normalized membrane area of 8 m^{2}s kg^{-1}. The MD membrane used in the simulations had a thickness of 125 μm and porosity of 0.75. Its thermal conductivity was 0.06 W m^{-1}K^{-1}, and pore diameter was 220 nm.

The feed and permeate temperatures along the length of a counter-current membrane module are shown in Figure 4.5B for different values of the membrane area normalized by the flow rate (A/Q). The feed temperature decreased and the permeate temperature increased along the length of the module as heat was transferred via conduction and the heat of vaporization. Larger membrane areas resulted in smaller temperature differences between the feed and the permeate sides because more heat crossed the membrane in a larger membrane area module. Normalized

87

membrane areas of 0.8 to 40 m^2s kg^{-1} were used for the simulations and their water recoveries increased from 6% to 21%. The corresponding average temperature difference in the module changed from 27 °C to 8 °C when the normalized membrane area increased from 0.8 to 40 m^2s kg^{-1}. As we show below, such changes in the temperature difference in the module have a substantial impact on the removal of volatile compounds because the Henry's constant of a compound is a function of temperature, and the varying Henry's constant changes the partial vapor difference between the feed and permeate sides and solute permeability.

Figure 4.5C shows the equilibrium ratios (the ratio of permeate concentration and feed concentration at steady state) of butane, chloroform, ethanol, and phenol at various normalized membrane areas and initial feed and permeate temperatures. The diffusion coefficients and Henry's constants of the compounds played important roles to determine the equilibrium ratios in the module. However, the order of the equilibrium ratios did not exactly align with the order of the Henry's constants or diffusion coefficients. Butane has the highest Henry's constant followed by chloroform, ethanol, and phenol. Ethanol has the highest diffusion coefficient followed by chloroform, butane, and phenol. However, the equilibrium ratio of chloroform was highest followed by ethanol, butane, and phenol. The non-intuitive order of equilibrium ratios occurs because solute flux is a function of both the Henry's constant and the diffusion coefficient. As membrane area increased, the equilibrium ratios of butane, ethanol, and chloroform approached 1 because the temperature difference between the feed and permeate becomes zero with increased heat transfer across a larger membrane area. In the case of phenol, the very low Henry's constant (five orders of magnitude smaller than butane) means a larger membrane area is required to approach an equilibrium ratio of 1.

When the initial feed temperature increased while maintaining the same initial temperature difference of 30 °C, it primarily affected the equilibrium ratios for modules with low and moderate membrane areas. When the initial feed and permeate temperatures were high, the accumulation of chloroform, ethanol, and butane on the permeate side lessened. Ethanol is in the transition regime, and chloroform and butane are in the boundary layer resistance regime. These compounds showed decreasing equilibrium ratios with increasing temperatures because the increases of Henry's constants resulted in higher boundary layer resistances, even though the partial vapor pressure difference increased at higher temperatures. Only phenol showed a reverse trend where the mass transport rate increased with higher initial temperatures. Phenol is in the membrane resistance regime, and its equilibrium ratio increased as raising the feed and permeate temperatures because membrane resistance becomes small with increasing temperature. The increase of partial vapor pressure difference with temperature outweighed the decrease of the overall mass transfer coefficient for phenol.

The effect of the crossflow velocity on the performance of membrane modules was also studied. Figure 4.5D shows that increasing crossflow velocity raised the equilibrium ratio of butane, chloroform, ethanol, and phenol in modules with a normalized membrane area of 8 m^2s kg^{-1}. High crossflow velocities increase the Reynolds and Sherwood numbers, which leads to a high mass transfer coefficient at the liquid-membrane interfaces. For example, an increase in the crossflow velocity from 0.01 m s^{-1} to 0.5 m s^{-1} resulted in a 2-times higher equilibrium ratio for chloroform and ethanol because of the higher mass transfer coefficients at the interfaces. Since chloroform's interface mass transfer coefficient was the most sensitive to the change of crossflow velocity, it showed the highest equilibrium ratio out of the four compounds.

4.3.4 Comparison of the transport mechanisms of the volatile compounds to RO

The above analysis reveals that MD has distinct selective properties compared to conventional desalination processes such as RO. Since MD is often considered as a technology that could replace RO, this section compares compound rejection between the two processes focusing on fundamental molecular properties that dictate transport. In MD, transport relies on the volatilization of compounds, vapor-phase diffusion through the membrane, and liquid-phase diffusion through boundary layers on either side of the membrane. Thus, the transport of compounds is primarily related to their Henry's constants and, in some cases, their diffusion coefficient. In RO, transport relies on partitioning of compounds into the membrane and diffusion through a dense polymer layer. Thus, transport across RO membranes is determined by a complex combination of solute size, charge, hydration properties, and other characteristics. These differences in selective properties can have a profound impact on the removal of certain classes of compounds in a given application. We note that, while MD compound transport can is well-described by theoretical models, the complicated interactions that dictate compound transport in RO mean that selectivity trends are typically determines experimentally. Therefore, our analysis relies on experimentally informed models for MD and direct experimental measurements for RO.

The rejection of various compounds in MD was compared to observations from the previous RO studies to provide general guidelines (Table 4.2). Sodium, potassium, calcium, chloride, phosphate, and sulphate ions are well-rejected by both RO and MD membranes due to their charge and low volatility. Low MW neutral non-volatile compounds such as urea, boron, *N*-nitrosomethylethylamine (NMEA), and *N*-nitrosodimethylamine (NDMA) are poorly rejected in RO due to their small size and neutral surface charge.[167–169] However, they can be highly rejected in MD due to their low volatility. Polar semi-volatile compounds including phenol and benzophenone are not completely rejected in MD systems or RO systems. Bisphenol A and benzyl

alcohol are non-polar semi-volatile compounds and show moderate rejection in MD. In RO systems, they showed varying rejection in different studies depending on membranes and operating conditions.[170–172] Non-polar volatile compounds include benzene and butane; these compounds have dipole moments equal to zero because of their symmetric structures. The non-polarity of the compounds results in high volatility and no electrostatic repulsion, and thus, both RO and MD have issues rejecting these compounds. Lastly, halogenated volatile compounds (1,2-dichloroethane and bromochloromethane) form shorter carbon-halogen bonds than carbon-oxygen or carbon-nitrogen. The compounds with these short bonds are likely to cross membranes without being rejected.[74] The relatively small size due to carbon-halogen bonds decreases MD rejection as well because Van der Waals forces are associated with the atomic size, and a decrease of the molecular size causes weak Van der Waals forces, which makes compounds more volatile.[173] Overall, MD outperforms RO when it comes to treating small and neutral compounds. For non-polar semi-volatile compounds, RO has higher rejection than MD. Halogenated volatile compounds are not effectively rejected neither RO nor MD since they are small and volatile.

Table 4.2 Qualitative comparison of RO and MD removal of different categories of compounds. 3-star indicates high rejection (> 80%) and 1-star indicates low rejection (< 40%). Neutral indicates no charge on the compound, semi-volatile corresponds to a Henry's constant less than 1000 Pa·L mol^{-1}, volatile corresponds to a Henry's constant greater than 1000 Pa·L mol^{-1}, polar corresponds to greater than 1.56 debye, and non-polar corresponds to less than 1.56 debye.

Compound category	RO	MD
Salts	★★★	★★★
Low-MW neutral compound (NDMA, NMEA, urea, boron)	★☆☆	★★★
Non-polar semi-volatile compound (bisphenol A, benzyl alcohol)	★★★	★★☆
Polar semi-volatile compound (phenol, benzophenone)	★★☆	★★☆
Non-polar volatile compound (benzene, butane)	★★☆	★☆☆
Halogenated volatile compound (1,2-dichloroethane, bromochloromethane)	★☆☆	★☆☆

Figure 4.6 visually summarizes the RO and MD rejection for different compounds as a function of molecular weight and the Henry's constant. The different colors indicate the rejections in MD and the different circle sizes indicate the rejections in RO. Compounds that have relatively low molecular weight and Henry's constant are better rejected in MD than RO (red color and small circle). Compounds that high Henry's constants are poorly rejected in MD (white color). They also have low molecular weights, which generally lead to poor rejection in RO as well. Although RO rejection is hard to correlate with certain compound properties, the graph shows that low molecular weight is generally unfavorable for RO rejection. For MD, rejection is relatively simple to explain because compound removal is closely related to the Henry's constant.
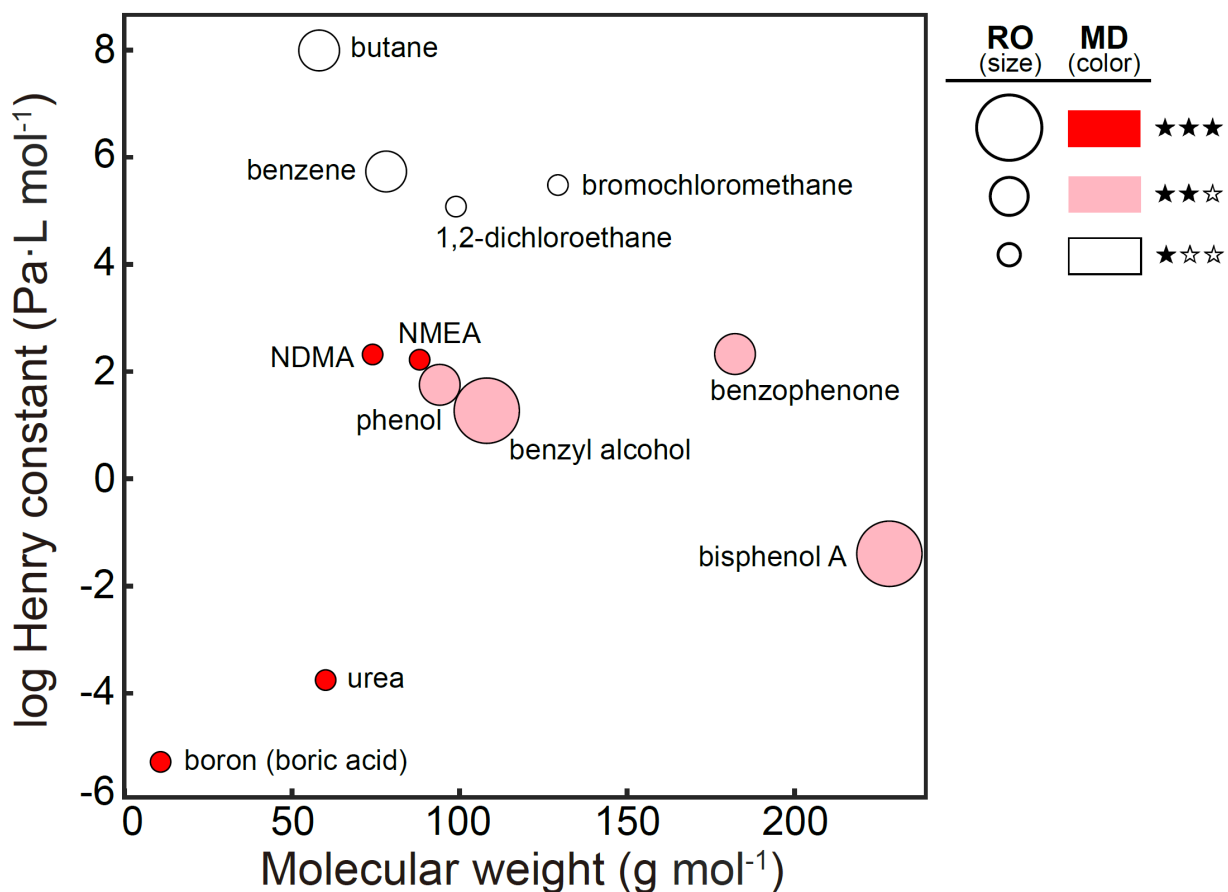
Figure 4.6 Comparison of the removal of various compounds in RO and DCMD as a function of the molecular weight and Henry's constant. 3-stars indicates high rejection (> 80%) and 1-star indicates low rejection (< 40%). Color is associated with DCMD, and circle size is associated with RO.

4.4 Conclusions

In this study, we evaluate the mass transport of a wide range of semi-volatile and volatile compounds in DCMD. The results allow us to gain broad insights into the compound properties, system designs, and operating conditions that impact solute rejection. The results show that the Henry's constant is the primary determining factor in the solute flux of a given compound. Based on the Henry's constant, we can define solute transport regimes dictated by either membrane resistances or boundary layer resistances. For compounds in the membrane resistance regime, the

Henry's constant and membrane properties play a strong role in determining the solute flux. The solute flux of compounds in the boundary layer resistance regime is primarily dependent on the diffusion coefficient of a given compound and hydrodynamic conditions that impact the mass transfer coefficient (e.g., the crossflow velocity). Thus, depending on the transport regime, solute flux can depend on completely different factors.

Large-scale analysis was used to show the impact of membrane area, operating temperature, and crossflow velocity on the equilibrium ratio (i.e., the ratio of compounds concentration in the permeate to the feed). Larger membrane areas diminished the temperature difference between the feed and the permeate sides, and thus, the volatile compounds in the feed and permeate approached equal concentrations. Raising crossflow velocity increased the equilibrium ratios due to increased mass transfer coefficients, and high crossflow velocities will be disadvantageous for preventing transport of volatile compounds.

Building on the analysis of selectivity in MD, the rejections of different compounds in RO and MD were compared. MD showed advantages over RO for neutral low molecular weight compounds with low volatility including *N*-nitrosodimethylamine, urea, and boron. MD can also concentrate highly volatile compounds in the permeate side if the Henry's constant difference between the feed and permeate sides greater than 500-1000 Pa·L mol^{-1}.

Overall, the results of this work allow for an improved fundamental understanding of the factors that govern the transport of semi-volatile and volatile contaminants in MD. Based on the insights from this work, the important molecular properties and operating conditions that influence solute transport in different regimes can be better understood. We expect that insights from this work will allow for the construction of membrane modules that tune design and operation to

achieve the desired flux or rejection of volatile solutes. Future work should focus on further experimentally characterizing the flux of volatile solutes in MD systems.

CHAPTER 5

Omniphobic membranes with re-entrant structures for separating low surface tension liquids in pressure-driven distillation

5.1 Introduction

Global water scarcity is driving the development of efficient and highly selective membrane-based separations that can be applied in desalination and water reuse. Pressure-driven distillation (PD) is an emerging membrane process that uses applied hydraulic pressure to drive water vapor flow through an air-trapping porous hydrophobic membrane. The phase-change separation mechanism of PD allows for nearly complete rejection of non-volatile contaminants, including low molecular weight neutral solutes (e.g., urea, boron, and N-nitrosodimethylamine) that pass through conventional reverse osmosis membranes. PD membranes can also be made from hydrophobic materials that resist damage from strong oxidants (for example, chlorine and ozone), and allow for treatment of strongly acidic or alkaline solutions. Unlike thermal distillation technologies, such as multi-stage flash or thermal membrane distillation, which consume large amounts of heat energy to conduct separations, PD can potentially offer high separations efficiencies comparable to those of reverse osmosis and facile implementation since only applied pressure is used as a driving force.

Although PD can offer benefits in separation performance, the structure of PD membranes leaves them vulnerable to wetting, a phenomenon where liquid enters the membrane pores and compromises the vapor gap. Such wetting results in a complete loss of selectivity and can occur when the membrane is exposed to oils, surfactants, and low surface tension liquids often encountered in water treatment and industrial separations. Hydrophobic membranes employing

vapor gaps to separate the feed and permeate streams are susceptible to pore wetting (i.e., liquid water entering the membrane pores), which eventually results in failure of the system. It is imperative that the membrane pores do not become wet by infiltrating liquids and conserve the selective barrier of air for blocking unwanted solutes. The prevention of pore wetting has been a challenging issue in treating low surface tension liquids such as the mixture of water and organic solvents or shale gas produced water with a high level of surfactants.[174] The presences of the substances decrease the surface tension force at the liquid and vapor interface, and lead to reducing the liquid entry pressure (LEP) of a pore. Successful fabrication of vapor-gap RO membranes that offer both robust wetting resistance and fast transport rates will allow for direct replacement of conventional RO membranes, enabling dramatically improved efficiency in desalination and industrial separations processes.

Recent advances in our understanding of the wetting have led to development of robust omniphobic materials and membrane, but few studies have focused on omniphobic materials that can prevent wetting with a large pressure difference across the air-liquid interface. To overcome the issue of wetting, previous studies introduced biomimetic designs with re-entrant structures to ensure local meta-stable states before landing the equilibrium wetted state.[175–177] The re-entrant structures render the liquid-vapor interface tighter by changing the force directions at the interface ends, and thus, they showed higher LEPs even for low surface tension liquids.[174,178] Nevertheless, those superhydrophobic membranes with re-entrant structures have been designed for MD applications. Although, they showed very high contact angles even for low surface tension liquids LEP values of the omniphobic membranes were not tested under PD scheme, which was only introduced by previous researchers as an experimental proof of the concept.[179,180] Since those membranes had pores in the range of 0.1-0.5 µm, it may be difficult for them to induce high LEP

values.[15,16] This study will be an initiator to broaden impact of pressure-driven membrane filtration with better selectivity and fouling control, even treating challenging mixtures having low surface tension. For example, pressure-driven membrane processes have been widely used for oil-in-water emulsions in oil/gas industry, surfactant-laden wastewater (such as shale-gas produced water, textile industry wastewater, and detergents), and organic solvent separations in chemical and pharmaceutical industries, and selectivity and permeability of the polymer membranes can be damaged due to the feeds. The use of omniphobic membranes with high LEPs in these applications can bring better selectivity and fouling control, and eventually lead to improved separation efficiency.

In this study, we fabricate pressure-resistant omniphobic membranes by grafting re-entrant nanostructures to the surface. Re-entrant structures are achieved by coating silica nanoparticles (SiNPs) on the anodic aluminum oxide (AAO) membrane surface, followed by subsequent surface fluorination using vapor deposition. Re-entrant structures from SiNPs are confirmed in the SEM images, and fluorination is analyzed by XPS. We then examine the wetting behavior of the membrane using LEP measurements, extracting the approximate re-entrant angle of the substrate. Finally, we demonstrate desalination of low surface tension liquid and compare performance to membranes without onmiphobic structures. Overall, this work proved improved wetting resistance for treating low surface tension liquids under hydraulic pressure.

5.2 Methods

5.2.1 Surface modification procedure

Anodic aluminum oxide samples with a pore diameter of 40 nm were purchased from InRedox. The samples were annealed at 900 °C for 2 hours. Subsequently, the membranes were hydroxylated by using a UV/Ozone cleaner for 5 minutes. (3-Aminopropyl)triethoxysilane (APTES) was grafted on the resulting membrane via vapor deposition in vacuum at 30 °C for 2 hours. The membrane was rinsed in DI water and dried at 100 °C for 20 minutes. 5% wt. silica nanoparticle (SiNP) solution was sonicated in a bath for 20 minutes to avoid particle aggregations, and the membrane was immersed in the SiNP solution with a gentle mixing for 3 hours. Afterward, the membrane was rinsed in DI water and dried at 100 °C for 1 hour. Lastly, (heptadecafluoro-1,1,2,2-tetrahydrodecyl)triethoxysilane (FAS-16) were deposited on the membrane in gas phase in a vacuum oven at 90-100 °C overnight, then the membrane was dried at 90-100 °C for 2 hours before further testing.

5.2.2 Materials Characterization

Field Emission Scanning electron microscopy (FESEM) images were obtained on a JEOL JSM-7401F (Tokyo, Japan) using magnifications of 50K, 70K, and 200K. Samples were coated with 1 nm of platinum before FESEM to avoid charging. The surface elemental composition of the membranes through the fabrication process was confirmed with X-ray photoelectron spectroscopy (XPS. Kratos Supra, Kratos Analytical, UK). The samples were irradiated with a monochromatic Al K beam with a source energy of 1486.69eV, a X-ray beam power of 225W and resolution of 225W. The charge neutralizer was turned on for the samples with a filament current, filament bias and charge balance of 0.35A, 1.3V and 4V respectively. CasaXPS software was used to determine the elemental surface composition and corresponding atomic percentages, and Shirley model was used as a background type for the survey spectra's.

5.2.3 Liquid entry pressure (LEP) and flux measurements

Liquid entry pressure was measured using a dead-end cell. The examined membrane lay between an upper and lower metal holder with a Viton o-ring and metal frit. Different ethanol and water mixture solutions were used, and their surface tensions (5, 15, and 40% wt.) were obtained in the previous literature.[181] The upper part was filled up with feed solutions such as DI water (72 mN/m) or different water/ethanol mixtures (31, 43, and 56 mN/m) and connected to a pressurized nitrogen gas cylinder through a regulator, which generated external pressure on the system. The applied pressure was increased in 20-50 psi every 2 hours. Typically, the LEP of a MD membrane was measured by increasing pressure at a minute interval. Unlike MD, PD is designed to be operated under pressure, so it needed more strict LEP measurements. So, two-hour interval was used in our LEP tests before proceeding with increasing pressure. The LEP values were decided when feed solutions seeped through membranes as monitoring the outside of the permeate side.

Measurements of flux and salt rejection were conducted using a dead-end cell immersed in a DI water bath. The dead-end cell and adjacent tubing were immersed in the bath for regulating temperature (40 and 25 °C). The feed side was filled with 0.05M NaCl aqueous solution or the 15% water/ethanol mixture with 0.05M NaCl concentration, and the permeate side was filled with DI water to measure the permeate volume increments and salt passage. The operating pressures were 200 and 100 psi for the feed of aqueous solution and the 15% ethanol solution. Before logging data points, the system was stabilized for 2 hours under constant temperature and pressure. Flux was calculated by monitoring the volume gain in the permeate tube. A high-resolution web camera (Logitech C390s, CA, USA) and a tape measure were used to track volume changes as a function of time. Rejection was calculated by obtaining electrical conductivity of initial and terminal

solutions in the permeate tube. The electrical conductivity probe was calibrated with standard solutions beforehand, and the increased permeate salt mass during a time interval was divided with the volume increment to get a permeate NaCl concentration excluding dilution from the initial permeate volume.

5.3 Results and Discussion

Pressure-driven distillation uses applied hydraulic pressure to create a partial vapor pressure difference that drives vapor flow through air-trapping porous hydrophobic membranes (Figure 5.1a). The ability of membranes with cylindrical pores to resist membrane wetting is defined by the Young-Laplace equation and is highly dependent on pore size and contact angle of a liquid on the membrane (eq 42). Schematic diagrams of the pore structures of the membranes with cylindrical pores and membranes with re-entrant pore structures are shown in Figure 5.1b and c. In this study, cylindrical pores were tested using hydrophobic anodic aluminum oxide (AAO) membranes and membranes with a re-entrant structure were fabricated by modifying membranes with hydrophibic spherical silica nanoparticles. The cylindrical pore structure of the control AAO membrane may have liquid-gas interface staying below the pore entrance when applied pressure exists. Then, the contact point where liquid, gas, and solid phases meet lies on the vertical pore wall, and tension along the pore wall causes zero re-entrant structure angle.[182] In this scenario, air is typically trapped at the top of the pore, forming a barrier that prevents liquids from entering. On the other hand, the pore entrance with silica nanoparticles sitting on the top can induce a re-entrant structure angle that generates a horizontal force against liquid-vapor interface expansion downward, the pore entrances with re-entrant structures can cause metastable states that prevent

wetting. Air can be trapped within the smaller pockets formed by the re-entrant structure, and this results in an even stronger barrier against liquid penetration according to the Cassie-Baxter principle, as the air pockets are more difficult to displace.

$$\Delta P = \frac{2\gamma}{r}\cos\theta \tag{42}$$
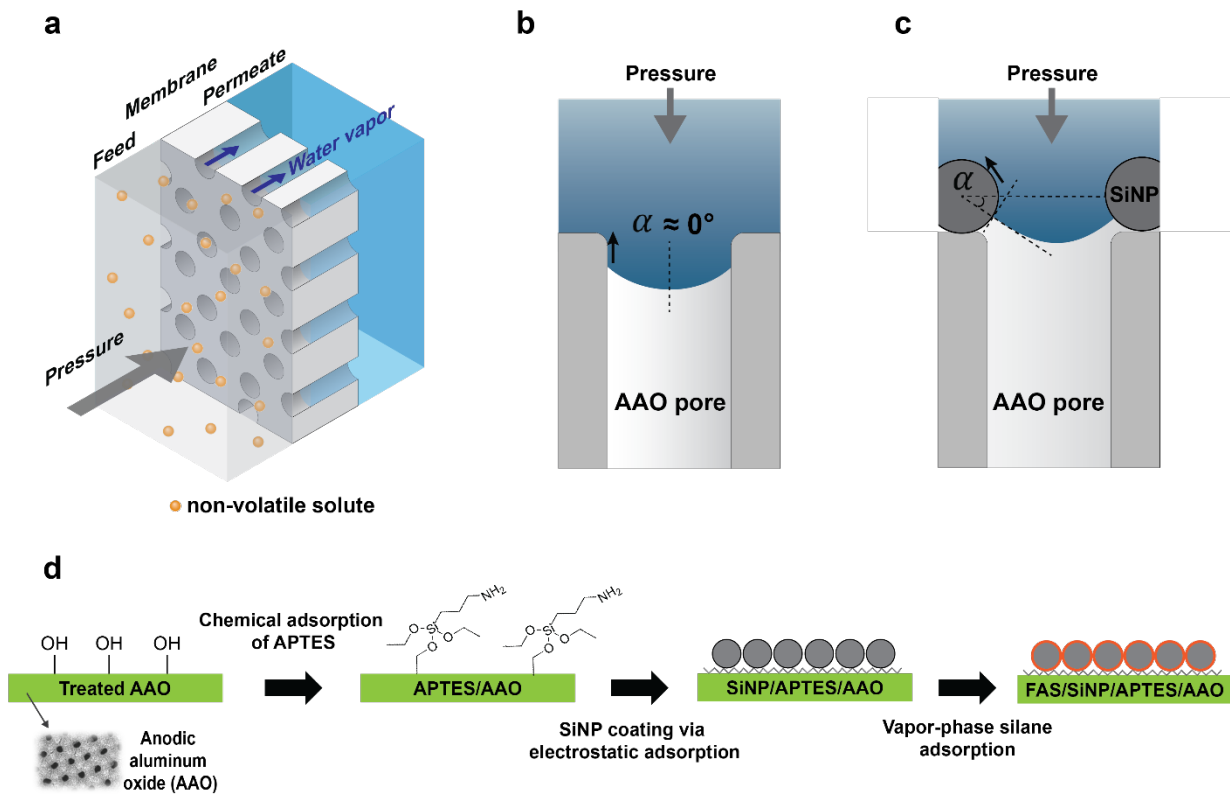
Figure 5.1 (a) Schematic diagram of pressure-driven distillation (PD) system. Demonstration of the pore and water-vapor interface on (b) a cylindrical membrane pore and (c) a pore with re-entrant structures created using nanoparticle deposition. (d) Procedures of the membrane surface modification for making omniphobic membranes. Initially, a pristine AAO membrane is annealed at 900 °C for 2 hours, then the hydroxyl groups of the membrane are activated by a UV/Ozone cleaner. After FAS hydrophobic coating, the membrane becomes omniphobic with re-entrant structures and low surface energy.

5.3.1 Membrane characterization

Surface modification of isoporous AAO membrane was performed using liquid and vapor deposition procedures (Figure 5.1d). Raw AAO membranes were annealed at 900 °C for 2 hours to make more uniform polycrystalline pore structures, and the pore structure of the annealed membrane is shown in Figure 5.2a. UV/Ozone was used to clean and hydroxylate the surface of the membrane, and APTES was used to graft amino groups to the membrane surface. The amino-functionalized membrane surface becomes positively charged and electrostatic attraction was used to deposit negatively charged silica nanoparticles on the surface. After electrostatic deposition of particles, the surfaces of the nanoparticles and membrane were coated with (heptadecafluoro-1,1,2,2-tetrahydrodecyl)triethoxysilane (FAS-16) to render the surface hydrophobic.

The pristine AAO membrane had an isoporous hexagonal structure that was observed in SEM imaging (Figure 5.2a). After modification, a uniform coverage of SiNPs was observed with the hexagonal structure of AAO still visible in imaging (Figure 5.2b). The magnified and cross-section SEM images in Figure 5.2b and c indicate that a pore entrance (40 nm diameter) had 4-5 particles (22 nm diameter), and particles mostly coated the top 0.2-0.4 μm of the pores but did not penetrate deep into the 50 μm thick AAO membrane to block the pores

XPS analysis was used to confirm surface modification and particle deposition throughout the modification procedures at each modification step (Figure 5.2d). The elemental composition of pristine AAO, AAO/APTES and AAO/SiNP/FAS were confirmed with XPS survey scans. Pristine AAO shows the presence of two peaks at 73 eV and 99 eV corresponding to Al 2p and Si 2p, respectively, along with a 284 eV peak associated with C 1s (adventitious carbon common in samples exposed to ambient air).[183] Following the activation of the AAO surface and subsequent deposition of the APTES molecule, peaks for Si 2p and N 1s appear at 99 eV and 399 eV,

respectively. The carbon peak also increases in intensity which is to be expected after the APTES

modification given that the molecule contains a three-carbon chain. Finally, after the deposition of

the silica nanoparticles and coating of the fluorosilane molecule, the Si 2p peak intensity increases

and while a peak at 686 eV appears, indicating the presence of a F 1s molecule.
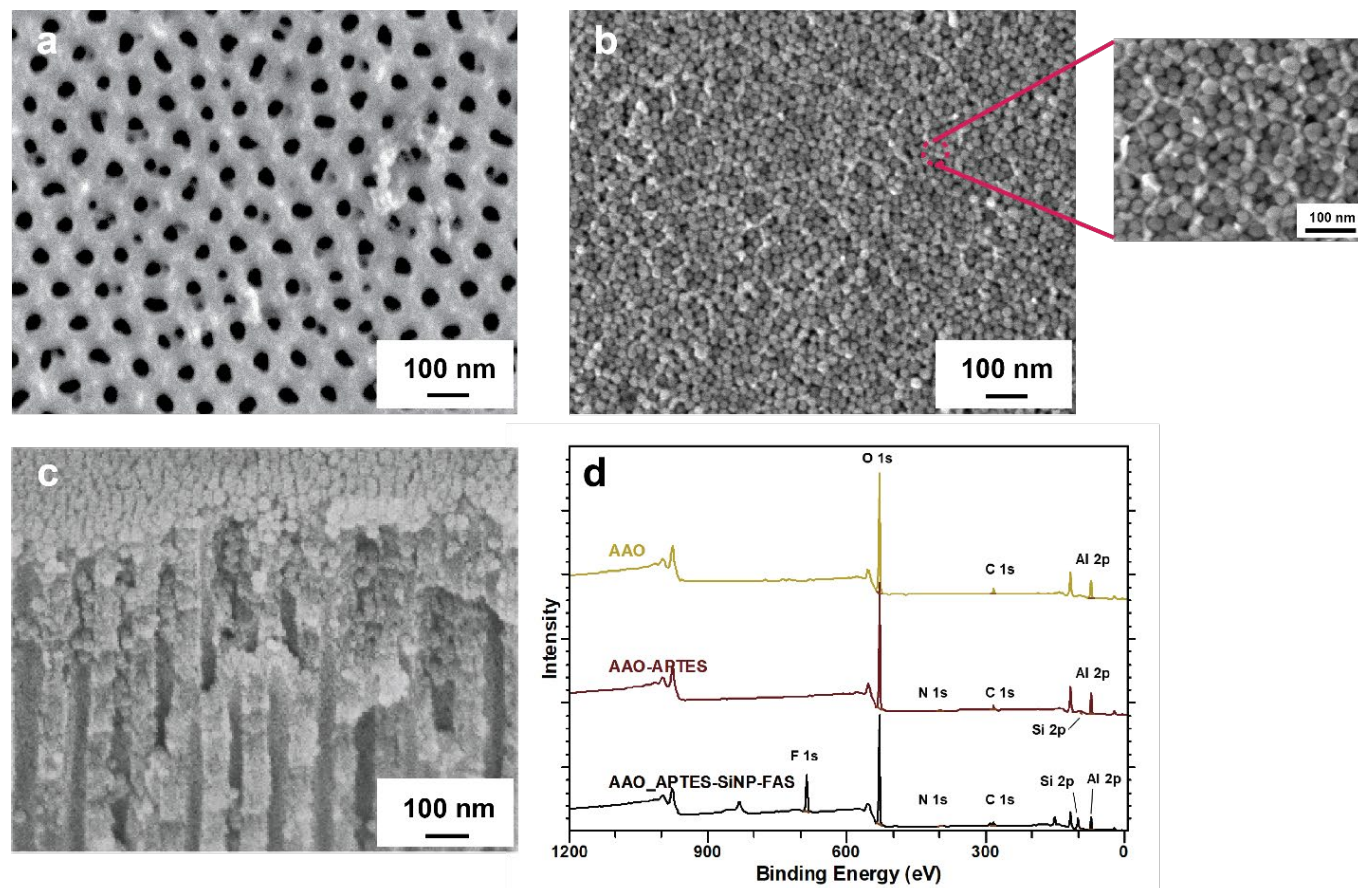
Figure 5.2 SEM images of (a) pristine AAO membrane, (b) modified AAO membrane with SiNPs and FAS-16, and magnified pores and particles of the modified AAO membrane, (c) cross-section of the modified AAO membrane. (d) XPS spectra of the pristine AAO membrane, the AAO membrane coated with APTES, and the APTES, SiNPs, and FAS deposited AAO membrane.

Contact angles for water and a water-ethanol mixture are shown in Figure 5.3. Contact

angle was measured on the hydrophobic AAO membrane control (cylindrical pore structure) and

the omniphobic AAO membrane modified with silica nanoparticles (re-entrant pore structure).

104

Water contact angles of both membranes were 130–140°. These angles were greater than the expected contact angle of the hydrophobic coating since the rough and porous structure of both membranes resulted in a Cassie-Baxter state, where entrapped air contributes to a higher contact angle. The water-ethanol mixture contained 40% weight of ethanol, and the surface tension of the mixture was 31 mN/m.[181] The contact angles of the water-ethanol mixture with control and omniphobic membranes were 96° and 112°, respectively. The higher contact angle in the omniphobic membrane is consistent with our understanding that re-entrant structures will prevent liquid water penetration in the membrane pores.
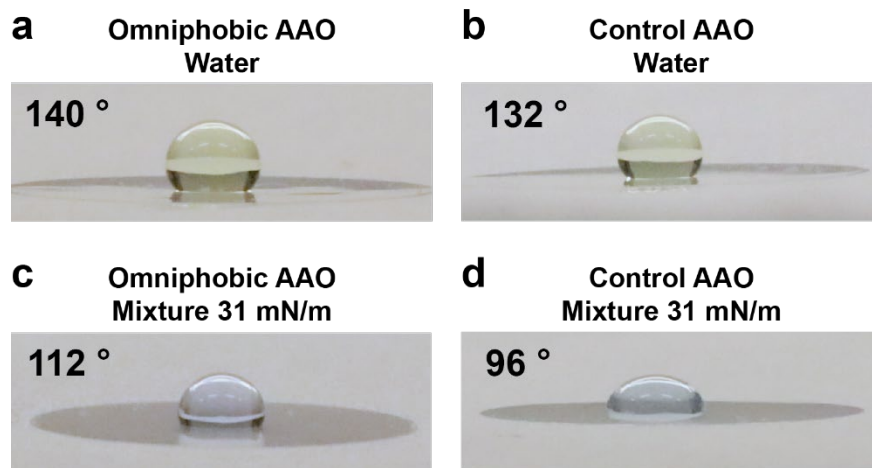
Figure 5.3 (a) Contact angle photograph of the omniphobic AAO membrane for water. (b) Contact angle photograph of the control AAO membrane for water. (c) Contact angle photograph of the omniphobic AAO membrane for the 31 mN/m surface tension mixture. (d) Contact angle photograph of the control AAO membrane for the 31 mN/m surface tension mixture.

5.3.2 Wetting resistance of omniphobic membranes under applied pressure.

Since PD uses applied hydraulic pressure as a driving force for water permeation, reaching high pressure without wetting the membrane is imperative. Avoiding pore wetting is made more challenging when working with low surface tension liquids, which can more easily penetrate into

membrane pores under pressure. Re-entrant structures were built on the membrane surfaces using silica nanoparticles, in order to improve wetting resistance for low surface tension liquids under external pressure. The measured and predicted liquid entry pressure (LEP) values for the control and omniphobic AAO membranes are shown in Figure 5.4a. The measured LEP values for the control membrane were 24.45, 14.48, 4.83, and 0 bar for water (72 mN/m), 5% mixture (56 mN/m), 15% mixture (43 mN/m), and 40% mixture (31 mN/m). The control membrane, which had cylindrical pores, showed a severe decline in LEP as the liquid surface tension decreased. In contrast, the measured LEP values for the omniphobic AAO membranes were 36.20, 24.48, 15.52, and 5.18 bar for water, 5% mixture, 15% mixture, and 40% mixture. The higher LEP values for omniphobic membranes indicated that the surface modification with re-entrant structures could lead to high wetting resistance. The impact of the omniphobicity was especially apparent for the lowest surface tension liquid, which readily wetted the control membrane but had an LEP of 5.18 bar for the omniphobic membranes.

The importance of re-entrant structures in preventing wetting with low surface tension liquid was confirmed using theoretical modeling. Equation 43 was used to determine the expected LEP behavior for different surface tension liquids, where the re-entrant structure angle, α, and the pore radius, r, were treated as fitting parameters using least-squares minimization. For the control membrane, the fitted re-entrant angle was -3°, consistent with our understanding that the pristine AAO pores are cylindrical without re-entrant structures. For the modified membranes, the re-entrant angle was -24°, indicating that the silica nanoparticles led to the formation of re-entrant structures. LEP values for the different surface tension liquids calculated using the fitted angles showed strong agreement with the experimental values overall (solid and dashed lines in Figure 5.4a) with root mean squared errors of 5.63 and 6.18 bar for the control and omniphobic

membranes, respectively. We note that decreases in the pore size due to the nanoparticle deposition in the omniphobic membranes did not appear to fully explain the improved LEP behavior (Figure SX). We therefore concluded that the main contribution of the omniphobic layer in improve the LEP was the formation of re-entrant structure.

$$\Delta P = \frac{2\gamma}{r} \frac{\cos(\theta - \alpha)}{1 + \frac{R}{r}(1 - \cos\alpha)} \tag{43}$$
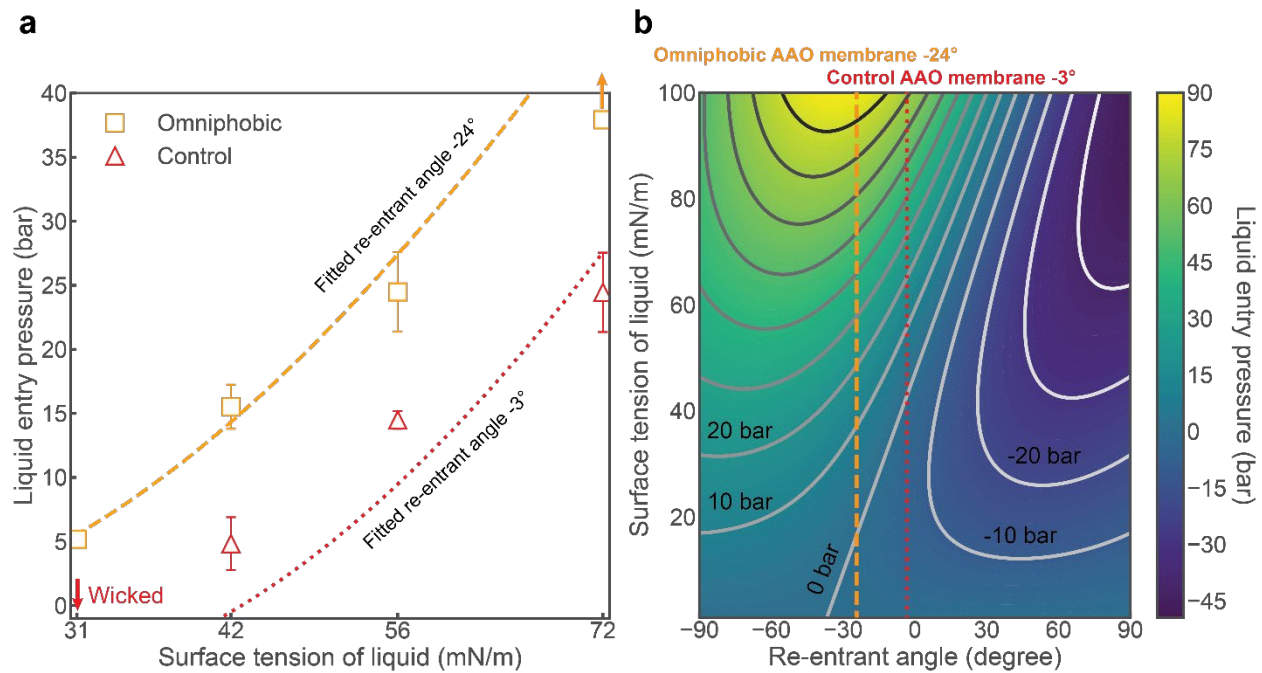
Figure 5.4 (a) Measured and predicted liquid entry pressures of the omniphobic and control AAO membranes for four different solvents (40% ethanol mixture, 15% ethanol mixture, 5% ethanol mixture, and water). Fitted re-entrant angle for each membrane was found using least square fitting of the experimental data. The red arrow at the left lower corner indicates that the control membranes became wicked immediately. The orange arrow at the right upper corner indicates that the omniphobic membrane did not get wet at the pressure, but we stopped the tests without going further up. (b) LEP changes along with varying surface tension and re-entrant angle caused by spherical particles. Particle radius of 11 nm and pore radius of 20 nm were used for the simulations.

To explore the range of LEPs possible with different surface tension liquids and membrane designs, LEP values induced by spherical re-entrant structures were simulated with different sets

of surface tensions and angles (Figure 5.4b). High LEPs are desirable for obtaining a higher driving force for vapor transport, and the surface tension depends on the target liquid. Re-entrant structure angle of particles varied from -90 to 90 degrees. The range of 1-100 mN/m was used for surface tension of liquid. The results highlight the importance of the re-entrant angle in obtaining high LEP values for low surface tension liquids. Before reaching the critical value, a larger angle is favorable to increase LEP, but beyond the critical angle LEP started decreasing. Varying critical angle depending on surface tension can be obtained by Equation 3. This is because the horizontal force induced by re-entrant angle decreases over the critical angle, and the vertical force component starts increasing. Lower surface tension required higher critical angle for achieving their maximum LEPs. This is because advancing low surface tension liquid can move further through the pore, compared to high surface tension liquid. In addition, lower surface tension than 20 mN/m was not able to bring positive LEP values and the highest achievable LEP in Figure 5.4b was about 90 bar. For example, the surface tensions of hexane and perfluoropentane are only 18 and 9.5 mN/m, and a LEP of 120 bar, which is required for ultra-high salinity brine treatment, was not able to be achieved in the given modeling space. For those organic solvents and ultra-high salinity brine, more robust re-entrant structures (e.g. multiple overhangs) will be required to resist pore wetting. When it comes to the control membranes, the lowest surface tension achieving positive LEP was around 40 mN/m, which was 2 times high compared to that of the omniphobic AAO membrane. The surface tension of shale gas produced water is assumed around 40 mN/m,[184] and thus, our omniphobic membranes are expected to run between 10-20 bar for produced water treatment, where the control membranes are on the verge of wetting.

$$\sin(\theta - \alpha) = \frac{\sin\theta}{1 + \dfrac{r}{R}} \tag{44}$$

5.3.3 Mass transport for separating water and low surface tension liquids in pressure-driven distillation system

The LEP results above showed that the omniphobic membranes were more resistant to wetting under pressure. Here, the effect of the particle layers on mass transport and the stability under long-term operation in PD system were examined. The performance tests with a dead-end membrane cell were conducted at 40 and 25 °C under the operating pressures of 200 and 100 psi for the feeds with 0.05 M NaCl aqueous solution and 0.05 M NaCl 15% ethanol mixture, respectively. The volume changes in the permeate tube and the electrical conductivity were recorded during the runs to calculate flux and rejection. In Figure 5.5a, the water fluxes of the control and omniphobic membranes were 0.07 and 0.12 LMH, and the NaCl rejections were 99 and 98%. The omniphobic membrane had slightly higher water flux than the control AAO membrane probably due to the enlarged liquid-vapor interface area with high roughness.[185] In addition, the feed of the 15% ethanol mixture with the surface tension of 43 mN/m was introduced to confirm a stable operation with low surface tension liquids. Herein, commercial PTFE membranes (Pall Corporation) were used during the performance tests. Although commercial PTFE membranes are fibrous and have different shapes from cylindrical AAO membranes, they were compared because they are widely used and have well-established performance benchmarks. The PTFE membranes and the control AAO membranes got wicked below 100 psi with the 43 mN/m liquid during the LEP tests. In Figure 5.5b, the commercial PTFE membrane showed 25 times higher flux compared to the omniphobic AAO membrane tests, and the measured rejection was low as 54%, which indicates the PTFE membrane became wet. In comparison, the performances of the omniphobic AAO membranes were robust. The measured fluxes were 0.02-0.04 during 48 and 24 hours of operations, and the rejection values were maintained as 97% under 100 psi. The robust wetting-resistance can be attributable to the combination of the low surface energy coating (FAS-16) and the re-entrant

structures formed by SiNPs. The control AAO membranes and PTFE membranes were not able to bring metastable Cassie-Baxter states for low surface tension liquids, however, the introduction of the re-entrant structures onto the nanoporous AAO made the transition from Cassie-Baxter state to Wenzel state unfavorable, which made higher liquid entry pressures.
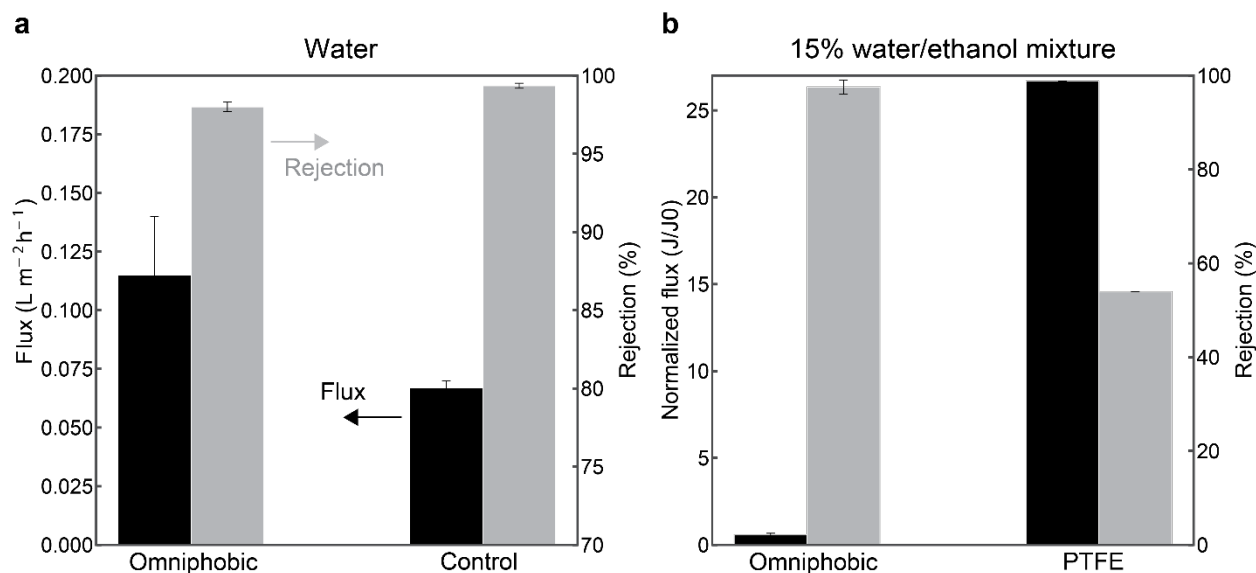
Figure 5.5 (a) Flux and rejection measurements of the omniphobic and control AAO membranes with the feed of water. The operating temperature and pressure were 40°C and 200 psi. (b) Flux and rejection measurements of the omniphobic AAO and commercial PTFE membranes with the feed of 15% ethanol mixture (43 mN/m). The operating temperature and pressure were 25°C and 100 psi.

5.4 Conclusions

We fabricated omniphobic AAO membranes with re-entrant structures and demonstrated their application in pressure-driven distillation for treating low surface tension liquids. Building re-entrant structures on the membrane surfaces can make membranes resist wetting from low surface tension liquids even under external pressure so that feeds waters containing surfactant or low surface tension liquids can be treated. Omniphobic membranes, fabricated by depositing spherical

nanoparticles on a porous substrate, showed higher wetting resistance for water and ethanol mixtures compared to control membranes with cylindrical pores. The LEP calculation confirmed that the omniphobic membrane can theoretically produce a positive LEP with liquid surface tensions down to 18 mN/m. In the flux and rejection measurements, stable operation with the 43 mN/m surface tension feed under 100 psi were realized for 24 and 48 hours with the high salt rejection of 97%. Our work here has focused on proof-of-concept testing using a nanoparticle modification, but recent developments in engineered nanostructures indicate that more sophisticated designs with higher re-entrant angle may further improve the wetting resistance of hydrophobic membranes.

REFERENCES

(1)   Mekonnen, M. M.; Hoekstra, A. Y. Sustainability: Four Billion People Facing Severe Water Scarcity. *Sci Adv* **2016**, *2* (2). https://doi.org/10.1126/SCIADV.1500323/SUPPL_FILE/1500323_SM.PDF.

(2)   UN Water. *The United Nations World Water Development Report 2022: Groundwater: Making the Invisible Visible*; 2020.

(3)   UNDP. *Human Development Report*; 2022.

(4)   Sedlak, D. L. The Unintended Consequences of the Reverse Osmosis Revolution. *Environ. Sci. Technol.* **2019**.

(5)   Shenvi, S. S.; Isloor, A. M.; Ismail, A. F. A Review on RO Membrane Technology: Developments and Challenges. *Desalination* **2015**, *368*, 10–26. https://doi.org/10.1016/J.DESAL.2014.12.042.

(6)   Fujioka, T.; O'Rourke, B. E.; Michishio, K.; Kobayashi, Y.; Oshima, N.; Kodamatani, H.; Shintani, T.; Nghiem, L. D. Transport of Small and Neutral Solutes through Reverse Osmosis Membranes: Role of Skin Layer Conformation of the Polyamide Film. *J Memb Sci* **2018**, *554*, 301–308. https://doi.org/10.1016/J.MEMSCI.2018.02.069.

(7)   Park, H. B.; Kamcev, J.; Robeson, L. M.; Elimelech, M.; Freeman, B. D. Maximizing the Right Stuff: The Trade-off between Membrane Permeability and Selectivity. *Science (1979)* **2017**, *356* (6343), 1138–1148. https://doi.org/10.1126/SCIENCE.AAB0530/ASSET/1FAB46CE-E045-4C54-80A4-6FD3685D9AEA/ASSETS/GRAPHIC/356_AAB0530_F5.JPEG.

(8)   Lee, J.; Straub, A. P.; Elimelech, M. Vapor-Gap Membranes for Highly Selective Osmotically Driven Desalination. *J Memb Sci* **2018**, *555*, 407–417. https://doi.org/10.1016/J.MEMSCI.2018.03.059.

(9)   Khayet, M. Membranes and Theoretical Modeling of Membrane Distillation: A Review. *Advances in Colloid and Interface Science*. Elsevier B.V. May 11, 2011, pp 56–88. https://doi.org/10.1016/j.cis.2010.09.005.

(10)   Ongaratto, R. S.; Menezes, L.; Borges, C. P.; Laranjeira da Cunha Lage, P. Osmotic Distillation Applying Potassium Pyrophosphate as Brine. *J Food Eng* **2018**, *228*, 69–78. https://doi.org/10.1016/j.jfoodeng.2018.02.013.

(11)   Cassano, A.; Drioli, E. Concentration of Clarified Kiwifruit Juice by Osmotic Distillation. *J Food Eng* **2007**, *79* (4), 1397–1404. https://doi.org/10.1016/j.jfoodeng.2006.04.021.

(12)   Winglee, J. M.; Bossa, N.; Rosen, D.; Vardner, J. T.; Wiesner, M. R. Modeling the Concentration of Volatile and Semivolatile Contaminants in Direct Contact Membrane

Distillation (DCMD) Product Water. *Environ Sci Technol* **2017**, *51* (22), 13113–13121. https://doi.org/10.1021/acs.est.6b05663.

(13)   Wijekoon, K. C.; Hai, F. I.; Kang, J.; Price, W. E.; Cath, T. Y.; Nghiem, L. D. Rejection and Fate of Trace Organic Compounds (TrOCs) during Membrane Distillation. *J Memb Sci* **2014**, *453*, 636–642. https://doi.org/10.1016/j.memsci.2013.12.002.

(14)   Ni, T.; Lin, J.; Kong, L.; Zhao, S. Omniphobic Membranes for Distillation: Opportunities and Challenges. *Chinese Chemical Letters* **2021**. https://doi.org/10.1016/j.cclet.2021.02.035.

(15)   Lu, K. J.; Chen, Y.; Chung, T. S. Design of Omniphobic Interfaces for Membrane Distillation – A Review. *Water Res* **2019**, *162*, 64–77. https://doi.org/10.1016/J.WATRES.2019.06.056.

(16)   UN Water. *UN World Water Development Report, Nature-based Solutions for Water*. http://repo.floodalliance.net/jspui/handle/44111/2726 (accessed 2022-07-25).

(17)   Tang, C. Y.; Yang, Z.; Guo, H.; Wen, J. J.; Nghiem, L. D.; Cornelissen, E. Potable Water Reuse through Advanced Membrane Technology. *Environ Sci Technol* **2018**, *52* (18), 10215–10223. https://doi.org/10.1021/ACS.EST.8B00562/ASSET/IMAGES/LARGE/ES-2018-00562B_0003.JPEG.

(18)   Yang, Q.; Wang, K. Y.; Chung, T. S. A Novel Dual-Layer Forward Osmosis Membrane for Protein Enrichment and Concentration. *Sep Purif Technol* **2009**, *69* (3), 269–274. https://doi.org/10.1016/j.seppur.2009.08.002.

(19)   Cui, Y.; Chung, T. S. Pharmaceutical Concentration Using Organic Solvent Forward Osmosis for Solvent Recovery. *Nature Communications 2018 9:1* **2018**, *9* (1), 1–9. https://doi.org/10.1038/s41467-018-03612-2.

(20)   Lutchmiah, K.; Verliefde, A. R. D.; Roest, K.; Rietveld, L. C.; Cornelissen, E. R. Forward Osmosis for Application in Wastewater Treatment: A Review. *Water Research*. Elsevier Ltd July 1, 2014, pp 179–197. https://doi.org/10.1016/j.watres.2014.03.045.

(21)   Sant'Anna, V.; Marczak, L. D. F.; Tessaro, I. C. Membrane Concentration of Liquid Foods by Forward Osmosis: Process and Quality View. *Journal of Food Engineering*. Elsevier August 1, 2012, pp 483–489. https://doi.org/10.1016/j.jfoodeng.2012.01.032.

(22)   Egea-Corbacho Lopera, A.; Gutiérrez Ruiz, S.; Quiroga Alonso, J. M. Removal of Emerging Contaminants from Wastewater Using Reverse Osmosis for Its Subsequent Reuse: Pilot Plant. *Journal of Water Process Engineering* **2019**, *29*, 100800. https://doi.org/10.1016/J.JWPE.2019.100800.

(23)   Petrie, B.; Barden, R.; Kasprzyk-Hordern, B. A Review on Emerging Contaminants in Wastewaters and the Environment: Current Knowledge, Understudied Areas and

Recommendations for Future Monitoring. *Water Res* **2015**, *72*, 3–27. https://doi.org/10.1016/J.WATRES.2014.08.053.

(24) Cabeza, Y.; Candela, L.; Ronen, D.; Teijon, G. Monitoring the Occurrence of Emerging Contaminants in Treated Wastewater and Groundwater between 2008 and 2010. The Baix Llobregat (Barcelona, Spain). *J Hazard Mater* **2012**, *239–240*, 32–39. https://doi.org/10.1016/J.JHAZMAT.2012.07.032.

(25) Coday, B. D.; Yaffe, B. G. M.; Xu, P.; Cath, T. Y. Rejection of Trace Organic Compounds by Forward Osmosis Membranes: A Literature Review. *Environ Sci Technol* **2014**, *48* (7), 3612–3624. https://doi.org/10.1021/ES4038676/ASSET/IMAGES/LARGE/ES-2013-038676_0001.JPEG.

(26) Radjenović, J.; Petrović, M.; Ventura, F.; Barceló, D. Rejection of Pharmaceuticals in Nanofiltration and Reverse Osmosis Membrane Drinking Water Treatment. *Water Res* **2008**, *42* (14), 3601–3610. https://doi.org/10.1016/J.WATRES.2008.05.020.

(27) Jeong, N.; Chung, T.; Tong, T. Predicting Micropollutant Removal by Reverse Osmosis and Nanofiltration Membranes: Is Machine Learning Viable? *Environ Sci Technol* **2021**, *55* (16), 11348–11359. https://doi.org/10.1021/ACS.EST.1C04041.

(28) Ignacz, G.; Szekely, G. Deep Learning Meets Quantitative Structure–Activity Relationship (QSAR) for Leveraging Structure-Based Prediction of Solute Rejection in Organic Solvent Nanofiltration. *J Memb Sci* **2022**, *646*, 120268. https://doi.org/10.1016/J.MEMSCI.2022.120268.

(29) Gupta, S.; Aga, D.; Pruden, A.; Zhang, L.; Vikesland, P. Data Analytics for Environmental Science and Engineering Research. *Environ Sci Technol* **2021**, *55* (16), 10895–10907. https://doi.org/10.1021/ACS.EST.1C01026.

(30) Yangali-Quintanilla, V.; Verliefde, A.; Kim, T. U.; Sadmani, A.; Kennedy, M.; Amy, G. Artificial Neural Network Models Based on QSAR for Predicting Rejection of Neutral Organic Compounds by Polyamide Nanofiltration and Reverse Osmosis Membranes. *J Memb Sci* **2009**, *342* (1–2), 251–262. https://doi.org/10.1016/J.MEMSCI.2009.06.048.

(31) Lee, S.; Kim, J. Prediction of Nanofiltration and Reverse-Osmosis-Membrane Rejection of Organic Compounds Using Random Forest Model. *Journal of Environmental Engineering* **2020**, *146* (11), 04020127. https://doi.org/10.1061/(ASCE)EE.1943-7870.0001806.

(32) Ammi, Y.; Khaouane, L.; Hanini, S. Prediction of the Rejection of Organic Compounds (Neutral and Ionic) by Nanofiltration and Reverse Osmosis Membranes Using Neural Networks. *Korean Journal of Chemical Engineering 2015 32:11* **2015**, *32* (11), 2300–2310. https://doi.org/10.1007/S11814-015-0086-Y.

(33) Khaouane, L.; Ammi, Y.; Hanini, S. Modeling the Retention of Organic Compounds by Nanofiltration and Reverse Osmosis Membranes Using Bootstrap Aggregated Neural Networks. *Arabian Journal for Science and Engineering 2016 42:4* **2016**, *42* (4), 1443–1453. https://doi.org/10.1007/S13369-016-2320-2.

(34) Su, C.; Yeo, H.; Xie, Q.; Wang, X.; Zhang, S. Understanding and Optimization of Thin Film Nanocomposite Membranes for Reverse Osmosis with Machine Learning. *J Memb Sci* **2020**, *606*, 118135. https://doi.org/10.1016/j.memsci.2020.118135.

(35) Bonny, T.; Kashkash, M.; Ahmed, F. An Efficient Deep Reinforcement Machine Learning-Based Control Reverse Osmosis System for Water Desalination. *Desalination* **2022**, *522*. https://doi.org/10.1016/J.DESAL.2021.115443.

(36) Van Der Bruggen, B.; Schaep, J.; Wilms, D.; Vandecasteele, C. Influence of Molecular Size, Polarity and Charge on the Retention of Organic Molecules by Nanofiltration. *J Memb Sci* **1999**, *156* (1), 29–41. https://doi.org/10.1016/S0376-7388(98)00326-3.

(37) Wijmans, J. G.; Baker, R. W. The Solution-Diffusion Model: A Review. *J Memb Sci* **1995**, *107* (1–2), 1–21. https://doi.org/10.1016/0376-7388(95)00102-I.

(38) Wang, X. L.; Tsuru, T.; Nakao, S. I.; Kimura, S. The Electrostatic and Steric-Hindrance Model for the Transport of Charged Solutes through Nanofiltration Membranes. *J Memb Sci* **1997**, *135* (1), 19–32. https://doi.org/10.1016/S0376-7388(97)00125-7.

(39) Deen, W. M. Hindered Transport of Large Molecules in Liquid-Filled Pores. *AIChE Journal* **1987**, *33* (9), 1409–1425. https://doi.org/10.1002/AIC.690330902.

(40) Chaabane, T.; Taha, S.; Taleb Ahmed, M.; Maachi, R.; Dorange, G. Coupled Model of Film Theory and the Nernst–Planck Equation in Nanofiltration. *Desalination* **2007**, *206* (1–3), 424–432. https://doi.org/10.1016/J.DESAL.2006.03.577.

(41) Goebel, R.; Glaser, T.; Skiborowski, M. Machine-Based Learning of Predictive Models in Organic Solvent Nanofiltration: Solute Rejection in Pure and Mixed Solvents. *Sep Purif Technol* **2020**, *248*, 117046. https://doi.org/10.1016/J.SEPPUR.2020.117046.

(42) Zhong, S.; Hu, J.; Yu, X.; Zhang, H. Molecular Image-Convolutional Neural Network (CNN) Assisted QSAR Models for Predicting Contaminant Reactivity toward OH Radicals: Transfer Learning, Data Augmentation and Model Interpretation. *Chemical Engineering Journal* **2021**, *408*, 127998. https://doi.org/10.1016/J.CEJ.2020.127998.

(43) Liu, Y. ling; Xiao, K.; Zhang, A. qian; Wang, X. mao; Yang, H. wei; Huang, X.; Xie, Y. F. Exploring the Interactions of Organic Micropollutants with Polyamide Nanofiltration Membranes: A Molecular Docking Study. *J Memb Sci* **2019**, *577*, 285–293. https://doi.org/10.1016/J.MEMSCI.2019.02.017.

(44) Fujioka, T.; Kodamatani, H.; Yujue, W.; Yu, K. D.; Wanjaya, E. R.; Yuan, H.; Fang, M.; Snyder, S. A. Assessing the Passage of Small Pesticides through Reverse Osmosis

Membranes. *J Memb Sci* **2020**, *595*, 117577.
https://doi.org/10.1016/J.MEMSCI.2019.117577.

(45) Shin, M. G.; Choi, W.; Park, S. J.; Jeon, S.; Hong, S.; Lee, J. H. Critical Review and
Comprehensive Analysis of Trace Organic Compound (TOrC) Removal with Polyamide
RO/NF Membranes: Mechanisms and Materials. *Chemical Engineering Journal* **2022**,
427. https://doi.org/10.1016/J.CEJ.2021.130957.

(46) Xing, L.; Glen, R. C.; Clark, R. D. Predicting PKa by Molecular Tree Structured
Fingerprints and PLS. *J Chem Inf Comput Sci* **2003**, *43* (3), 870–879.
https://doi.org/10.1021/CI020386S.

(47) Xing, L.; Glen, R. C. Novel Methods for the Prediction of LogP, PKa, and LogD. *J Chem
Inf Comput Sci* **2002**, *42* (4), 796–805. https://doi.org/10.1021/CI010315D.

(48) Wu, Z.; Ramsundar, B.; Feinberg, E. N.; Gomes, J.; Geniesse, C.; Pappu, A. S.; Leswing,
K.; Pande, V. MoleculeNet: A Benchmark for Molecular Machine Learning. *Chem Sci*
2017, *9* (2), 513–530. https://doi.org/10.48550/arxiv.1703.00564.

(49) Sanches-Neto, F. O.; Dias-Silva, J. R.; Keng Queiroz Junior, L. H.; Carvalho-Silva, V. H.
"PySiRC": Machine Learning Combined with Molecular Fingerprints to Predict the
Reaction Rate Constant of the Radical-Based Oxidation Processes of Aqueous Organic
Contaminants. *Environ Sci Technol* **2021**, *55* (18), 12437–12448.
https://doi.org/10.1021/acs.est.1c04326.

(50) Ding, Y.; Chen, M.; Guo, C.; Zhang, P.; Wang, J. Molecular Fingerprint-Based Machine
Learning Assisted QSAR Model Development for Prediction of Ionic Liquid Properties. *J
Mol Liq* **2021**, *326*, 115212. https://doi.org/10.1016/J.MOLLIQ.2020.115212.

(51) Zhong, S.; Hu, J.; Fan, X.; Yu, X.; Zhang, H. A Deep Neural Network Combined with
Molecular Fingerprints (DNN-MF) to Develop Predictive Models for Hydroxyl Radical
Rate Constants of Water Contaminants. *J Hazard Mater* **2020**, *383*, 121141.
https://doi.org/10.1016/J.JHAZMAT.2019.121141.

(52) Zhong, S.; Zhang, K.; Wang, D.; Zhang, H. Shedding Light on "Black Box" Machine
Learning Models for Predicting the Reactivity of HO Radicals toward Organic
Compounds. *Chemical Engineering Journal* **2021**, *405*, 126627.
https://doi.org/10.1016/J.CEJ.2020.126627.

(53) Francoeur, P. G.; Peñaherrera, D.; Koes, D. R. Active Learning for Small Molecule PKa
Regression; a Long Way To Go. **2022**. https://doi.org/10.26434/CHEMRXIV-2022-
8W1Q0.

(54) *A Unified Approach to Interpreting Model Predictions*.
https://proceedings.neurips.cc/paper/2017/hash/8a20a8621978632d76c43dfd28b67767-
Abstract.html (accessed 2022-07-25).

(55)   Martín, A.; Martínez, F.; Malfeito, J.; Palacio, L.; Prádanos, P.; Hernández, A. Zeta Potential of Membranes as a Function of PH: Optimization of Isoelectric Point Evaluation. *J Memb Sci* **2003**, *213* (1–2), 225–230. https://doi.org/10.1016/S0376-7388(02)00530-6.

(56)   Riniker, S.; Landrum, G. A. Similarity Maps - A Visualization Strategy for Molecular Fingerprints and Machine-Learning Methods. *J Cheminform* **2013**, *5* (9), 1–7. https://doi.org/10.1186/1758-2946-5-43/FIGURES/5.

(57)   Gao, K.; Nguyen, D. D.; Sresht, V.; Mathiowetz, A. M.; Tu, M.; Wei, G.-W. Are 2D Fingerprints Still Valuable for Drug Discovery? †. *Phys. Chem. Chem. Phys* **2020**, *22*, 8373. https://doi.org/10.1039/d0cp00305k.

(58)   Wigh, D. S.; Goodman, J. M.; Lapkin, A. A. A Review of Molecular Representation in the Age of Machine Learning. *Wiley Interdiscip Rev Comput Mol Sci* **2022**, e1603. https://doi.org/10.1002/WCMS.1603.

(59)   Cang, Z.; Wei, G. W. Integration of Element Specific Persistent Homology and Machine Learning for Protein-Ligand Binding Affinity Prediction. *Int J Numer Method Biomed Eng* **2018**, *34* (2). https://doi.org/10.1002/CNM.2914.

(60)   Cang, Z.; Mu, L.; Wei, G. W. Representability of Algebraic Topology for Biomolecules in Machine Learning Based Scoring and Virtual Screening. *PLoS Comput Biol* **2018**, *14* (1), e1005929. https://doi.org/10.1371/JOURNAL.PCBI.1005929.

(61)   Wu, K.; Wei, G. W. Quantitative Toxicity Prediction Using Topology Based Multitask Deep Neural Networks. *J Chem Inf Model* **2018**, *58* (2), 520–531. https://doi.org/10.1021/ACS.JCIM.7B00558/SUPPL_FILE/CI7B00558_SI_001.PDF.

(62)   Wu, K.; Zhao, Z.; Wang, R.; Wei, G. W. TopP–S: Persistent Homology-Based Multi-Task Deep Neural Networks for Simultaneous Predictions of Partition Coefficient and Aqueous Solubility. *J Comput Chem* **2018**, *39* (20), 1444–1454. https://doi.org/10.1002/JCC.25213.

(63)   Cereto-Massagué, A.; Ojeda, M. J.; Valls, C.; Mulero, M.; Garcia-Vallvé, S.; Pujadas, G. Molecular Fingerprint Similarity Search in Virtual Screening. *Methods* **2015**, *71* (C), 58–63. https://doi.org/10.1016/J.YMETH.2014.08.005.

(64)   Chen, T.; Guestrin, C. XGBoost: A Scalable Tree Boosting System. *Proceedings of the 22nd ACM SIGKDD International Conference on Knowledge Discovery and Data Mining*. https://doi.org/10.1145/2939672.

(65)   Yangali-Quintanilla, V.; Sadmani, A.; McConville, M.; Kennedy, M.; Amy, G. A QSAR Model for Predicting Rejection of Emerging Contaminants (Pharmaceuticals, Endocrine Disruptors) by Nanofiltration Membranes. *Water Res* **2010**, *44* (2), 373–384. https://doi.org/10.1016/j.watres.2009.06.054.

(66) Aas, K.; Jullum, M.; Løland, A. Explaining Individual Predictions When Features Are Dependent: More Accurate Approximations to Shapley Values. *Artif Intell* **2021**, *298*, 103502. https://doi.org/10.1016/J.ARTINT.2021.103502.

(67) Bowen, W. R.; Jones, M. G.; Welfoot, J. S.; Yousef, H. N. S. Predicting Salt Rejections at Nanofiltration Membranes Using Artificial Neural Networks. *Desalination* **2000**, *129* (2), 147–162. https://doi.org/10.1016/S0011-9164(00)00057-6.

(68) Libotean, D.; Giralt, J.; Rallo, R.; Cohen, Y.; Giralt, F.; Ridgway, H. F.; Rodriguez, G.; Phipps, D. Organic Compounds Passage through RO Membranes. *J Memb Sci* **2008**, *313* (1–2), 23–43. https://doi.org/10.1016/J.MEMSCI.2007.11.052.

(69) Hu, J.; Kim, C.; Halasz, P.; Kim, J. F.; Kim, J.; Szekely, G. Artificial Intelligence for Performance Prediction of Organic Solvent Nanofiltration Membranes. *J Memb Sci* **2021**, *619*, 118513. https://doi.org/10.1016/J.MEMSCI.2020.118513.

(70) Gao, H.; Zhong, S.; Zhang, W.; Igou, T.; Berger, E.; Reid, E.; Zhao, Y.; Lambeth, D.; Gan, L.; Afolabi, M. A.; Tong, Z.; Lan, G.; Chen, Y. Revolutionizing Membrane Design Using Machine Learning-Bayesian Optimization. *Environ Sci Technol* **2022**, *56* (4), 2572–2581. https://doi.org/10.1021/ACS.EST.1C04373/SUPPL_FILE/ES1C04373_SI_002.XLSX.

(71) Wang, M.; Xu, Q.; Tang, H.; Jiang, J. Machine Learning-Enabled Prediction and High-Throughput Screening of Polymer Membranes for Pervaporation Separation. *ACS Appl Mater Interfaces* **2022**, *14* (6). https://doi.org/10.1021/ACSAMI.1C22886/SUPPL_FILE/AM1C22886_SI_002.XLSX.

(72) Bellona, C.; Drewes, J. E. The Role of Membrane Surface Charge and Solute Physico-Chemical Properties in the Rejection of Organic Acids by NF Membranes. *J Memb Sci* **2005**, *249* (1–2), 227–234. https://doi.org/10.1016/J.MEMSCI.2004.09.041.

(73) Kiso, Y.; Sugiura, Y.; Kitao, T.; Nishimura, K. Effects of Hydrophobicity and Molecular Size on Rejection of Aromatic Pesticides with Nanofiltration Membranes. *J Memb Sci* **2001**, *192* (1–2), 1–10. https://doi.org/10.1016/S0376-7388(01)00411-2.

(74) Breitner, L. N.; Howe, K. J.; Minakata, D. Effect of Functional Chemistry on the Rejection of Low-Molecular Weight Neutral Organics through Reverse Osmosis Membranes for Potable Reuse. *Environ Sci Technol* **2019**, 11401–11409. https://doi.org/10.1021/acs.est.9b03856.

(75) Werber, J. R.; Porter, C. J.; Elimelech, M. A Path to Ultraselectivity: Support Layer Properties to Maximize Performance of Biomimetic Desalination Membranes. *Environ Sci Technol* **2018**, *52* (18), 10737–10747. https://doi.org/10.1021/ACS.EST.8B03426/ASSET/IMAGES/LARGE/ES-2018-03426Y_0006.JPEG.

(76) Vollhardt, K. P. C., & Schore, N. E. *Organic Chemistry: Structure and Function*; Macmillan International Higher Education, 2014.

(77) Phillip, W. A.; Elimelech, M. The Future of Seawater Desalination: Energy, Technology, and the Environment. *Science (1979)* **2011**, *333* (6043), 712–717.

(78) Wang, Z.; Horseman, T.; Straub, A. P.; Yip, N. Y.; Li, D.; Elimelech, M.; Lin, S. Pathways and Challenges for Efficient Solar-Thermal Desalination. *Sci Adv* **2019**.

(79) Sedlak, D. L. The Unintended Consequences of the Reverse Osmosis Revolution. *Environmental Science and Technology*. 2019, pp 3999–4000. https://doi.org/10.1021/acs.est.9b01755.

(80) Yang, Q.; Wang, K. Y.; Chung, T. S. A Novel Dual-Layer Forward Osmosis Membrane for Protein Enrichment and Concentration. *Sep Purif Technol* **2009**, *69* (3), 269–274. https://doi.org/10.1016/j.seppur.2009.08.002.

(81) Cui, Y.; Chung, T. S. Pharmaceutical Concentration Using Organic Solvent Forward Osmosis for Solvent Recovery. *Nat Commun* **2018**, *9* (1). https://doi.org/10.1038/s41467-018-03612-2.

(82) Lutchmiah, K.; Verliefde, A. R. D.; Roest, K.; Rietveld, L. C.; Cornelissen, E. R. Forward Osmosis for Application in Wastewater Treatment: A Review. *Water Research*. Elsevier Ltd July 1, 2014, pp 179–197. https://doi.org/10.1016/j.watres.2014.03.045.

(83) Sant'Anna, V.; Marczak, L. D. F.; Tessaro, I. C. Membrane Concentration of Liquid Foods by Forward Osmosis: Process and Quality View. *Journal of Food Engineering*. August 2012, pp 483–489. https://doi.org/10.1016/j.jfoodeng.2012.01.032.

(84) Park, H. B.; Kamcev, J.; Robeson, L. M.; Elimelech, M.; Freeman, B. D. Maximizing the Right Stuff: The Trade-off between Membrane Permeability and Selectivity. *Science (1979)* **2017**, *356* (6343), 1138–1148. https://doi.org/10.1126/science.aab0530.

(85) Geise, G. M.; Park, H. B.; Sagle, A. C.; Freeman, B. D.; McGrath, J. E. Water Permeability and Water/Salt Selectivity Tradeoff in Polymers for Desalination. *J Memb Sci* **2011**, *369* (1–2), 130–138. https://doi.org/10.1016/j.memsci.2010.11.054.

(86) Lee, S.; Lueptow, R. M. Reverse Osmosis Filtration for Space Mission Wastewater: Membrane Properties and Operating Conditions. *J Memb Sci* **2001**, *182* (1–2), 77–90. https://doi.org/10.1016/S0376-7388(00)00553-6.

(87) Werber, J. R.; Deshmukh, A.; Elimelech, M. The Critical Need for Increased Selectivity, Not Increased Water Permeability, for Desalination Membranes. *Environ. Sci. Technol. Lett* **2016**, *3*, 120. https://doi.org/10.1021/acs.estlett.6b00050.

(88) Lee, S.; Lueptow, R. M. Membrane Rejection of Nitrogen Compounds. *Environ Sci Technol* **2001**, *35* (14), 3008–3018. https://doi.org/10.1021/es0018724.

(89) Cath, T. Y.; Gormly, S.; Beaudry, E. G.; Flynn, M. T.; Adams, V. D.; Childress, A. E. Membrane Contactor Processes for Wastewater Reclamation in Space: Part I. Direct Osmotic Concentration as Pretreatment for Reverse Osmosis. *J Memb Sci* **2005**, *257* (1–2), 85–98. https://doi.org/10.1016/j.memsci.2004.08.039.

(90) Cath, T. Y.; Adams, D.; Childress, A. E. Membrane Contactor Processes for Wastewater Reclamation in Space: II. Combined Direct Osmosis, Osmotic Distillation, and Membrane Distillation for Treatment of Metabolic Wastewater. *J Memb Sci* **2005**, *257* (1–2), 111–119. https://doi.org/10.1016/j.memsci.2004.07.039.

(91) Lee, J.; Straub, A. P.; Elimelech, M. Vapor-Gap Membranes for Highly Selective Osmotically Driven Desalination. *J Memb Sci* **2018**, *555*, 407–417. https://doi.org/10.1016/j.memsci.2018.03.059.

(92) Cassano, A.; Drioli, E. Concentration of Clarified Kiwifruit Juice by Osmotic Distillation. *J Food Eng* **2007**, *79* (4), 1397–1404. https://doi.org/10.1016/j.jfoodeng.2006.04.021.

(93) Rehman, W. U.; Muhammad, A.; Khan, Q. A.; Younas, M.; Rezakazemi, M. Pomegranate Juice Concentration Using Osmotic Distillation with Membrane Contactor. *Sep Purif Technol* **2019**, *224*, 481–489. https://doi.org/10.1016/j.seppur.2019.05.055.

(94) Zambra, C.; Romero, J.; Pino, L.; Saavedra, A.; Sanchez, J. Concentration of Cranberry Juice by Osmotic Distillation Process. *J Food Eng* **2015**, *144*, 58–65. https://doi.org/10.1016/j.jfoodeng.2014.07.009.

(95) Coday, B. D.; Xu, P.; Beaudry, E. G.; Herron, J.; Lampi, K.; Hancock, N. T.; Cath, T. Y. The Sweet Spot of Forward Osmosis: Treatment of Produced Water, Drilling Wastewater, and Other Complex and Difficult Liquid Streams. *Desalination* **2014**, *333* (1), 23–35. https://doi.org/10.1016/j.desal.2013.11.014.

(96) Bailey, A. F. G.; Barbe, A. M.; Hogan, P. A.; Johnson, R. A.; Sheng, J. The Effect of Ultrafiltration on the Subsequent Concentration of Grape Juice by Osmotic Distillation. *J Memb Sci* **2000**, *164* (1–2), 195–204. https://doi.org/10.1016/S0376-7388(99)00209-4.

(97) Durham, R. J.; Nguyen, M. H. Hydrophobic Membrane Evaluation and Cleaning for Osmotic Distillation of Tomato Puree. *J Memb Sci* **1994**, *87* (1–2), 181–189. https://doi.org/10.1016/0376-7388(93)E0142-7.

(98) Warczok, J.; Gierszewska, M.; Kujawski, W.; Güell, C. Application of Osmotic Membrane Distillation for Reconcentration of Sugar Solutions from Osmotic Dehydration. *Sep Purif Technol* **2007**, *57* (3), 425–429. https://doi.org/10.1016/j.seppur.2006.04.012.

(99) Courel, M.; Dornier, M.; Rios, G. M.; Reynes, M. Modelling of Water Transport in Osmotic Distillation Using Asymmetric Membrane. *J Memb Sci* **2000**, *173* (1), 107–122. https://doi.org/10.1016/S0376-7388(00)00348-3.

(100) Mansouri, J.; Fane, A. G. Osmotic Distillation of Oily Feeds. *J Memb Sci* **1999**, *153* (1), 103–120. https://doi.org/10.1016/S0376-7388(98)00252-X.

(101) Tiraferri, A.; Yip, N. Y.; Straub, A. P.; Romero-Vargas Castrillon, S.; Elimelech, M. A Method for the Simultaneous Determination of Transport and Structural Parameters of Forward Osmosis Membranes. *J Memb Sci* **2013**, *444*, 523–538. https://doi.org/10.1016/j.memsci.2013.05.023.

(102) Wang, L.; Min, J. Modeling and Analyses of Membrane Osmotic Distillation Using Non-Equilibrium Thermodynamics. *J Memb Sci* **2011**, *378* (1–2), 462–470. https://doi.org/10.1016/j.memsci.2011.05.034.

(103) Gostoli, C. Thermal Effects in Osmotic Distillation. *J Memb Sci* **1999**, *163* (1), 75–91. https://doi.org/10.1016/S0376-7388(99)00157-X.

(104) Straub, A. P.; Elimelech, M. Energy Efficiency and Performance Limiting Effects in Thermo-Osmotic Energy Conversion from Low-Grade Heat. *Environ Sci Technol* **2017**, *51* (21), 12925–12937. https://doi.org/10.1021/acs.est.7b02213.

(105) Eames, I. W.; Marr, N. J.; Sabir, H. The Evaporation Coefficient of Water: A Review. *Int J Heat Mass Transf* **1997**, *40* (12), 2963–2973. https://doi.org/10.1016/S0017-9310(96)00339-0.

(106) Deshmukh, A.; Lee, J. Membrane Desalination Performance Governed by Molecular Reflection at the Liquid-Vapor Interface. *Int J Heat Mass Transf* **2019**, *140*, 1006–1022. https://doi.org/10.1016/j.ijheatmasstransfer.2019.06.044.

(107) Mason, E. A.; Malinauskas, A. P.; Evans, R. B. Flow and Diffusion of Gases in Porous Media. *J Chem Phys* **1967**, *46* (8), 3199–3216. https://doi.org/10.1063/1.1841191.

(108) Cunningham, R. E.; Williams, R. J. J. *Diffusion in Gases and Porous Media*; Springer US, 1980. https://doi.org/10.1007/978-1-4757-4983-0.

(109) Ferraro, V. C. A.; Chapman, S.; Cowling, T. G. The Mathematical Theory of Non-Uniform Gases. An Account of the Kinetic Theory of Viscosity, Thermal Conduction, and Diffusion in Gases. *The Mathematical Gazette* **1954**, *38* (323), 63. https://doi.org/10.2307/3609795.

(110) Lee, J.; Laoui, T.; Karnik, R. Nanofluidic Transport Governed by the Liquid/Vapour Interface. *NATURE NANOTECHNOLOGY |* **2014**, *9*. https://doi.org/10.1038/NNANO.2014.28.

(111) Lee, J.; Karnik, R. Desalination of Water by Vapor-Phase Transport through Hydrophobic Nanopores. *J Appl Phys* **2010**, *108* (4). https://doi.org/10.1063/1.3419751.

(112) Lee, J.; Laoui, T.; Karnik, R. Nanofluidic Transport Governed by the Liquid/Vapour Interface. *Nat Nanotechnol* **2014**, *9* (4), 317–323. https://doi.org/10.1038/nnano.2014.28.

(113) Phattaranawik, J.; Jiraratananon, R.; Fane, A. G. Heat Transport and Membrane Distillation Coefficients in Direct Contact Membrane Distillation. *J Memb Sci* **2003**, *212* (1–2), 177–193. https://doi.org/10.1016/S0376-7388(02)00498-2.

(114) Achilli, A.; Cath, T. Y.; Childress, A. E. Selection of Inorganic-Based Draw Solutions for Forward Osmosis Applications. *J Memb Sci* **2010**, *364* (1–2), 233–241. https://doi.org/10.1016/j.memsci.2010.08.010.

(115) Deshmukh, A.; Elimelech, M. Understanding the Impact of Membrane Properties and Transport Phenomena on the Energetic Performance of Membrane Distillation Desalination. *J Memb Sci* **2017**, *539* (March), 458–474. https://doi.org/10.1016/j.memsci.2017.05.017.

(116) Davenport, D. M.; Deshmukh, A.; Werber, J. R.; Elimelech, M. High-Pressure Reverse Osmosis for Energy-Efficient Hypersaline Brine Desalination: Current Status, Design Considerations, and Research Needs. *Environ Sci Technol Lett* **2018**, *5* (8), 467–475. https://doi.org/10.1021/acs.estlett.8b00274.

(117) Lin, S.; Yip, N. Y.; Elimelech, M. Direct Contact Membrane Distillation with Heat Recovery: Thermodynamic Insights from Module Scale Modeling. *J Memb Sci* **2014**, *453*, 498–515. https://doi.org/10.1016/j.memsci.2013.11.016.

(118) Werber, J. R.; Deshmukh, A.; Elimelech, M. The Critical Need for Increased Selectivity, Not Increased Water Permeability, for Desalination Membranes. *Environmental Science and Technology Letters*. American Chemical Society April 12, 2016, pp 112–120. https://doi.org/10.1021/acs.estlett.6b00050.

(119) Werber, J. R.; Deshmukh, A.; Elimelech, M. Can Batch or Semi-Batch Processes Save Energy in Reverse-Osmosis Desalination? *Desalination* **2017**, *402*, 109–122. https://doi.org/10.1016/j.desal.2016.09.028.

(120) Bui, A. V.; Nguyen, H. M.; Joachim, M. Characterisation of the Polarisations in Osmotic Distillation of Glucose Solutions in Hollow Fibre Module. *J Food Eng* **2005**, *68* (3), 391–402. https://doi.org/10.1016/j.jfoodeng.2004.06.015.

(121) Lin, S.; Straub, A. P.; Elimelech, M. Thermodynamic Limits of Extractable Energy by Pressure Retarded Osmosis. *Energy Environ Sci* **2014**, *7* (8), 2706–2714. https://doi.org/10.1039/c4ee01020e.

(122) Bartholomew, T. V.; Mauter, M. S. Computational Framework for Modeling Membrane Processes without Process and Solution Property Simplifications. *J Memb Sci* **2019**, *573*, 682–693. https://doi.org/10.1016/j.memsci.2018.11.067.

(123) Deshmukh, A.; Yip, N. Y.; Lin, S.; Elimelech, M. Desalination by Forward Osmosis: Identifying Performance Limiting Parameters through Module-Scale Modeling. *J Memb Sci* **2015**, *491*, 159–167. https://doi.org/10.1016/j.memsci.2015.03.080.

(124) Straub, A. P.; Elimelech, M. Energy Efficiency and Performance Limiting Effects in Thermo-Osmotic Energy Conversion from Low-Grade Heat. *Environ. Sci. Technol* **2017**, *51*, 12925–12937. https://doi.org/10.1021/acs.est.7b02213.

(125) Phuntsho, S.; Hong, S.; Elimelech, M.; Shon, H. K. Osmotic Equilibrium in the Forward Osmosis Process: Modelling, Experiments and Implications for Process Performance. *J Memb Sci* **2014**, *453*, 240–252. https://doi.org/10.1016/j.memsci.2013.11.009.

(126) Gustafson, R. D.; Murphy, J. R.; Achilli, A. A Stepwise Model of Direct Contact Membrane Distillation for Application to Large-Scale Systems: Experimental Results and Model Predictions. *Desalination* **2016**, *378*, 14–27. https://doi.org/10.1016/j.desal.2015.09.022.

(127) Ongaratto, R. S.; Menezes, L.; Borges, C. P.; Laranjeira da Cunha Lage, P. Osmotic Distillation Applying Potassium Pyrophosphate as Brine. *J Food Eng* **2018**, *228*, 69–78. https://doi.org/10.1016/j.jfoodeng.2018.02.013.

(128) Tuteja, A.; Choi, W.; Mabry, J. M.; Mckinley, G. H.; Cohen, R. E.; Prausnitz, J. M. *Robust Omniphobic Surfaces*; 2008.

(129) García-Payo, M. C.; Izquierdo-Gil, M. A.; Fernández-Pineda, C. Wetting Study of Hydrophobic Membranes via Liquid Entry Pressure Measurements with Aqueous Alcohol Solutions. *J Colloid Interface Sci* **2000**, *230*, 420–431. https://doi.org/10.1006/jcis.2000.7106.

(130) Rapp, B. E. *Microfluidics: Modeling, Mechanics and Mathematics*; 2016. https://doi.org/10.1016/c2012-0-02230-2.

(131) Deshmukh, A.; Yip, N. Y.; Lin, S.; Elimelech, M. Desalination by Forward Osmosis: Identifying Performance Limiting Parameters through Module-Scale Modeling. *J Memb Sci* **2015**, *491*, 159–167. https://doi.org/10.1016/j.memsci.2015.03.080.

(132) Boo, C.; Elimelech, M.; Hong, S. Fouling Control in a Forward Osmosis Process Integrating Seawater Desalination and Wastewater Reclamation. *J Memb Sci* **2013**, *444*, 148–156. https://doi.org/10.1016/j.memsci.2013.05.004.

(133) Zhou, S.; Xiong, Z.; Liu, F.; Lin, H.; Wang, J.; Li, T.; Han, Q.; Fang, Q. Novel Janus Membrane with Unprecedented Osmosis Transport Performance. *J Mater Chem A Mater* **2019**, *7* (2), 632–638. https://doi.org/10.1039/c8ta08541b.

(134) Zhou, S.; Liu, F.; Wang, J.; Lin, H.; Han, Q.; Zhao, S.; Tang, C. Y. Janus Membrane with Unparalleled Forward Osmosis Performance. *Environ Sci Technol Lett* **2019**, *6* (2), 79–85. https://doi.org/10.1021/acs.estlett.8b00630.

(135) Petrotos, K. B.; Lazarides, H. N. Osmotic Concentration of Liquid Foods. *J Food Eng* **2001**, *49* (2–3), 201–206. https://doi.org/10.1016/S0260-8774(00)00222-3.

(136) Liguori, L.; Russo, P.; Albanese, D.; Di Matteo, M. Evolution of Quality Parameters during Red Wine Dealcoholization by Osmotic Distillation. *Food Chem* **2013**, *140* (1–2), 68–75. https://doi.org/10.1016/j.foodchem.2013.02.059.

(137) Valdés, H.; Romero, J.; Saavedra, A.; Plaza, A.; Bubnovich, V. Concentration of Noni Juice by Means of Osmotic Distillation. *J Memb Sci* **2009**, *330* (1–2), 205–213. https://doi.org/10.1016/j.memsci.2008.12.053.

(138) Hongvaleerat, C.; Cabral, L. M. C.; Dornier, M.; Reynes, M.; Ningsanond, S. Concentration of Pineapple Juice by Osmotic Evaporation. *J Food Eng* **2008**, *88* (4), 548–552. https://doi.org/10.1016/j.jfoodeng.2008.03.017.

(139) Kwon, H. E.; Kwon, S. J.; Park, S. J.; Shin, M. G.; Park, S. H.; Park, M. S.; Park, H.; Lee, J. H. High Performance Polyacrylonitrile-Supported Forward Osmosis Membranes Prepared via Aromatic Solvent-Based Interfacial Polymerization. *Sep Purif Technol* **2019**, *212*, 449–457. https://doi.org/10.1016/j.seppur.2018.11.053.

(140) Lee, K. P.; Arnot, T. C.; Mattia, D. A Review of Reverse Osmosis Membrane Materials for Desalination-Development to Date and Future Potential. *Journal of Membrane Science*. March 15, 2011, pp 1–22. https://doi.org/10.1016/j.memsci.2010.12.036.

(141) Alkhudhiri, A.; Darwish, N.; Hilal, N. Membrane Distillation: A Comprehensive Review. *Desalination*. November 15, 2012, pp 2–18. https://doi.org/10.1016/j.desal.2011.08.027.

(142) Akshay Deshmukh; Chanhee Boo; Vasiliki Karanikola; Shihong Lin; P. Straub, A.; Tiezheng Tong; M. Warsinger, D.; Menachem Elimelech. Membrane Distillation at the Water-Energy Nexus: Limits, Opportunities, and Challenges. *Energy Environ Sci* **2018**, *11* (5), 1177–1196. https://doi.org/10.1039/C8EE00291F.

(143) Phattaranawik, J.; Jiraratananon, R.; Fane, A. G. Heat Transport and Membrane Distillation Coefficients in Direct Contact Membrane Distillation. *J Memb Sci* **2003**, *212* (1–2), 177–193. https://doi.org/10.1016/S0376-7388(02)00498-2.

(144) Tu, K. L.; Chivas, A. R.; Nghiem, L. D. Effects of Membrane Fouling and Scaling on Boron Rejection by Nanofiltration and Reverse Osmosis Membranes. *Desalination* **2011**, *279* (1–3), 269–277. https://doi.org/10.1016/J.DESAL.2011.06.019.

(145) Shen, M.; Keten, S.; Lueptow, R. M. Rejection Mechanisms for Contaminants in Polyamide Reverse Osmosis Membranes. *J Memb Sci* **2016**, *509*, 36–47. https://doi.org/10.1016/J.MEMSCI.2016.02.043.

(146) Wijekoon, K. C.; Hai, F. I.; Kang, J.; Price, W. E.; Cath, T. Y.; Nghiem, L. D. Rejection and Fate of Trace Organic Compounds (TrOCs) during Membrane Distillation. *J Memb Sci* **2014**, *453*, 636–642. https://doi.org/10.1016/j.memsci.2013.12.002.

(147) Winglee, J. M.; Bossa, N.; Rosen, D.; Vardner, J. T.; Wiesner, M. R. Modeling the Concentration of Volatile and Semivolatile Contaminants in Direct Contact Membrane

Distillation (DCMD) Product Water. *Environ Sci Technol* **2017**, *51* (22), 13113–13121. https://doi.org/10.1021/acs.est.6b05663.

(148) Parida, V. K.; Saidulu, D.; Majumder, A.; Srivastava, A.; Gupta, B.; Gupta, A. K. Emerging Contaminants in Wastewater: A Critical Review on Occurrence, Existing Legislations, Risk Assessment, and Sustainable Treatment Alternatives. *J Environ Chem Eng* **2021**, *9* (5), 105966. https://doi.org/10.1016/J.JECE.2021.105966.

(149) Salls, K. A.; Won, D.; Kolodziej, E. P.; Childress, A. E.; Hiibel, S. R. Evaluation of Semi-Volatile Contaminant Transport in a Novel, Gas-Tight Direct Contact Membrane Distillation System. *Desalination* **2018**, *427*, 35–41. https://doi.org/10.1016/j.desal.2017.11.001.

(150) Xie, M.; Nghiem, L. D.; Price, W. E.; Elimelech, M. Relating Rejection of Trace Organic Contaminants to Membrane Properties in Forward Osmosis: Measurements, Modelling and Implications. *Water Res* **2014**, *49*, 265–274. https://doi.org/10.1016/J.WATRES.2013.11.031.

(151) Lin, S.; Yip, N. Y.; Elimelech, M. Direct Contact Membrane Distillation with Heat Recovery: Thermodynamic Insights from Module Scale Modeling. *J Memb Sci* **2014**, *453*, 498–515. https://doi.org/10.1016/j.memsci.2013.11.016.

(152) Yaws, C. L. *Yaws' Handbook of Properties for Aqueous Systems*; Knovel Norwich, NY, 2012; Vol. 13.

(153) Yaws, C. L. *The Yaws Handbook of Vapor Pressure: Antoine Coefficients*; Gulf Professional Publishing, 2015.

(154) Yaws, C. L. Diffusion Coefficient in Water–Organic Compounds. In *Transport Properties of Chemicals and Hydrocarbons*; Elsevier, 2009; pp 502–593.

(155) Warneck, P. A Review of Henry's Law Coefficients for Chlorine-Containing C1 and C2 Hydrocarbons. *Chemosphere* **2007**, *69* (3), 347–361. https://doi.org/10.1016/j.chemosphere.2007.04.088.

(156) Khiter, A.; Balannec, B.; Szymczyk, A.; Arous, O.; Nasrallah, N.; Loulergue, P. Behavior of Volatile Compounds in Membrane Distillation: The Case of Carboxylic Acids. *J Memb Sci* **2020**, *612*, 118453. https://doi.org/10.1016/j.memsci.2020.118453.

(157) Banat, F. A.; Simandl, J. Removal of Benzene Traces from Contaminated Water by Vacuum Membrane Distillation. *Chem Eng Sci* **1996**, *51* (8), 1257–1265. https://doi.org/10.1016/0009-2509(95)00365-7.

(158) Phuntsho, S.; Hong, S.; Elimelech, M.; Shon, H. K. Osmotic Equilibrium in the Forward Osmosis Process: Modelling, Experiments and Implications for Process Performance. *J Memb Sci* **2014**, *453*, 240–252. https://doi.org/10.1016/J.MEMSCI.2013.11.009.

(159) Da Costa, A. R.; Fane, A. G.; Wiley, D. E. Spacer Characterization and Pressure Drop Modelling in Spacer-Filled Channels for Ultrafiltration. *J Memb Sci* **1994**, *87* (1–2), 79–98. https://doi.org/10.1016/0376-7388(93)E0076-P.

(160) Bagger-Jørgensen, R.; Meyer, A. S.; Varming, C.; Jonsson, G. Recovery of Volatile Aroma Compounds from Black Currant Juice by Vacuum Membrane Distillation. *J Food Eng* **2004**, *64* (1), 23–31. https://doi.org/10.1016/J.JFOODENG.2003.09.009.

(161) Kujawa, J.; Cerneaux, S.; Kujawski, W. Removal of Hazardous Volatile Organic Compounds from Water by Vacuum Pervaporation with Hydrophobic Ceramic Membranes. *J Memb Sci* **2015**, *474*, 11–19. https://doi.org/10.1016/j.memsci.2014.08.054.

(162) Gryta, M.; Barancewicz, M. Separation of Volatile Compounds from Fermentation Broth by Membrane Distillation. *Polish Journal of Chemical Technology* **2011**, *13* (3), 56–60. https://doi.org/10.2478/v10026-011-0038-1.

(163) Vollhardt, K. P. C., & Schore, N. E. *Organic Chemistry: Structure and Function*; Macmillan International Higher Education, 2014.

(164) Spencer, J. N.; Wolbach, W. S.; Hovick, J. W.; Ansel, L.; Modarress, K. J. Hydrogen Bonding by Alcohols and Amines. *J Solution Chem* **1985**, *14* (11), 805–814. https://doi.org/10.1007/BF00646002.

(165) Bouguecha, S.; Chouikh, R.; Dhahbi, M. Numerical Study of the Coupled Heat and Mass Transfer in Membrane Distillation. *Desalination* **2003**, *152* (1–3), 245–252. https://doi.org/10.1016/S0011-9164(02)01070-6.

(166) Lee, H.; Kim, H.-J.; Kwon, J.-H. Determination of Henry's Law Constant Using Diffusion in Air and Water Boundary Layers. *J Chem Eng Data* **2012**, *57* (11), 3296–3302. https://doi.org/10.1021/JE300954S.

(167) Ray, H.; Perreault, F.; Boyer, T. H. Rejection of Nitrogen Species in Real Fresh and Hydrolyzed Human Urine by Reverse Osmosis and Nanofiltration. *J Environ Chem Eng* **2020**, *8* (4), 103993. https://doi.org/10.1016/J.JECE.2020.103993.

(168) Croll, H.; Soroush, A.; Pillsbury, M. E.; Romero-Vargas Castrillón, S. Graphene Oxide Surface Modification of Polyamide Reverse Osmosis Membranes for Improved N-Nitrosodimethylamine (NDMA) Removal. *Sep Purif Technol* **2019**, *210*, 973–980. https://doi.org/10.1016/J.SEPPUR.2018.08.070.

(169) Mane, P. P.; Park, P. K.; Hyung, H.; Brown, J. C.; Kim, J. H. Modeling Boron Rejection in Pilot- and Full-Scale Reverse Osmosis Desalination Processes. *J Memb Sci* **2009**, *338* (1–2), 119–127. https://doi.org/10.1016/J.MEMSCI.2009.04.014.

(170) Yüksel, S.; Kabay, N.; Yüksel, M. Removal of Bisphenol A (BPA) from Water by Various Nanofiltration (NF) and Reverse Osmosis (RO) Membranes. *J Hazard Mater* **2013**, *263*, 307–310. https://doi.org/10.1016/J.JHAZMAT.2013.05.020.

(171) Ozaki, H.; Li, H. Rejection of Organic Compounds by Ultra-Low Pressure Reverse Osmosis Membrane. *Water Res* **2002**, *36* (1), 123–130. https://doi.org/10.1016/S0043-1354(01)00197-X.

(172) Xie, M.; Nghiem, L. D.; Price, W. E.; Elimelech, M. Comparison of the Removal of Hydrophobic Trace Organic Contaminants by Forward Osmosis and Reverse Osmosis. *Water Res* **2012**, *46* (8), 2683–2692. https://doi.org/10.1016/J.WATRES.2012.02.023.

(173) Rowland, R. S.; Taylor, R. Intermolecular Nonbonded Contact Distances in Organic Crystal Structures: Comparison with Distances Expected from van Der Waals Radii. **1996**. https://doi.org/10.1021/JP953141.

(174) Lin, S.; Nejati, S.; Boo, C.; Hu, Y.; Osuji, C. O.; Elimelech, M. Omniphobic Membrane for Robust Membrane Distillation. *Environ Sci Technol Lett* **2014**, *1* (11), 443–447. https://doi.org/10.1021/ez500267p.

(175) Xiao, Z.; Guo, H.; He, H.; Liu, Y.; Li, X.; Zhang, Y.; Yin, H.; Volkov, A. V.; He, T. Unprecedented Scaling/Fouling Resistance of Omniphobic Polyvinylidene Fluoride Membrane with Silica Nanoparticle Coated Micropillars in Direct Contact Membrane Distillation. *J Memb Sci* **2020**, *599*. https://doi.org/10.1016/j.memsci.2020.117819.

(176) Li, C.; Li, X.; Du, X.; Zhang, Y.; Wang, W.; Tong, T.; Kota, A. K.; Lee, J. Elucidating the Trade-off between Membrane Wetting Resistance and Water Vapor Flux in Membrane Distillation. *Environ. Sci. Technol* **2020**, *54*, 10333–10341. https://doi.org/10.1021/acs.est.0c02547.

(177) Wang, T.; Lv, C.; Ji, L.; He, X.; Wang, S. Designing Re-Entrant Geometry: Construction of a Superamphiphobic Surface with Large-Sized Particles. *ACS Appl Mater Interfaces* **2020**. https://doi.org/10.1021/acsami.0c11398.

(178) Wang, W.; Du, X.; Vahabi, H.; Zhao, S.; Yin, Y.; Kota, A. K.; Tong, T. Trade-off in Membrane Distillation with Monolithic Omniphobic Membranes. *Nature Communications 2019 10:1* **2019**, *10* (1), 1–9. https://doi.org/10.1038/s41467-019-11209-6.

(179) Lee, J.; Karnik, R. Desalination of Water by Vapor-Phase Transport through Hydrophobic Nanopores. *J Appl Phys* **2010**, *108* (4), 044315. https://doi.org/10.1063/1.3419751.

(180) Lopez, K. P.; Wang, R.; Hjelvik, E. A.; Lin, S.; Straub, A. P. Toward a Universal Framework for Evaluating Transport Resistances and Driving Forces in Membrane-Based Desalination Processes. *Sci Adv* **2023**, *9* (1). https://doi.org/10.1126/SCIADV.ADE0413.

(181) Vázquez, G.; Alvarez, E.; Navaza, J. M. Surface Tension of Alcohol + Water from 20 to 50 °C. *J. Chem. Eng. Data* **1995**, *40*, 611–614.

(182) Kim, B. S.; Harriott, P. Critical Entry Pressure for Liquids in Hydrophobic Membranes. *J Colloid Interface Sci* **1987**, *115* (1), 1–8. https://doi.org/10.1016/0021-9797(87)90002-6.

(183) Comini, N.; Huthwelker, T.; Diulus, J. T.; Osterwalder, J.; Novotny, Z. Factors Influencing Surface Carbon Contamination in Ambient-Pressure x-Ray Photoelectron Spectroscopy Experiments. *Journal of Vacuum Science & Technology A: Vacuum, Surfaces, and Films* **2021**, *39* (4), 043203. https://doi.org/10.1116/6.0001013.

(184) Boo, C.; Lee, J.; Elimelech, M. Omniphobic Polyvinylidene Fluoride (PVDF) Membrane for Desalination of Shale Gas Produced Water by Membrane Distillation. **2016**. https://doi.org/10.1021/acs.est.6b03882.

(185) Kharraz, J. A.; An, A. K. Patterned Superhydrophobic Polyvinylidene Fluoride (PVDF) Membranes for Membrane Distillation: Enhanced Flux with Improved Fouling and Wetting Resistance. *J Memb Sci* **2020**, *595*, 117596. https://doi.org/10.1016/J.MEMSCI.2019.117596.

APPENDICES

Appendix A: Supporting Information for Chapter 2 - Predicting organic solute rejection in reverse osmosis and nanofiltration with machine learning and molecular fingerprints

A.1: Fingerprint bit collision

Bit collision occurs when different sub-structures are stored in the same bit, and only one fragment will be presented at the end. Bit collision happens in the hashed style fingerprints including the path-based and circular MFs, and usually a low bit length is the cause. In this study, bit length of each case was adjusted to avoid bit collision because the occurrence of bit collision can confuse the interpretation stage of molecular fragments. A longer bit length is required to avoid multiple features being stored in the same bit, and these increased bit lengths lead to extended calculation times.

Bit collision can be counted by printing out the number of hashed features and the number of stored features with RDKit library. The difference between two becomes the number of lost features by bit collision. In Table A-S1, the counts of bit collision for the Path-based and Circular fingerprints cases were shown. Structural key fingerprints do not have bit collision because their keys are pre-defined. With the high bit lengths, path-based fingerprint cases had zero bit collision. However, circular fingerprint cases still had 1 or 3 collisions, but they can be negligible because they are very low numbers compared to the entire bit lengths (0.024% and 0.018%).
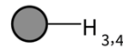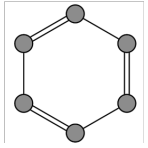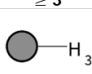
Table A-S1. The counts of bit collision for path-based and circular fingerprints cases.

Fingerprint	Parameter	Bit length	Count of bit collision
Path-based	maximum length of 1	1024	0
Path-based	maximum length of 3	32768	0
Circular	maximum radius of 1	4096	1
Circular	maximum radius of 3	16384	3

A.2: Molecular fragments generated by fingerprints

All the molecular fragments appeared in the top-20 SHAP results were printed out to compare the molecular fragments over different fingerprints. The molecular fragments of MACCS were shown in the manuscript, and the fragments for other fingerprints are shown below.

Table A-S2. Most important molecular fragments generated with the MACCS model.
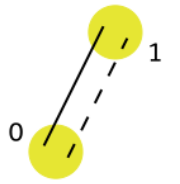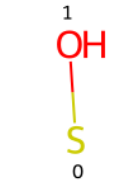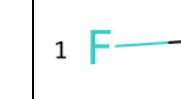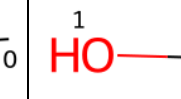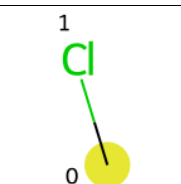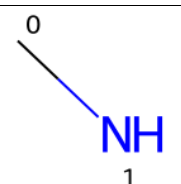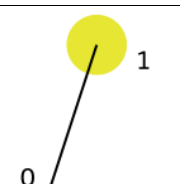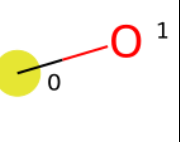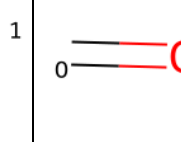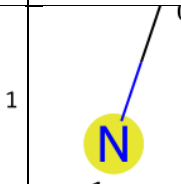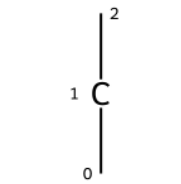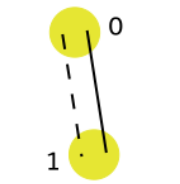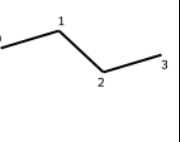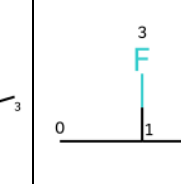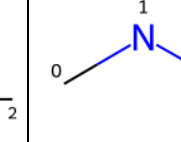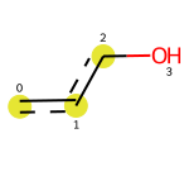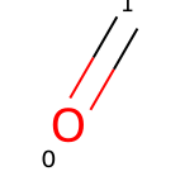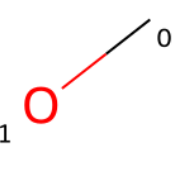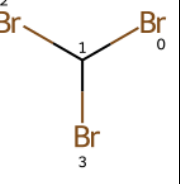
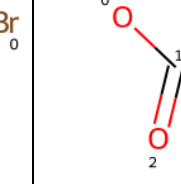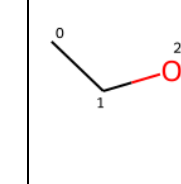| Molecular fragments					
F 43	any bond any atom 113	**O ≥ 3** 147	6 molecule ring ≥ 2 any bond any atom 146	aliphatic C with 3 or 4 H ≥ 2 —H$_{3,4}$ 150	any bond O C 124
any bond any atom not C and not H with not 0 hydrogen aliphatic C with 2 hydrogen 92	aromatic ring ≥ 2 126	aliphatic C with 3 H ≥ 3 —H$_3$ 142	any bond any atom not C and not H with not 0 hydrogen aliphatic C with 2 hydrogen 91	**O ≥ 4** 141	6 molecule ring ≥ 1 any bond any atom 164

Table A-S3. Most important molecular fragments generated with the PubChem model.

Molecular fragments					
C(~C)(~C) 333	>= 16 H 3	C-H 284	>= 16 C 13	>= 8 H 2	>= 1 F 24
C(~O)(~O) 381	O-C-C-C-C-C-C-C 697	>= 4 C 11	O-H 309	C(~C)(~O) 353	C-C:C-O-[#1] 591

* ~ regardless of bond order, : bond aromacity, [#1] 1 hydrogen

Table A-S4. Most important molecular fragments generated with the Path-based models.

Molecular fragments with maximum path length of 1					
285	931	3	52	384	563
575	1024	37	348	884	634
Molecular fragments with maximum path length of 3					
24342	5405	31747	29548	27961	22941
20020	1076	18995	28509	8959	31029

* a yellow atom indicates a carbon atom in an aromatic ring

Table A-S5. Most important molecular fragments generated with the Circular models.

Molecular fragments with maximum radius of 1					
1929	1381	2129	2163	3068	2438
3106	2332	2856	2699	2794	2050
Molecular fragments with maximum radius of 3					
6025	11260	5477	14451	6225	10630
10242	11048	7202	657	10524	11122

* a yellow atom indicates a carbon atom in an aromatic ring, a blue atom indicates a center atom, a star mark indicates any atom or any bond can be connected to the site

A.3: Clustering compounds based on the MACCS fingerprint

A few compounds in Cluster 2 and 3 are demonstrated in Figure A-S1 to represent the general shapes of the compounds in the clusters. The compounds in Cluster 1 share similarity of multiple rings and branches. The compounds in Cluster 3 share similarity of long linear path and presence of multiple oxygen atoms. Since compounds with similar structures are grouped via clustering, we

were able to identify the difference or similarity in or between clusters. It is noteworthy that compounds in Cluster 4 had relatively high variances compared to other cl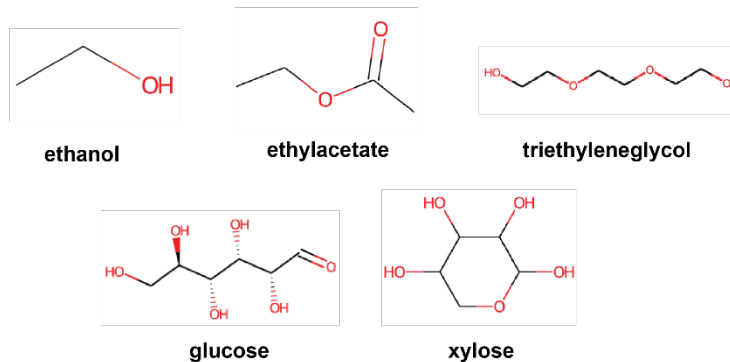usters, and may indicate that there are more specific chemical compound groups than 4. The number of clusters of 4 was determined by testing inertia (sum of distance squares between a central point and data points in cluster) changes along with different number of clusters in Figure A-S2. The number of clusters of 4 was chosen because adding more clusters started giving insignificant decrease of inertia. Although adding more clusters can provide more information, the extra complexity may be not required depending on cases.

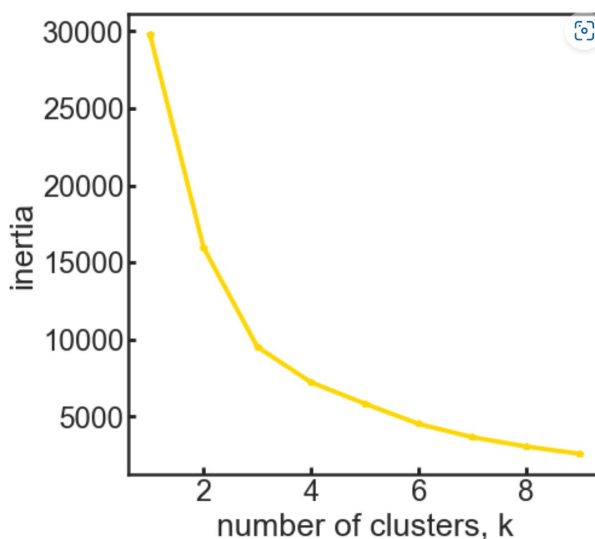**Cluster 2 (44 compounds)**

atrazin

lidocaine

propyphenazone

diltiazem

Cluster 3 (31 compounds)

ethanol

ethylacetate

triethyleneglycol

glucose

xylose
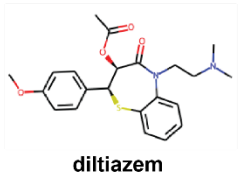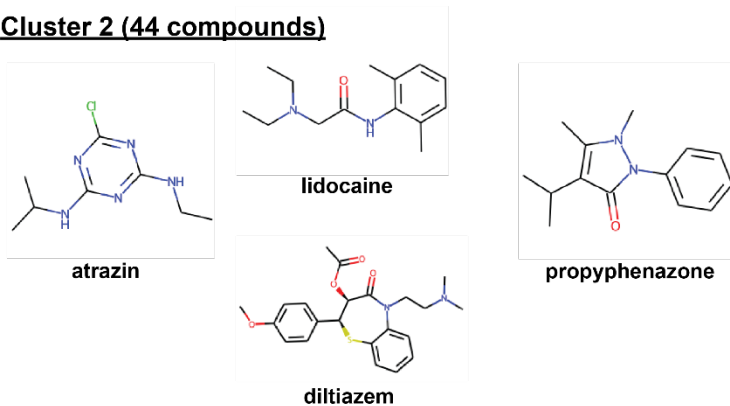
Figure A-S1. Exemplary organic compounds in different clusters (Cluster 2 and 3).

133

Figure A-S2. Inertia curve for choosing the optimal number of clusters.

The entire list of the frequent MACCS fingerprint features in each cluster is displayed in Table A-S6. The sub-dataset contained 176 unique compounds, and Cluster 1, Cluster 2, Cluster 3, and Cluster 4 had 49, 44, 31, and 52 compounds, respectively. The frequency percentage was calculated by dividing their counts with the number of compounds in total in each cluster. Cluster 1, 2, and 3 had 10, 10, and 7 fingerprint features exceeding 80% of frequency percentages, whereas Cluster 4 had zero features over 80%, which means the compounds in the cluster are highly varying. The physical meaning of each MACCS feature can be found on the web. Originally, MACCS fingerprint has 166 keys, but in this study, we generated 167 MACCS keys with an extra padding key in the very first bit.

Table A-S6. List of top-10 ranked MACCS features in each cluster.

Cluster 1 (49 compounds)			Cluster 2 (44 compounds)		
MACCS feature No.	Count	Appearance (%)	MACCS feature No.	Count	Appearance (%)
164	49	100	157	44	100
165	49	100	159	44	100
166	49	100	162	44	100
158	45	91.84	163	44	100
163	45	91.84	164	44	100
140	43	87.76	166	44	100
153	41	83.67	143	39	88.64
128	40	81.63	161	39	88.64
144	40	81.63	165	39	88.64
160	40	81.63	149	36	81.82
Cluster 3 (31 compounds)			Cluster 4 (52 compounds)		
MACCS feature No.	Count	Appearance (%)	MACCS feature No.	Count	Appearance (%)
165	31	100	165	40	76.92
154	28	90.32	166	39	75.00
158	28	90.32	163	38	73.08
110	26	83.87	164	37	71.15
133	26	83.87	162	33	63.46
156	26	83.87	157	32	61.54
140	25	80.65	155	30	57.69
160	24	77.42	159	30	57.69
83	23	74.19	158	27	51.92
105	20	64.52	160	27	51.92

Appendix B: Supporting Information for Chapter 3 - Opportunities for high productivity and selectivity desalination via osmotic distillation with improved membrane design

B.1: Determination of partial vapor pressure driving force

The driving force for water transport in osmotic distillation (OD) is the difference in water partial vapor pressure across the membrane. Water molecules evaporate from the feed solution and condense in the draw solution, and hence, the vapor pressure difference between the feed and draw allows water molecules to move through the membrane. As shown in Equation S1, vapor pressure of an aqueous solution, P_v, is expressed by using the Kohler equation [1]:

$$P_v(T, C) = P_{v,0}(T)\exp\left[\frac{-\pi(C)V_m}{RT}\right] \tag{S1}$$

$$\pi = kCRT \tag{S2}$$

where π is the osmotic pressure of the solution which is a function of the solution concentration C, V_m is the molar volume of the solution, R is the ideal gas constant, k is van't Hoff's factor, and $P_{v,0}$ is the equilibrium vapor pressure of water corresponding to solution temperature T. In our work, there was no external applied pressure ($P = 0$) so the vapor pressure of the feed and draw sides was only a function of temperature, T, and concentration, C.

B.2: Simulating osmotic distillation membranes with a hydrophilic support

To allow for a fair comparison between FO and OD membranes, the OD membranes were simulated with a support layer having equivalent properties to the commercial FO membranes. The S value of the FO membrane was 453 µm and tortuosity, τ, porosity, e, and support layer thickness, d, were 2.23, 0.74, and 150 µm, respectively. In our analysis, the support layer of the OD membrane had the same properties as the FO membrane support layer.

Without a support layer, we are able to use the same heat transfer coefficient, h, of 1000 W m^{-2}K^{-1} for the feed and draw side. With a hydrophilic support layer, the heat transfer

coefficient on the draw side, h_d, has an added component from the heat transfer coefficient of the support layer, $h_{support}$:

$$h_{support} = \frac{K_s}{d} \tag{S3}$$

$$h_d = \left(\frac{1}{h} + \frac{1}{h_{support}}\right)^{-1} \tag{S4}$$

where K_s is the thermal conductivity of the support layer and can be obtained using the porosity (0.8), air thermal conductivity (0.01 W m^{-1}K^{-1}), and material thermal conductivity (0.2 W m^{-1}K^{-1}). d is the thickness of the support layer. The modified draw side heat transfer coefficient, h_d, was used when calculating heat transfer of a membrane with a support layer in the element- and module-scale analysis.
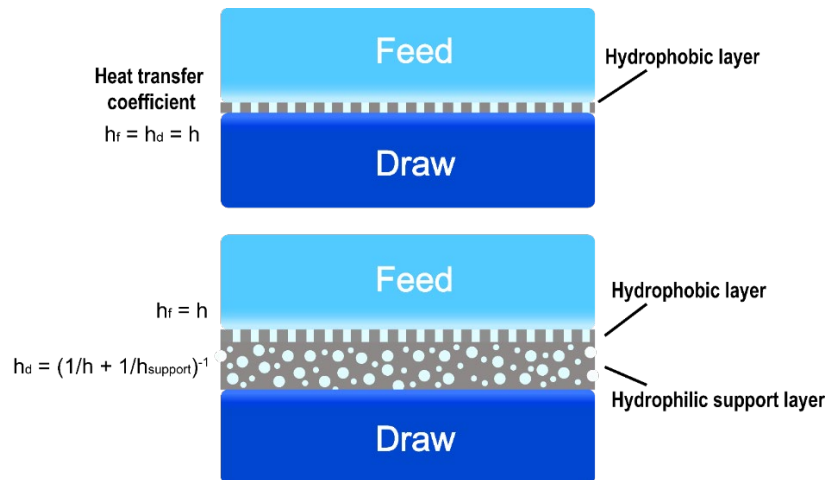
Figure B-S1. Schematic diagram of an osmotic distillation membrane without a hydrophilic support layer (top) and with a hydrophilic support layer (bottom).

B.3: Determination of forward osmosis membrane properties

The properties of a representative commercial membrane (Hydration Technology Innovations Thin-Film Composite, HTI-TFC) were retrieved from previous work in the literature where the water permeability coefficient, A, and structural parameter, S, were shown to be 1.48 kg m^{-2}h^{-1}bar^{-1} and 453 μm, respectively [2]. The salt permeability coefficient, B, was determined using the permeability-selectivity relationship described previously in the literature, where B is a function of A [3]:

$$B = \gamma A^3 \tag{S5}$$

Previous work found the constant γ, which relates A and B, to be 0.0133 L^{-2} m^{4}h^{2}bar^3 based on a comprehensive analysis of the performance of polyamide thin-film composite membranes.

B.4: Simulation of forward osmosis membrane module

The element-scale water and salt flux of FO are expressed below:

$$J_w = A(\pi_{D,m} - \pi_{F,m}) \tag{S6}$$

$$J_s = B(C_{D,m} - C_{F,m}) \tag{S7}$$

where J_w is the water vapor flux across the membrane, A is the water permeability coefficient, $\pi_{D,m}$ and $\pi_{F,m}$ are the osmotic pressure of the draw and feed membrane surface, J_s is the salt flux through the membrane, B is the salt permeability coefficient, and $C_{D,m}$ and $C_{F,m}$ are the feed and draw concentrations at the membrane surface.

The water and salt flux equations incorporating the effects of external concentration polarization (ECP) and internal concentration polarization (ICP) are given by [4]:

$$J_w = \frac{A\left[\pi_{D,b}\exp\left(-\frac{J_w S}{D}\right) - \pi_{F,b}\exp\left(\frac{J_w}{k}\right)\right]}{1 + \left(\frac{B}{J_w}\right)\left[\exp\left(\frac{J_w}{k}\right) - \exp\left(-\frac{J_w S}{D}\right)\right]} \tag{S8}$$

$$J_s = \frac{B\left[C_{D,b}\exp\left(-\frac{J_w S}{D}\right) - C_{F,b}\exp\left(\frac{J_w}{k}\right)\right]}{1 + \left(\frac{B}{J_w}\right)\left[\exp\left(\frac{J_w}{k}\right) - \exp\left(-\frac{J_w S}{D}\right)\right]} \tag{S9}$$

The dilutive ICP on the draw side is described as $(-\frac{J_w S}{D})$ and the concentrative ECP on the feed side is described as $(\frac{J_w}{k})$. The diffusion coefficient, D, is 1.48×10^{-9} m^2 s^{-1} and the mass transfer coefficient, k, is 0.02769 kg m^{-2}s^{-1}. The water flux decrease caused by the net solute permeation (forward salt flux and reverse salt flux) is represented as $(\frac{B}{J_w})\left[\exp\left(\frac{J_w}{k}\right) - \exp\left(-\frac{J_w S}{D}\right)\right]$, which is the denominator of the J_w and J_s equations. Note that dilutive ECP also occurs on the draw side. However, its impact is negligible compared to dilutive ICP so it was ignored in the calculations.

The differential equations representing mass transfer of water and salt in the system were discretized using a finite membrane area, A_m. Two differential equations were used to determine the flow rates and concentrations along the membrane module:

$$\frac{dQ_f(A_m)}{dA_m} = \frac{dQ_d(A_m)}{dA_m} = -J_w \tag{S10}$$

$$\frac{d[Q_f(A_m)C_f(A_m)]}{dA_m} = \frac{d[Q_d(A_m)C_d(A_m)]}{dA_m} = J_s \tag{S11}$$

The volumetric balance of water and mass balance of salt were expressed above. The balance equations were solved using the modified Powell method in conjunction with the element-scale analysis. The boundary conditions for numerical solutions were $Q_f(0) = Q_{f,0}$, $Q_d(N) = Q_{d,0}$, $C_f(0) = C_{f,0}$, and $C_d(N) = C_{d,0}$. The calculated water and salt flux over the entire module were used to obtain water recovery and bulk concentrations with the membrane properties described in Supplementary Note.

References

[1]   E.A. Mason, A.P. Malinauskas, R.B. Evans, Flow and diffusion of gases in porous media, J. Chem. Phys. 46 (1967) 3199–3216. doi:10.1063/1.1841191.

[2]   H.-E. Kwon, S.J. Kwon, S.-J. Park, M.G. Shin, S.-H. Park, M.S. Park, H. Park, J.-H. Lee, High performance polyacrylonitrile-supported forward osmosis membranes prepared via aromatic solvent-based interfacial polymerization, (2018). doi:10.1016/j.seppur.2018.11.053.

[3]   N. Yin Yip, M. Elimelech, Performance Limiting Effects in Power Generation from Salinity Gradients by Pressure Retarded Osmosis, Environ. Sci. Technol. 45 (2011) 35. doi:10.1021/es203197e.

[4]   A. Deshmukh, N.Y. Yip, S. Lin, M. Elimelech, Desalination by forward osmosis: Identifying performance limiting parameters through module-scale modeling, J. Memb. Sci. 491 (2015) 159–167. doi:10.1016/j.memsci.2015.03.080.

Appendix C: Supporting Information for Chapter 4 - Evaluation of volatile and semi-volatile organic compound transport in membrane distillation modules

C.1: Mass and heat transport of water vapor

The mass and heat transport across the hydrophobic MD membrane is shown in Figure 4.1 of the main text. The membrane has pores filled with air and water vapor that become pathways for water vapor flow through the membrane, J_w, which is driven by a difference in the partial vapor pressure of water, P_v, that depends primarily on the temperature difference between the feed and permeate membrane interfaces ($T_{f,m}$ and $T_{p,m}$, respectively). The temperature difference across the membrane leads to a net flux of water vapor from the feed to the permeate side, and the associated evaporation and condensation of water molecules induces convective and conductive heat transport. Convective heat transport occurs when the water molecules carry the latent heat of vaporization, $H_{v,w}$, through the membrane to cool the feed stream and heat the permeate stream. The temperature difference across the membrane then induces conductive heat transfer as heat is transported back toward the feed, the rate of which depends on the thermal conductivity of the membrane, K_m, the temperature at the feed membrane interface, $T_{f,m}$, and the temperature at the draw membrane interface, $T_{p,m}$. The sum of convective and conductive heat is the net heat flux, q. Since the solute flux, J_s, of the volatile compounds is relatively small compared to the existing amounts of water in the feed and permeate sides, the heat transport through the latent heat of vaporization of volatile compounds, $H_{v,s}$, was neglected in the calculation. The water flux, J_w, and heat flux, q, are expressed as follows:[1]

$$J_w = B[P_v(T_{f,m}, C_{f,m}) - P_v(T_{p,m}, C_{p,m})] \tag{S12}$$

$$q = J_w H_{v,w} + \frac{K_m}{d}(T_{f,m} - T_{p,m}) + \sum_{i=0}^{n} J_i H_{v,i} \tag{S13}$$

The vapor permeability, B, is determined by incorporating Hertz hypothesis and total transport resistance:[2,3]

$$B = \varepsilon \sqrt{\frac{M_w}{2\pi R_g \bar{T}}} \left[R_t + R_{i,f} + R_{i,p}\right]^{-1} \tag{S14}$$

where the total resistance is determined by the transmission resistance, R_t, the interface resistance on the feed side, $R_{i,f}$, the interface resistance on the permeate side, $R_{i,p}$, the molecular weight of water, M_w, and the average temperature of both membrane surfaces, $\bar{T}$.

Transmission resistance, R_t, arises from collisions that occur as water molecules pass through the membrane pores. Transmission resistance is the inverse of effective transmission probability, η_{eff}, and can also be expressed using the effective diffusion coefficient, D_{eff}, and the mean speed of water vapor, $\bar{v}_w$.[3]

$$R_t = \frac{1}{\eta_{eff}} = \frac{\bar{v}_w d}{4 D_{eff}} \tag{S15}$$

The collisions that cause transmission resistances can be described using two diffusion regimes.[4,5] In molecular diffusion, transport resistances are dominated by collisions between water and air molecules, whereas Knudsen diffusion involves interactions between water molecules and pore walls. The transition between the two regimes is defined by the membrane pore size and mean free path of water vapor. When the size of the pore is larger than the mean free path of the vapor (60–100 nm at atmospheric pressure),[6] the system is in the molecular diffusion regime. In contrast, if the membrane has smaller pores than the mean free path, the system is in the Knudsen regime. Thus, the equation for the effective diffusion coefficient, D_{eff}, contains terms for molecular diffusion and Knudsen diffusion. D_{eff} can be approximated by:

$$D_{eff} \approx \left[\frac{1 - \frac{p_0(\bar{T})}{p_t}}{D_{w,a}} + \frac{1}{D_{w,M}}\right]^{-1} \tag{S16}$$

where $\frac{p_0(\bar{T})}{p_t}$ is the mole fraction of water vapor assumed by comparing the pure water vapor pressure and the total pressure of water and air in the pores, $\bar{T}$ is the mean temperature of the feed and draw sides, p_t is the total pressure inside the pores, and $p_0(\bar{T})$ is the equilibrium water vapor

pressure at a given temperature. This approximation is valid when the operating temperature range falls between 20 and 80 °C.[3] D_{wa} represents the binary (water-air) diffusion coefficient of water vapor, which reflects the molecular diffusion contribution to resistance, and $D_{w,M}$ represents the Knudsen diffusion coefficient of water vapor across the membrane.

$$D_{w,a} = \frac{cT^{\frac{3}{2}}}{(p_t l_{wa}^2 \Omega_D)}\left[\frac{1}{M_w} + \frac{1}{M_a}\right]^{\frac{1}{2}} \tag{S17}$$

$$D_{w,M}\frac{\Delta C}{d} = \frac{\eta \bar{v}_w \Delta C}{4} \tag{S18}$$

$$D_{w,M} = \frac{\eta \bar{v}_w d}{4} \tag{S19}$$

$$\eta = 1 + \left(\frac{L^2}{4}\right) - \left(\frac{L}{4}\right)(L^2 + 4)^{\frac{1}{2}}$$

$$- \frac{\left[(8 - L^2)(L^2 + 4)^{\frac{1}{2}} + L^3 - 16\right]^2}{72L(L^2 + 4)^{1/2} - 288\ln[L + (L^2 + 4)^{1/2}] + 288\ln 2} \tag{S20}$$

$D_{w,a}$ is expressed based on previous studies,[3] where a characteristic length, $l_{w,a}$, is obtained by the Lennard-Jones 12-6 potential. The constant, c, is an empirical constant, and the collision integral, Ω_D, is for mass diffusion. Both $D_{w,M}$ and $D_{w,a}$ depend on temperature, and thus, transmission resistance and vapor permeability are also temperature-dependent. The Knudsen diffusion coefficient, $D_{w,M}$, in eq S18 is determined by equating the mole flux calculated from the transmission probability, η, (the right-hand side of eq S18) with the flux calculated from the diffusion equation (the left-hand side of eq S18).[7] The transmission probability, η, in a cylindrical

tube was determined using the aspect ratio, L, which is defined as the pore length divided by the pore radius.[3] Substituting eq S16 into eq S15 defines transmission resistance, R_t, as following:

$$R_t = \frac{(1 - \frac{p_0(\bar{T})}{p_t})\bar{v}_w d}{4D_{w,a}} + \frac{1}{\eta} \tag{S21}$$

Interface resistance, R_i, occurs because vapor molecules can be reflected at the gas-liquid interface and is expressed using the condensation coefficient, σ, which is the probability of water vapor condensation into bulk liquid at the gas-liquid interface.[8]

$$R_i = \frac{1 - \sigma(T)}{\sigma(T)} \tag{S22}$$

For thick membranes, transmission resistances greatly outweigh resistances at the interfaces. However, it has been shown interface resistances are a critical consideration for thin and highly permeable membranes with low transmission resistances.[3] Interface resistance is a function of temperature because higher temperatures result in increased energy levels of water vapor that lead to a higher probability of reflection at the gas-liquid interface.[9] Since the feed and draw side surface temperatures change during the evaporation and condensation of water molecules, the feed interface and draw interface resistances are calculated separately.

C.2: Overview of molecular properties in the data

Table C-S1 summarizes the mean and standard deviation values of molecular weight, partitioning coefficient, dipole moment, and Henry's constant for each compound class. The last column indicates the number of compounds included in each class. Alkanes has zero standard deviations due to the number of compounds in the class.

Table C-S1. Summary of molecular properties for different organic compound classes. The mean and standard deviation (STD) of each compound property is provided.

Chemical class	MW (g mol⁻¹)	Octanol-water partitioning coefficient	Henry's constant at 25 °C (Pa·L mol⁻¹)	Dipole (debye)	No. of compounds

	Mean	STD	Mean	STD	Mean	STD	Mean	STD	
Alcohols	79.79	22.11	0.88	0.64	9.27×10^2	6.10×10^2	1.53	0.04	6
Aldehydes	96.13	9.99	1.47	0.24	9.48×10^3	6.64×10^3	2.44	0.04	2
Alkanes	58.12	0	2.31	0	9.82×10^7	0	0	0	1
Alkenes	116.50	25.27	2.30	0.35	1.56×10^6	1.01×10^6	0.77	0.69	6
Alkyl halides	103.07	38.84	1.55	0.25	4.61×10^5	3.52×10^5	1.31	0.23	7
Amines	86.12	7.02	0.94	0.14	6.54×10^2	4.61×10^2	0.99	0.36	2
Arenes	105.21	15.52	3.01	0.77	1.24×10^6	1.71×10^6	0.22	0.36	8
Esters	115.76	25.55	1.82	0.91	5.87×10^4	3.39×10^4	1.50	0.57	5
Ethers	90.34	2.19	1.03	0.4	3.19×10^4	2.76×10^4	1.97	0.30	2
Ketones	97.57	37.11	1.01	0.99	5.59×10^3	3.46×10^3	2.54	0.07	7
Nitrile	47.06	6.01	0.03	0.18	8.54×10^3	5.44×10^3	2.12	0.07	2
Phenols	129.18	38.63	2.67	1.31	5.72×10^2	1.06×10^3	2.17	0.21	6

## C.3: Change of Henry's constant with varying temperatures

Since temperature significantly affects vapor pressure, Henry's constant is a function of temperature as well. The Henry's constants of butane, chloroform, ethanol, and phenol span the range of values studied in this work. Figure C-S1 shows that the Henry's constant of the four compounds increase with increasing temperature. In some cases, the temperature dependence of the Henry's constant is not consistent between different compounds due to different activity coefficients and Antoine constants (eq 24 and 25).
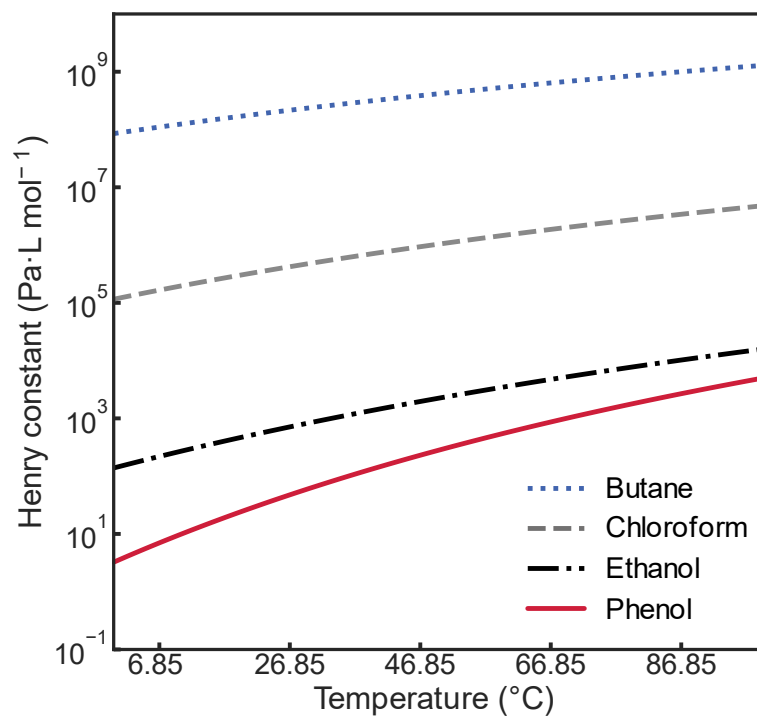
Figure C-S1. Henry's constant change along with different temperatures. Henry's constant was calculated using partial vapor pressure, activity coefficient, and molar volume. The temperature range fell in 0-100 ℃.

## C.4: Effect of operating temperature on mass transport resistance

The ratio of membrane resistance to total resistance and rejection obtained with membrane surface concentrations were shown for all compounds studied, indicating a trend where the rejection decreased (Figure C-S2A) and the ratio decreased as the Henry's constant increased (Figure C-S2B). The trend was expedited with high feed temperature due to increasing Henry's constant. The Henry's constant increases along with increasing temperature (see Figure C-S1), and the increased difference of the Henry's constant caused the ratio of membrane resistance to decline. In Figure C-S2A, rejection of each volatile compound is shown with different feed temperatures. The Henry's constant of 100 and 10000 Pa·L mol^{-1} were used as boundary values to divide the regimes. In the membrane resistance regime, the rejections decreased with Henry's constant, and the feed temperature changes did not significantly affect their transports under the regime. However, the decrease of the rejection approached thresholds in the boundary layer resistance regime, and high feed temperature affected Henry's constant and the rejections of the compounds decreased with feed temperature increases.
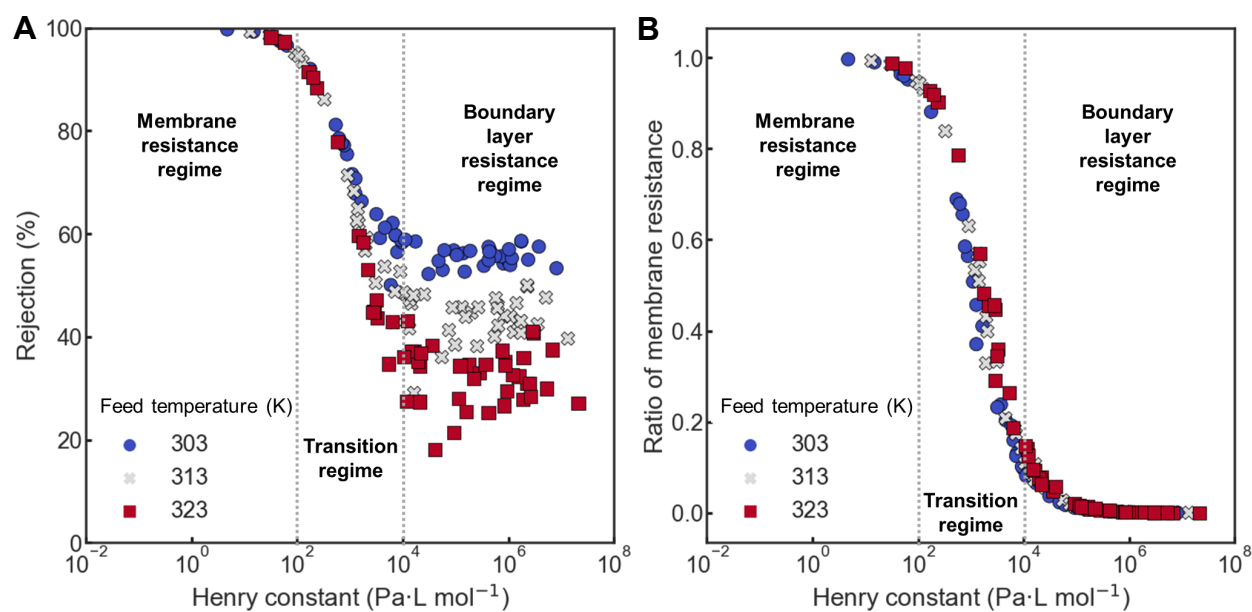
Figure C-S2. (A) Rejections of compounds with varying feed temperatures (B) Change of ratio of membrane resistance with varying feed temperatures

C.5: Validating predicted rejections via comparing to experimental rejections

This work built a computational model to describe the volatile compound transport in MD system based on prior models used in the literature.[10] The predicted results for certain compounds (4-tert-octylphenol, 4-tert-butylphenol, benzophenone, and bisphenol A) were compared to experimental results from a previous study in Figure C-S3.[11] The predictions from the model described the experimental values with good accuracy. The rejections were calculated by using the feed and permeate membrane surface concentrations. The gray bars indicate measurements from previous experiments. The hollow bars indicate the predicted values by the model. For benzophenone, the predicted values fell in the error range of the experimental results. For 4-tert-octylphenol, 4-tert-butylphenol, and bisphenol A, the predicted values were within 12% of the experimental values.
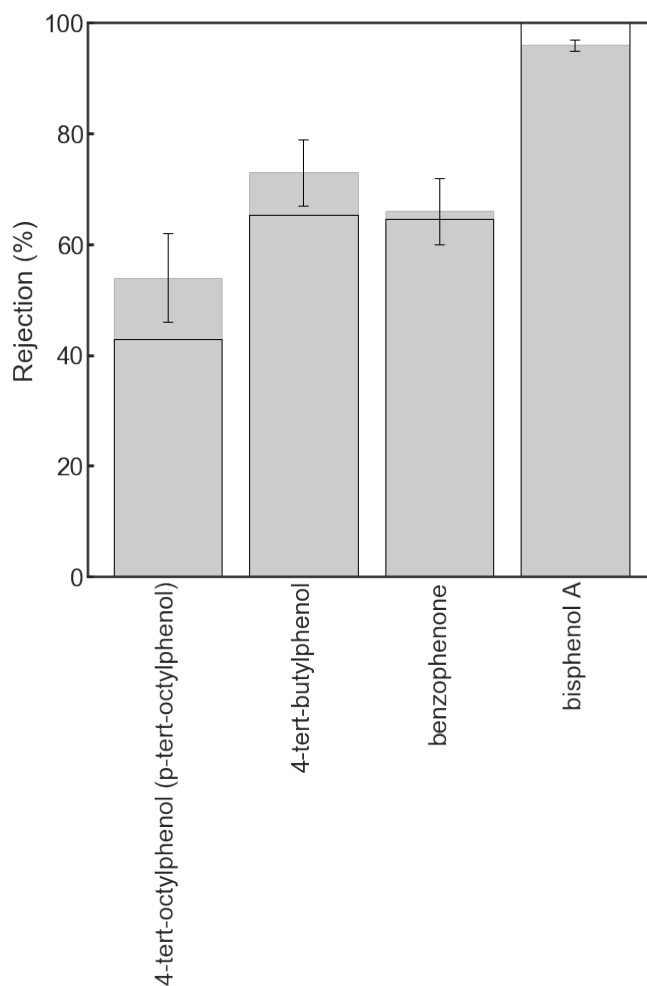
Figure C-S3. Comparison of predicted rejection and experimental rejection for four volatile and semi-volatile compounds. The experimental and predicted rejection were obtained in the same conditions: membrane pore radius and porosity were 0.22 μm and 0.7, respectively; the operating temperatures were 40 °C and 20 °C for the feed and permeate, respectively; and the velocity of the crossflow cell was 11.7 cm/s

C.6: Regression coefficients of solute flux with Henry's constant and diffusion coefficient

Fitting lines in Figure 4.2C and D were obtained by using linear and non-linear regression for the low Henry's constant group (< 10000 Pa·L mol^{-1}), which is colored red, and the high Henry's constant group (> 10000 Pa·L mol^{-1}), which is colored blue, respectively. The relationship between the solute flux and Henry's constant for the low Henry's constant group was calculated with a linear regression (Eq S23), whereas the relationship between the solute flux and diffusion coefficient was built using a more detailed correlation based on the transport equations (Eq S24):

$$J_s \propto \alpha H \tag{S23}$$

$$J_s \propto \frac{\beta D}{\gamma D + \delta} \tag{S24}$$

where H is Henry's constant; D is diffusion coefficient; J_s is solute flux; and $\alpha, \beta, \gamma, and\ \delta$ are regression coefficients. The equation was constructed using eq 32, 34, and 35.

References

(1)   Straub, A. P.; Elimelech, M. Energy Efficiency and Performance Limiting Effects in Thermo-Osmotic Energy Conversion from Low-Grade Heat. *Environ. Sci. Technol.* **2017**, *51* (21), 12925–12937. https://doi.org/10.1021/acs.est.7b02213.

(2)   Eames, I. W.; Marr, N. J.; Sabir, H. The Evaporation Coefficient of Water: A Review. *Int. J. Heat Mass Transf.* **1997**, *40* (12), 2963–2973. https://doi.org/10.1016/S0017-9310(96)00339-0.

(3)   Deshmukh, A.; Lee, J. Membrane Desalination Performance Governed by Molecular Reflection at the Liquid-Vapor Interface. *Int. J. Heat Mass Transf.* **2019**, *140*, 1006–1022. https://doi.org/10.1016/j.ijheatmasstransfer.2019.06.044.

(4)   Mason, E. A.; Malinauskas, A. P.; Evans, R. B. Flow and Diffusion of Gases in Porous Media. *J. Chem. Phys.* **1967**, *46* (8), 3199–3216. https://doi.org/10.1063/1.1841191.

(5)   Cunningham, R. E.; Williams, R. J. J. *Diffusion in Gases and Porous Media*; Springer US, 1980. https://doi.org/10.1007/978-1-4757-4983-0.

(6)   Ferraro, V. C. A.; Chapman, S.; Cowling, T. G. The Mathematical Theory of Non-Uniform Gases. An Account of the Kinetic Theory of Viscosity, Thermal Conduction, and Diffusion in Gases. *Math. Gaz.* **1954**, *38* (323), 63. https://doi.org/10.2307/3609795.

(7)   Lee, J.; Laoui, T.; Karnik, R. Nanofluidic Transport Governed by the Liquid/Vapour Interface. *Nat. Nanotechnol. |* **2014**, *9*. https://doi.org/10.1038/NNANO.2014.28.

(8)   Lee, J.; Karnik, R. Desalination of Water by Vapor-Phase Transport through Hydrophobic Nanopores. *J. Appl. Phys.* **2010**, *108* (4). https://doi.org/10.1063/1.3419751.

(9)   Lee, J.; Laoui, T.; Karnik, R. Nanofluidic Transport Governed by the Liquid/Vapour Interface. *Nat. Nanotechnol.* **2014**, *9* (4), 317–323. https://doi.org/10.1038/nnano.2014.28.

(10)   Winglee, J. M.; Bossa, N.; Rosen, D.; Vardner, J. T.; Wiesner, M. R. Modeling the Concentration of Volatile and Semivolatile Contaminants in Direct Contact Membrane Distillation (DCMD) Product Water. *Environ. Sci. Technol.* **2017**, *51* (22), 13113–13121. https://doi.org/10.1021/acs.est.6b05663.

(11)   Wijekoon, K. C.; Hai, F. I.; Kang, J.; Price, W. E.; Cath, T. Y.; Nghiem, L. D. Rejection and Fate of Trace Organic Compounds (TrOCs) during Membrane Distillation. *J. Memb. Sci.* **2014**, *453*, 636–642. https://doi.org/10.1016/j.memsci.2013.12.002.

Appendix D: Supporting Information for Chapter 5 - Omniphobic membranes with re-entrant structures for separating low surface tension liquids in pressure-driven distillation

D.1: Checking the durability of nanoparticles

There is a possibility that nanoparticles attached by electrostatic adsorption may be washed away while operating. The same modified membrane sample was used under multiple LEP tests and became wet (drying before re-use). Then the SEM images of the membrane surface were taken. The membrane in Figure D-S1a was used for the LEP tests of XX, XX, and XX, and the other membrane in Figure D-S1b was used for the LEP test of XX. The SEM images showed that the particles were not washed away after multiple wetting.
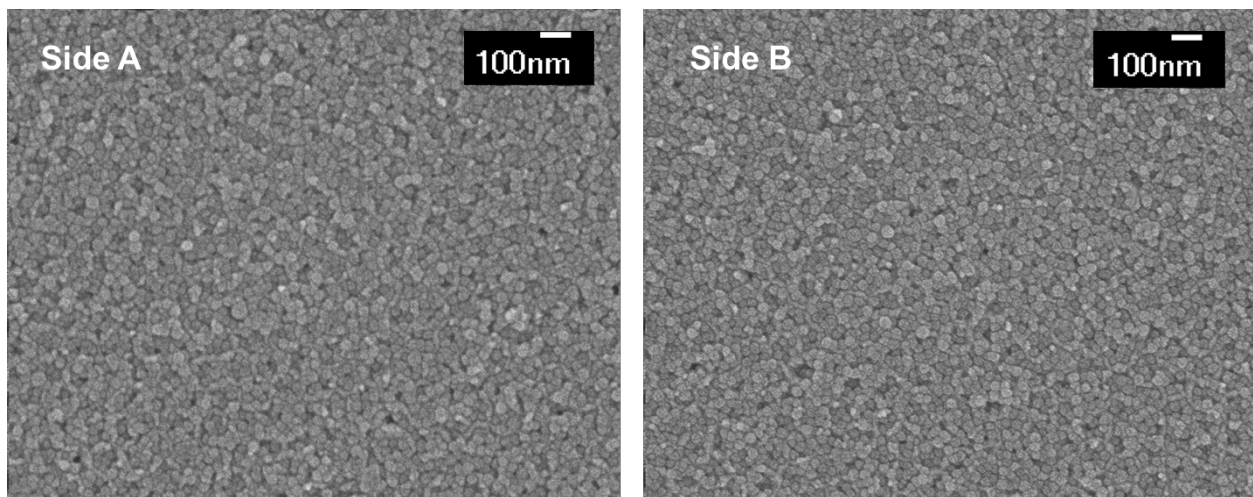

Figure D-S1. SEM images of the omniphobic membranes after multiple use for LEP tests

D.2: Simulation details

Expanded LEP values were obtained with varying re-entrant structure angles and surface tension of liquid (see Figure 5.4b). Equation 43 was used for calculating LEP values. Intrinsic contact angles, θ, are supposed to change with varying surface tension of liquid, so they were interpolated by using the three known values of water (72 mN/m & 110°), hexadecane (27 mN/m & 80°), and ethanol (22 mN/m & 70°). Nanoparticle radius was 11 nm, and the default pore radius was 20 nm.

Least squares minimization was used to simulate re-entrant structure angles from the measured data. Due to its nano-sized scale, measuring the re-entrant structure angles from SEM image is challenging. 'least_squares' function in Scipy was used for the optimization task with a Cauchy loss method. While other parameters were fixed, re-entrant structure angle kept changing from the initial value to minimize the least squares error between predictions and measurements. Initial values of 0 and 20° were used for the control and omniphobic membranes, respectively. The fitted re-entrant structure angles were -3 and -24° for the control and omniphobic AAO membranes.

Least squares optimization was also used to compare the effects of re-entrant structure angle and pore size on LEP. The nanoparticle depositions on the pore entrances provided re-entrant structure angles, but also could make the pore entrances smaller. And as shown in Equation 43, pore radius, r, is a important factor to control LEP values. Therefore, we demonstrated that these LEP increases with the omniphobic membranes are from re-entrant structure angles, not narrowed pore entrances. We ran two different optimization tasks. The first optimization was to fit re-entrant structure angle as shown in Figure 5.4a. The second optimization was to fit pore radius with the measured LEP data. The initial pore size was assumed as 20 nm, and the re-entrant structure angle of -3° (obtained angle for a control AAO membrane) was used. This simulated a scenario where re-entrant structure angle increase was ignored and pore size became small. The found pore radius was 15 nm with the optimization, and it was not bringing a good fit to the measured data (see Figure D-S2). The orange dashed line is originally calculated values with the optimized re-entrant structure angle. The dark red dotted line is calculated values with the optimized pore radius, and it brings higher errors from the measured LEP points. Therefore, the increased LEP values in our tests are primarily derived from the re-entrant structure angle changes.
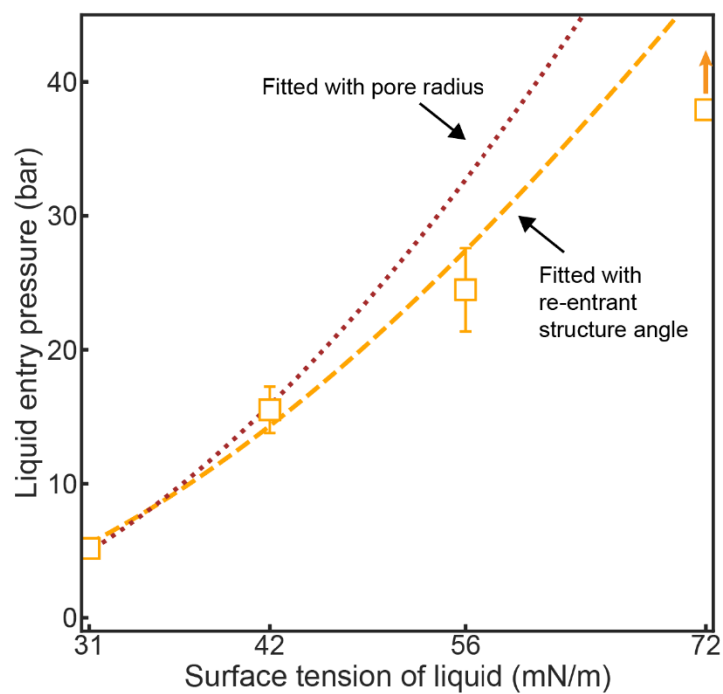
Figure D-S2. Comparison of the predicted LEP values from the re-entrant structure optimization and the pore radius optimization